AWARD NUMBER: W81XWH-16-1-0375

TITLE: SERS Nanosensors for in Vivo Glucose Sensing

PRINCIPAL INVESTIGATOR: Milan Mrksich

CONTRACTING ORGANIZATION: Northwestern University, Evanston, IL

REPORT DATE: December 2022

TYPE OF REPORT: Final

PREPARED FOR: U.S. Army Medical Research and Development Command
Fort Detrick, Maryland 21702-5012

REPORT DOCUMENTATION PAGE

Form Approved
OMB No. 0704-0188

1. REPORT DATE	2. REPORT TYPE	3. DATES COVERED
December 2022	Final	01Sep2016-31Aug2022

4. TITLE AND SUBTITLE

SERS Nanosensors for in Vivo Glucose Sensing

5a. CONTRACT NUMBER
W81XWH-16-1-0375

5b. GRANT NUMBER

5c. PROGRAM ELEMENT NUMBER

6. AUTHOR(S)

Milan Mrksich, Eric Berns, Ji Eun Park, Vitor Brasiliense, Guru Neupane
E-Mail: milan.mrksich@northwestern.edu

5d. PROJECT NUMBER

5e. TASK NUMBER

5f. WORK UNIT NUMBER

7. PERFORMING ORGANIZATION NAME(S) AND ADDRESS(ES)

Northwestern University
Evanston, Illinois 60208

8. PERFORMING ORGANIZATION REPORT NUMBER

9. SPONSORING / MONITORING AGENCY NAME(S) AND ADDRESS(ES)

U.S. Army Medical Research and Development Command
Fort Detrick, Maryland 21702-5012

10. SPONSOR/MONITOR'S ACRONYM(S)

11. SPONSOR/MONITOR'S REPORT NUMBER(S)

12. DISTRIBUTION / AVAILABILITY STATEMENT

Approved for Public Release; Distribution Unlimited

13. SUPPLEMENTARY NOTES

14. ABSTRACT

The goal of this program was to develop small and sensitive nanosensors for the continuous glucose monitoring in living tissue without the need for drawing blood. A major advantage of the transdermal sensors we are developing is to directly detect glucose itself – not the byproducts of its transformation. The technique we use – surface-enhanced Raman spectroscopy (SERS) – is based on light and informs on the presence of glucose on or near metallic nanosensors. In Major Task 1, we worked on the development of i) sensitive nanosensors, ii) selective capture layers that can be immobilized onto metal surfaces, iii) the integration of ligands on nanoparticles, and iv) integration of the functionalized nanoparticles with microneedle arrays for SERS sensing. We have successfully developed novel SERS nanoplatforms that integrates gold nanoparticles and capture layers. We have also developed electro-chemical SERS methods, integrated with microneedle arrays, to sense biomolecules without the use of a small molecule binding ligand. In Major Task 2, we evaluated the biocompatibility and mechanical stability of functionalized plasmonic SERS microarray sensors and demonstrated their ability to measure pH in skin phantom models after repeated implantations. We also evaluated thermal stability. In Major Task 3, the SERS performance of the plasmonic microneedle arrays were evaluated ex vivo in rat, pig, and human skin samples.

15. SUBJECT TERMS
Glucose, sensing, boronic acid, SERS, spectroscopy, hydrogel, microneedle array, continuous glucose monitoring, medical device

16. SECURITY CLASSIFICATION OF:			17. LIMITATION OF ABSTRACT	18. NUMBER OF PAGES	19a. NAME OF RESPONSIBLE PERSON USAMRDC
a. REPORT	**b. ABSTRACT**	**c. THIS PAGE**	Unclassified	71	**19b. TELEPHONE NUMBER** *(include area code)*
Unclassified	Unclassified	Unclassified			

Standard Form 298 (Rev. 8-98)
Prescribed by ANSI Std. Z39.18

TABLE OF CONTENTS

Page

1. INTRODUCTION

Diabetes is a chronic disease in which levels of blood glucose – a small molecule that serves as an energy source – exceed the norm and pose a host of primary and secondary health complications. The goal of this program is to lighten the physical and psychological burden that daily blood glucose checks represent for patients and to improve their long-term health through the development of small and sensitive nanosensors that *continuously* detect and measure glucose in living tissue over a long period of time (several months) without the need for drawing blood. A major advantage of the transdermal sensors we are developing is to *directly* detect glucose itself – not the byproducts of glucose transformation - which require external reagents that add extra costs and steps, and which can respond to other molecules in the blood, such as fructose, leading to false inflation of measurements.

2. KEYWORDS

Glucose, diabetes, pH, biosensing, SERS, Raman scattering, spectroscopy, microneedle array, plasmonic microneedles, transdermal patch, continuous monitoring, ex vivo, electrochemical sensing, reversible

3. ACCOMPLISHMENTS

Major goals of the project
As stated in the approved Statement of Work (SOW), the Specific Aims and Major Tasks of this program were:

Specific Aim 1: Functional Nanosensors Development
    Major Task 1: Synthesis and fabrication
    We proposed two designs: a metal film over nanospheres substrates that would be subcutaneously implanted, and a transdermal nanosensing patch that would be applied onto the skin. We proposed a boronic acid-based glucose capture layer. Several molecular designs, including boronic acid-based molecules, were investigated and evaluated for their efficiency to bind glucose and pH. We demonstrated successful incorporation of functionalized gold nanorods into microneedle arrays, capable of generating SERS spectra reporting on analytes. Due to difficulty in synthesizing glucose capture ligands with effective binding, we have explored alternative strategies to reversibly adsorb analytes to the surface using electrochemical methods. We demonstrated that applied potential can be used to modulate the surface chemistry (and therefore analyte binding constant), enabling selective sensing on microneedle arrays. This method also enables application of interpretable multivariate analysis, which has the potential of coping with presence of interfering biomolecules (which are likely to be present in vivo).

    Major Task 2: Biocompatibility of functional nanosensors
    We proposed integrating the glucose capture layers to the nanosensors and evaluate the functionality of the whole nanosensing platform using surface-enhanced Raman spectroscopy (SERS). We demonstrated multiple approaches for forming microarrays, including the use of

4

anti-fouling materials. We characterized the stability of these microneedles after repeated use in skin phantom models.

Specific Aim 2: *In Vivo* Glucose SERS Sensing

Major Task 3: Animal studies

We proposed implanting nanosensors with SERS/SESORS detection into rats, measuring glucose levels, and assessing their long-term stability. We integrated functionalized nanorods into microneedle nanosensor patches and demonstrated their ability to detect changes in pH in phantom skin and skin models. Experiments in skin using plasmonic microneedle array was performed ex vivo in rat skin, pig skin, and in human skin. We successfully demonstrated the sensing ability of the plasmonic microneedle array by detecting skin pH while inserted in human skin ex vivo.

ACCOMPMLISHMENTS

Major Task 1: Synthesis and fabrication

1. NANOSENSOR FABRICATION

1.1 Metal film over nanospheres (FONs) substrates

Metal film over nanospheres (FONs) substrates are nanostructured metallic surfaces exhibiting high SERS performance (i.e., enhancing Raman signals by a factor of 10^7 or higher) with the advantage of being easily functionalized, thus serving as a great sensing platform and an ideal one for testing new functionalization layers. MFONs are typically made by evaporating silver or gold onto a hexagonal close packed array of silica spheres (~300-600 nm in diameter) either using thermal evaporation or physical vapor deposition. While the SERS performance – evaluated by measuring its enhancement factor (EF) –for these substrates is very good even over large areas, relatively little is known about the structure-performance relationship in these substrates.

To address this critical aspect of rational SERS sensor engineering at the nanoscale, the Van Duyne lab has investigated the interrelationship between structure (using scanning electron microscopy - SEM), far-field optical property (i.e., localized surface plasmon resonance (LSPR) spectroscopy) and near-field optical property (i.e., SERS)

Depending on the fabrication method (stationary vs. spinning metal deposition, designated as ST-FONs and SP-FONs, respectively), we clearly confirmed by SEM analysis that it is possible to control the fine morphology of the metal film in the 10−90 nm range, with the resulting nanofeatures differing in their shape and size dispersity. Using wavelength-scan surface-enhanced Raman excitation spectroscopy (WS-SERES), we directly measured the near-field SERS enhancement profile of both ST-FONs and SP-FONs and clearly showed that the near- and far-field profiles of SP-FONs were spectrally aligned, whereas a ∼ 45 nm spectral shift was observed in the case of ST-FONs. The extensive numerical analysis revealed that the presence of nanofeatures with small size polydispersity results in the spectral alignment of optical far-field and near-field profiles. The absence of a commonly observed, near- to far-field spectral shift is

attributed to a significant increase in the radiative damping originating from the surface morphology of the FONs.

We have shown that by controlling the FONs fabrication methodology through the metal evaporation conditions, it is possible to predict the SERS performance of the FONs substrates through the wavelength at which the maximum EF will occur. These findings were published in The Journal of Physical Chemistry C.[1]

1.2 Microneedle Arrays

1.2.1 State of the art and rationale for design selection

One of the sensing platforms we developed is a SERS-active microneedle array for a transdermal sensor toward use for continuous glucose monitoring (CGM). Here we outline some of the basic structural parameters that dictate the effectiveness of such a sensor.

The most important feature is its optical transparency at the wavelength of the SERS excitation in the 700-800 nm region of the visible-NIR spectrum. These wavelengths of light penetrate human skin and enable Raman scattered light to be detected. Additionally, the transdermal patch requires a robust design so that both the structural integrity and functionality of the sensor are not compromised during penetration through skin. Once the patch is applied onto the skin, the biosensor needs to be mechanically and chemically stable throughout the continuous monitoring time period and remain functional over several weeks and months. The transdermal patch will serve as the biosensing component by evaluating the glucose level in the interstitial fluid. Therefore, optimizing the depth of the microneedles in direct contact with the epidermis is critical to target the fluid and avoid blood capillaries. This will minimize the contamination risk of the microneedles with blood-borne proteins, which may aggravate biofouling of the sensor, and also minimize pain by avoiding contact with nerves beneath the epidermis.

The Mrksich lab has fabricated polymer-based solid microneedles, taking into consideration all the pre-requisites outlined above. We have used a replica molding technique where the transdermal patch was shaped within an elastomeric mold (polydimethylsiloxane, PDMS) enabling reproducible fabrication of the patches. Two commercially available PDMS molds were purchased for the initial testing of polymer materials. The mold from Micropoint Technologies PTE Ltd has pyramidal features measuring 300 μm in depth, 200 μm in width, and spaced by a 500 μm tip-to-tip distance. The second mold, from Blueacre Technology, has conical features measuring 300 μm in depth, 300 μm in width, and spaced by a 600 μm tip-to-tip distance.

In addition to the structural requirements of a microneedle transdermal sensor, it must incorporate plasmonic materials to enhance the Raman scattering signal and be considered SERS-active. Thus, following the microneedle preparation, the transdermal biosensors were functionalized with SERS-active Au nanorods (AuNRs) that were synthesized in the Van Duyne group. There are two possible ways to incorporate the SERS active component with the transtermal patch: (i) functionalizing the microneedle surface with AuNRs, and (ii) embedding the AuNRs within the microneedles.

6

We pursued these two approaches by working with two different polymer types. The first approach requires the use of rigid polymers that do not swell in water. This allows us to locate AuNRs from the aqueous suspension solution on the microneedle surface. The second approach requires SERS active components densely distributed within the polymer matrix that must also beporous to allow glucose diffusion into the matrix. We have fabricated such microneedles using hydrogel-based materials. The selection of the hydrogel material relies on the mechanical robustness (to penetrate skin), porosity (for diffusion), biocompatibility, and optical characteristics of the solidified hydrogel.

### 1.2.2 Solid Microneedles SERS Biosensors using Rigid Polymers

NOA (Norland Optical Adhesive) is a generic name for commercially available one-part adhesive liquids that can be cured under UV light exposure at room temperature. The composition of NOA products is protected by a commercial patent, but some studies report the constituents of NOA65,[2-4] which is a mixture of trimethylolpropane diallyl ether, trimethylolpropane tristhiol, isophorome diisocyanate ester and benzophenone as the photoinitiator. Based on the major constituents being aliphatic, the Raman fingerprint of NOA materials are not expected to interfere with the Raman signals originating from the aromatic structure of the glucose capture ligand.

NOA materials are optically transparent which makes them a good candidate for transdermal biosensors. Once photocured, they form mechanically robust structures with modulus values up to 1 GPa. Three different versions of NOAs were chosen for fabricating the rigid polymer-based microneedles: NOA 61, NOA 65, and NOA 68. **Table 1** summarizes some of the characteristics of the NOA products that were used to prepare microneedle patches.

|	NOA 61	NOA 65	NOA 68
Composition	Mercapto ester (30-50 %) Triallyl isocyanurate (30-55 %)	Mercapto ester (30-50 %) Mercapto ester (30-55 %)	Mercapto ester (30-50 %) Mercapto ester (35-60 %) Tetrahydrofurfuryl methacrylate (15-25 %)
Viscosity at 25C (cps)	300	1200	5000
Refractive Index (cured polymer)	1.56	1.524	1.54
Modulus of Elasticity (GPa)	1.03	0.14	0.14
Elongation at Failure (%)	38	80	80

Table 1. Selected NOA products with corresponding chemical, physical and mechanical properties. Listed information provided by the supplier (Norland Products).

In brief, NOA microneedle arrays are prepared by filling the aforementioned PDMS molds with NOA, removing air bubbles by gentle vacuum, and curing the polymer by UV exposure. The solidified array is then removed from the mold. Scanning electron microscopy (SEM) images of the resultant pyramidal and conical microneedle are shown in **Figure 1**. The pyramidal needles are uniform across large areas. However, the conical mold was more difficult to fill with NOA, and resulted in defective or missing tips. These experiments served to inform which mold needle shape best operates with the NOA materials.
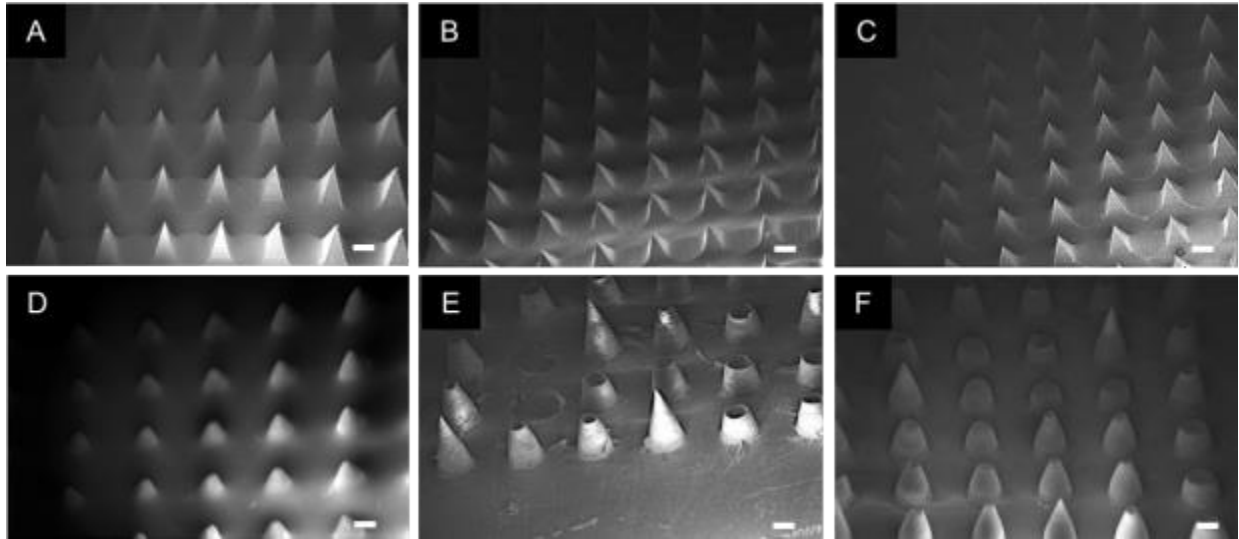
Figure 1. SEM micrographs of pyramidal and conical NOA microneedles. Materials made by using(A, D) NOA 61, (B, E) NOA 65 and (C, F) NOA 68. Scale bars: 200 μm

The next step for the biosensor preparation was the assembly of the SERS active component, AuNRs synthesized in the Van Duyne lab, on the microneedles surface. The AuNRs are stabilized with a cetyltrimethylammonium bromide (CTAB) bilayer in aqueous solution. The physisorbed CTAB bilayer on the Au surface limits the particle-microneedle surface interactions due to a stronger particle-particle interaction. Therefore, the electrostatic attraction between particles must be overcome to bring the particles closer to the surface in favor of subsequent particle deposition. This can be done by adjusting the ionic strength of the suspension solution. We centrifuged the
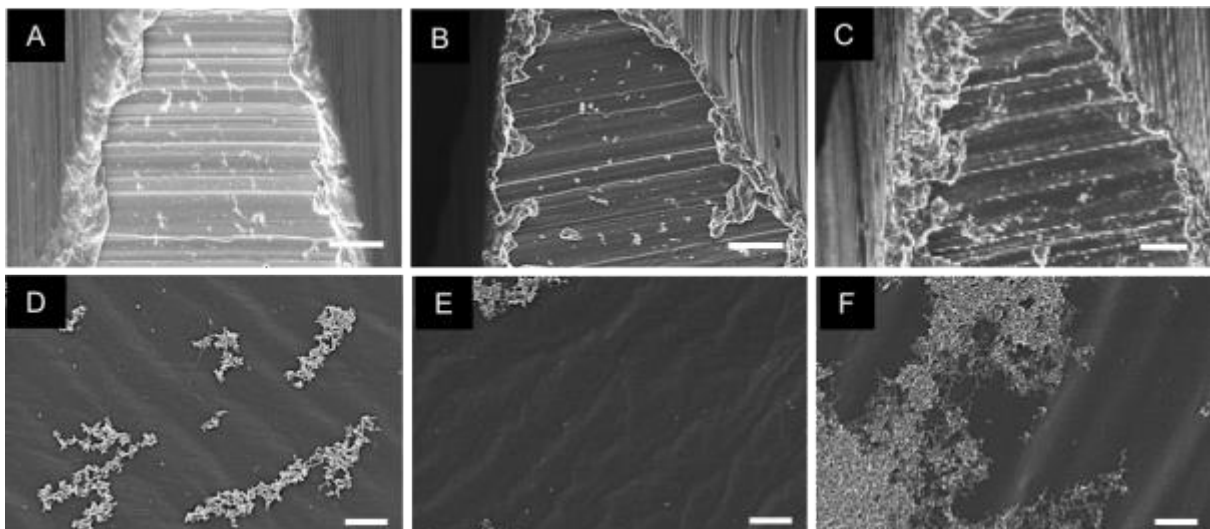
Figure 2. SEM micrographs of Au nanorods assemblies on NOA microneedles and flat films using (a, d) NOA 61, (b, e) NOA 65, and (c, f) NOA 68. Scale bars in (a, b, and c) are 10 μm. Scale bars in (d, e, and f) are 1 μm.

AuNRs suspension to remove the excess CTAB from the solution prior to re-suspending the AuNRs in a 5 mM NaCl aqueous solution. The NOA microneedles or flat NOA films (as a control) were then immersed in this particle suspension right after preparation. After incubating at room temperature for 2 hours, the samples were washed with deionized water to remove excess AuNRs. Investigation of the surface characterization for these samples by SEM revealed that AuNRs form large aggregates rather than individual AuNR monolayers on the NOA surface (**Figure 2**).

Raman scattering enhancement is highest when the excitation wavelength (785 nm) overlaps with theextinction maximum of the plasmonic material. The AuNRs synthesized by the Van Duyne lab for this project were optimized to have a solution-phase extinction maximum of ~783 nm However, this extinction maximum reflects the ensemble monomer spectrum in solution. Introduction of NaCl salt facilitated the AuNR assembly on both NOA microneedle surface and flat films, but there is evidence that doing so negatively affects the AuNR distribution on the surface.

AuNRs on the flat NOA surface demonstrated a quite different extinction spectrum than the characteristic plasmon bands in solution; two peaks were observed at 765 nm and 509 nm (**Figure 3**). This result may be caused by sedimenting pre-aggregated particles rather than individual particles onthe surface and leading to extinction of larger aggregates at longer wavelengths.

We expect the AuNRs to self-assemble as an individual monolayer if the NOA surface charge is modified, rather than introducing a solution-phase charge (NaCl). Subsequently, NOA surfaces were treated with oxygen plasma prior to incubation with AuNR solution. As shown in **Figures 3 and 4**, plasma treatment on the NOA film significantly promoted the monolayer particle assembly as implied by an absorption peak in the 700-800 nm region. According to the surface images and the UV-Vis extinction peak intensity, we also investigated a change in the density of the AuNRs in the monolayer when different versions of NOAs were used. We concluded that AuNRs assembly on the plasma treated NOA 61 and NOA 65 surfaces will give the maximum SERS activity among the studied NOA forms for detecting the Raman signals and subsequent glucose sensing.
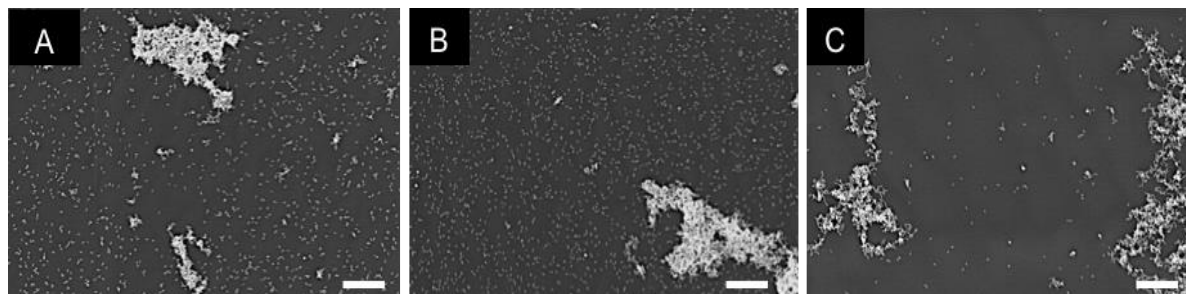
Figure 4. Structural characterization of plasmonic NOA surfaces. SEM micrographs of Au nanorods assembly on plasma treated flat NOA films using (a) NOA 61, (b) NOA 65, and (c) NOA 68. Scale bars are 1 μm.

We also have evaluated the option to directly evaporate metal on the polymer rather than grafting AuNRs onto the surface. We deposited Au over the NOA microneedles using physical vapor deposition. Three different thicknesses of Au (40, 70, and 100 nm) were deposited to initially

optimize the optical transparency, rigidity, and SERS enhancement at 785 nm. We confirmed the SERS activity of the Au-covered microneedle array, shown in **Figure 5**.
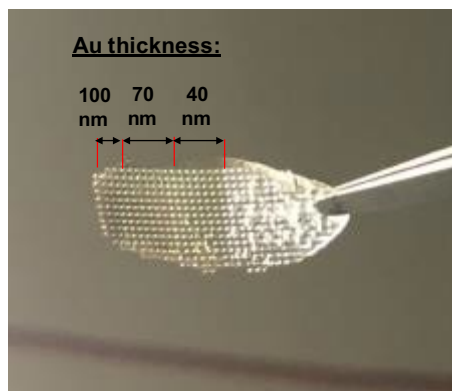

Figure 5. Picture of a metallized microneedle array. Au was deposited by physical layer deposition (PVD) with different thicknesses, as indicated on the image.

1.2.3 Solid hydrogel-based microneedles

Based on relevant biocompatibility studies in the literature, we have also worked with an acid anhydride copolymer containing alternating maleic anhydride and methyl vinyl ether groups. This material was purchased from International Specialty Products, NJ, under the tradename Gantrez AN-139. Gantrez is a non-toxic material [2] and exhibits antimicrobial properties when blended with PEG.[3] Donnelly et al. demonstrated various examples of Gantrez-PEG based microneedles for drug delivery and biosensing applications. [4-6]

We have focused on adapting the Gantrez-PEG blend chemistry to fabricate SERS active transdermal patches for glucose sensing. Incorporation of SERS active components, Au nanorods, as embedded within the polymer matrix was achieved by an easy particle dispersion in the pre-polymer solution and subsequent solidification of the matrix at elevated temperature (80 ˚C). The microneedles were fabricated by casting the pre-polymer solution on the PDMS mold and solidifying within the mold at high temperature (**Figure 6A**). The flat films were prepared on the flat surface. As the water content evaporates, carboxyl groups on the Gantrez and hydroxyl groups on the PEG chains goes through esterification reaction and finally the polymer matrix solidifies. The resulting patch became very rigid and the AuNRs assembly within the matrix exhibited light absorption features in the target 700-800 nm region (**Figure 6B**).
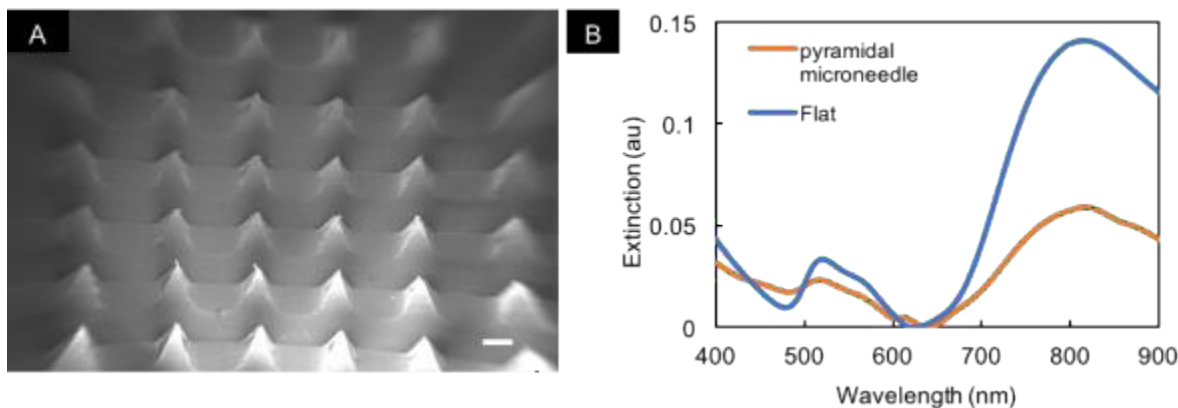
Figure 6. Characterization of solid plasmonic-PEG microneedles. A) SEM micrograph of Gantrez-PEG pyramidal microneedles. Scale bar is 200 μm. B) UV-vis extinction spectra of Au nanorods assembly embedded in the Gantrez-PEG hydrogel with pyramidal microneedles and flat film.

2. GLUCOSE CAPTURE LAYER SYNTHESIS

2.1 Boronic acids

2.1.1 Bisboronic acid synthesis and product quality check

We began with an in-depth characterization of the bisboronic acid glucose capture layer reported in our 2016 publication.[7] Additionally, we have implemented a quality check protocol to ensure high synthetic batch-to-batch reproducibility.

After synthesizing 1,1-bisboronic acid (1,1-BBA) in the Mrksich lab, its binding constant (K) with glucose was evaluated in PBS buffer (pH 7.4) as a systematic quality check in the Van Duyne lab. To determine the K, a UV-vis titration study was done by varying the concentration of glucose (0-1000 mM) at a constant 1,1-BBA concentration. Two absorbance peaks of 1,1-BBA (206 and 245 nm) are observable in the UV region (**Figure 7A**). As the concentration of glucose increased there was a blue shift for the peak at 245 nm and the signal intensity decreased. The resulting data was fitted to a Langmuir isotherm model (**Figure 7B**) and the binding constant of 1,1-BBA in PBS bufferdetermined to be 158 M^{-1}. For comparison, the binding constant of 4-mercaptophenylboronic acid (4-MPBA), a commonly used monoboronic acid used to bind glucose, was determined to be around only50 M^{-1}.

In addition to UV-vis titrations, normal Raman spectra of each batch of 1,1-BBA were collected to ensure that each batch was molecularly identical. Following these checks, 1,1-BBA was used to functionalize SERS-active substrates for glucose sensing.
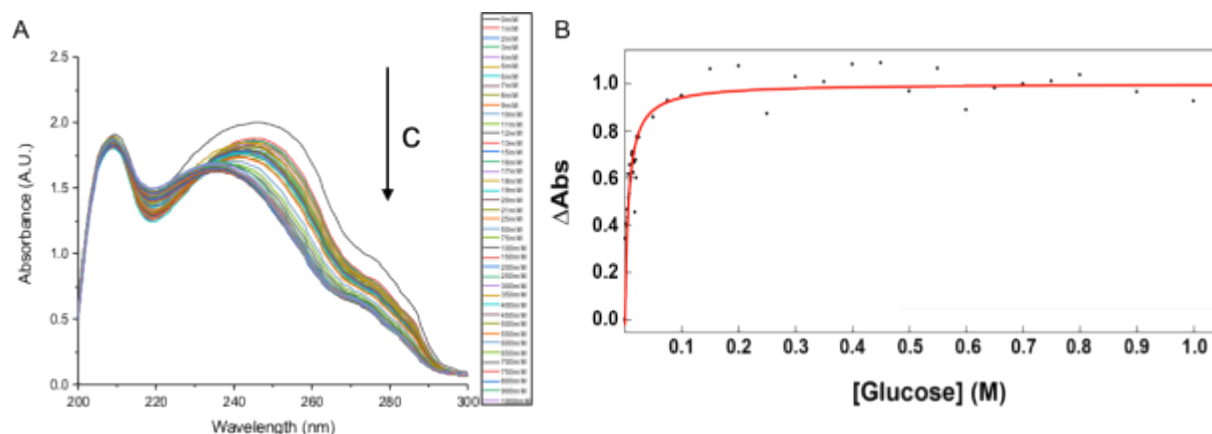
Figure 7. Confirmation of glucose binding to 1,1-BBA by UV-vis spectroscopy. (A). UV-vis spectra of the concentration dependent binding of 1,1-BBA with glucose in 10% MeOH/PBS at pH 7.4, B) Langmuir isotherm of 1,1-BBA binding interaction with glucose.

2.1.2 Monoboronic acids modification

Subsequent testing of batches of 1,1-BBA led to inconsistent measurement of glucose with SERS. As potential alternatives, the following monoboronic acid derivatives (**Figure 8**) were considered as potential trial compounds for optimizing our glucose sensing platform, described further in section 3. The parameters we wished to optimize are the binding constant and selectivity over fructose. Each of these derivatives retains the electron-withdrawing fluorine group of 1,1-BBA that allows for sensing of glucose at physiological pH.

By minimizing the distance between the boronic acid receptor and the surface-binding thiol, we can maximize the Raman signal enhancement, which is distance dependent. Additionally, the pinacol boronic ester glucose duplex (**Figure 8A**) should enable direct detection of glucose Raman peaks, which will serve as a reference for directly detecting glucose using shorter capture agents (**Figure 8B and C**).
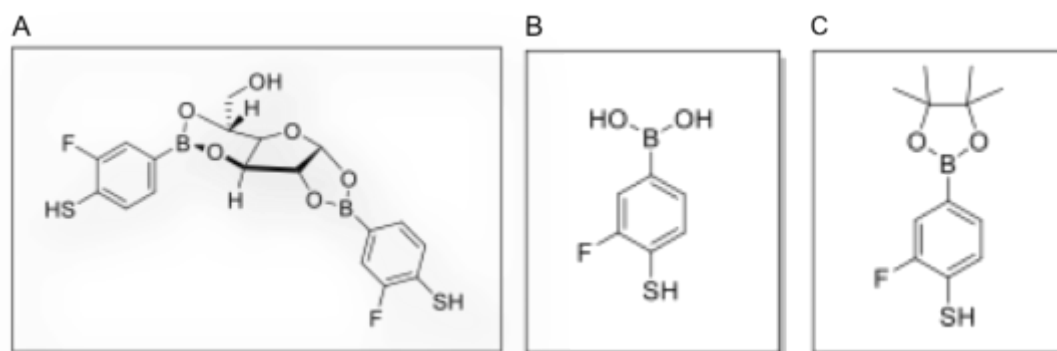
Figure 8. **Monoboronic acid derivatives** identified as alternative capture layers to bisboronic acids.

3. NANOSENSOR FUNCTIONALIZATION WITH CAPTURE LAYERS AND SERS EVALUATION

## 3.1 AuNRs/AuFONs functionalization and SERS measurement

3.1.1 Performance evaluation for SERS substrates

AuFONs and AuNRs are the two plasmonic substrates used in our SERS nanosensors. Both are highly robust and reproducible substrates with high enhancing capabilities whose fabrication production can be scaled up for large distribution. Importantly, the surface chemistry of both AuFONs and AuNRs can be easily tuned by functionalizing the surface with different ligands, making them ideal SERS substrates for biosensing and subsequent functionalization with anti-biofouling layers.

AuNRs and AuFONs were both fabricated so that their localized surface plasmon resonance (LSPR), or extinction maximum, were optimized for 785 nm excitation wavelength through tuning of metal thickness and underlying microspheres diameter (for AuFONs) and aspect ratio (AuNRs, $\sim$ 45 nm by 15 nm).

The SERS activity of the AuNRs was confirmed in the Van Duyne lab by functionalizing the surface with a water-soluble Raman reporter, 4-MBA, and subsequently measuring the SERS spectrum with a 785 nm excitation wavelength (**Figure 9**). The peaks observed on the SERS spectrum at 1078 and 1590 cm^{-1} represent the two dominant ring vibrational modes of 4-MBA. The average enhancement factor (EF) of the 785-nm optimized AuNRs was calculated to be 4×10^4.

Although lower than that of AuFONs, the EF can be increased by aggregating nanorods into dimers and trimers, creating electromagnetic hotspots known to considerably boost the SERS signal.[2] We therefore pursued controlling the aggregation of nanorods when deposited onto microneedles patches, both in solid microneedles and hydrogel approaches, described below. The SERS activity was confirmed using 1,2-bis(2-pyridyl)ethylene (BPE), a non-resonant Raman reporter molecule commonly usedin the Van Duyne lab to confirm the SERS activity of plasmonic substrates.
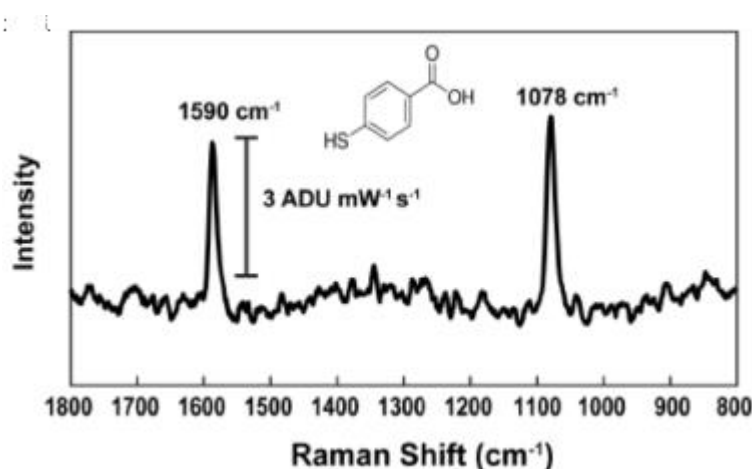

Figure 9. Confirmation of SERS activity by AuNRs used as plasmonic nanosensors. SERS spectrum of 4-MBA on AuNRs (20x ELWD objective, λ_{ex} = 785 nm, Savitsky-Golay filtering and baseline correction)

3.1.2 Glucose cross-section measurements

The importance of glucose in metabolic disorders has led to many researchers attempting to quantify glucose concentration *in vivo* using Raman scattering techniques, including by stimulated Raman scattering (SRS) microscopy. As normal Raman scattering (NRS) studies of glucose showed very weak scattering, surface-enhanced Raman scattering (SERS) and coherent Raman scattering techniques were used to enhance the low overall NRS signal (**Figure 10**). Unfortunately, previous research either cites a literature value of the differential Raman scattering cross-section (DRSC) that references unpublished and non-peer reviewed data for the DRSC of the 1126 cm^{-1} mode of glucose, or simply omits the exact value.

To resolve this issue, we utilized femtosecond stimulated Raman scattering (FSRS) to quantitatively determine its DSRCs using both stimulated Raman loss (SRL) and stimulated Raman gain (SRG) simultaneously (**Figure 10**). Using the two analogous FSRS techniques, SRG and SRL, we determine that the DRSCs of glucose excited at 514.5 nm range from a low of 5.0 ± 1.1 x 10^{-30} to a high of 8.9 ± 0.9 x 10^{-30} cm^2 molecule^{-1} sr^{-1}.
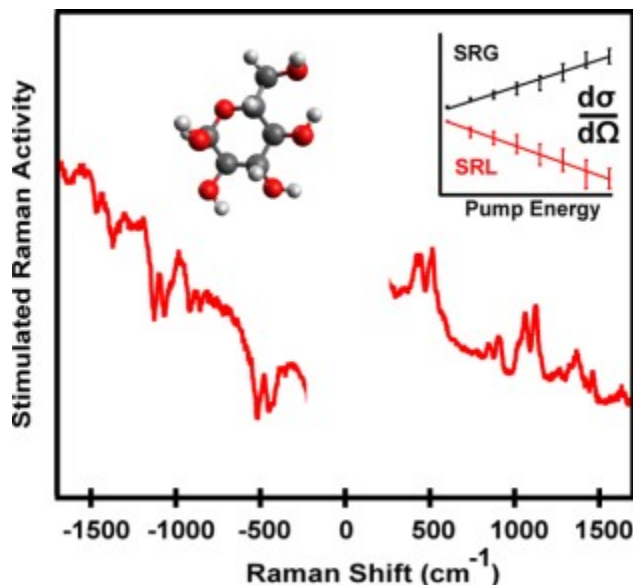
Figure 10. Determination of glucose Raman section. The DRSC of multiple vibrational modes of glucose was determined for the first time using FSRS. In the FSRS approach, SRL and SRG spectra were obtained simultaneously, then a linear regression was performed on the pump energy dependent stimulated Raman activity.

Based on this measurement, we can confidently evaluate the DRSC for 1124 cm^{-1} mode of glucose at 785 nm excitation to be ~ 1.05 x 10^{-30} cm^2.molecule^{-1}.sr^{-1}. This work established both the compatibility of SRL for measuring DRSCs and values for the DRSC of multiple vibrational modes of glucose, something of direct interest to the PRMRP effort. These results were published in Analytical Chemistry.[8]

3.1.3 Evaluating monoboronic acid derivatives for glucose recognition

Phenylboronic acids (PBAs) are small molecules widely reported to reversibly bind glucose. The mechanism through which PBAs interact with glucose is an esterification of the hydroxyl groups of the diols through bonding with the boron of the PBA, further forming cyclic boronate esters. Boronic acids can exist in either neutral trigonal forms or anionic tetrahedral forms, depending on the pH of the environment. The binding constant of anionic tetrahedral boronate ester for glucose is higher than that of the trigonal boronate esters. Thus, the pK_a of the PBA should ideally be lower than the pH of the environment.[9]

To understand the binding interaction of PBAs with glucose and quantitatively detect glucose using SERS, 4-mercaptophenylboronic acid (4-MPBA), the simplest and commercially available PBA, was used. In addition to 4-MPBA, we also used fluorinated 4-MPBA synthesized in the Mrksich lab to investigate glucose binding. With the electron-withdrawing fluorine group, the fluorinated 4-MPBA allows sensing glucose at physiological pH.

3.1.3.1 4-MPBA and fluorinated 4-MPBA

Density functional theory (DFT) calculations of the normal Raman of 4-MPBA with and without glucose binding show clear spectral changes of 4-MPBA upon glucose binding (**Figure 11**). We then verified the binding interaction with glucose in solution. To determine the glucose binding constant (K_a) of 4-MPBA in solution, a UV-visible spectrophotometric titration study was done by varying the concentration of glucose (0-900 mM) at a constant 4-MPBA concentration in pH 10 buffer (**Figure 12A**). With a pK_a value of 9, the binding interaction of 4-MPBA with glucose works best in basic conditions.[9] As the concentration of glucose increased the shoulder peaks at 263 nm and 292 nm increased and decreased, respectively. As shown in **Figure 12B**, the data was fitted to a Langmuir isotherm model and the binding constant of 4-MPBA for glucose in pH 10 was determined to be 90 M^{-1}. To check the glucose binding interaction on the surface, SERS of 4-MPBA functionalized on a plasmonic substrate was measured in pH 10 buffer solution and saturated glucose solution in a flow cell (**Figure 12C**). A new peak at 1574 cm^{-1} appeared in the SERS spectrum taken in pH 10 buffer. This peak represents the anionic tetrahedral-form of boronic acid.[10] However, no glucose Raman peaks (direct evidence) or peak shifts (indirect evidence) in the SERS data was observed upon introducing saturated glucose solution. SERS of fluorinated 4-MPBA before and after introducing glucose solution also did not show direct or indirect evidence of glucose binding.
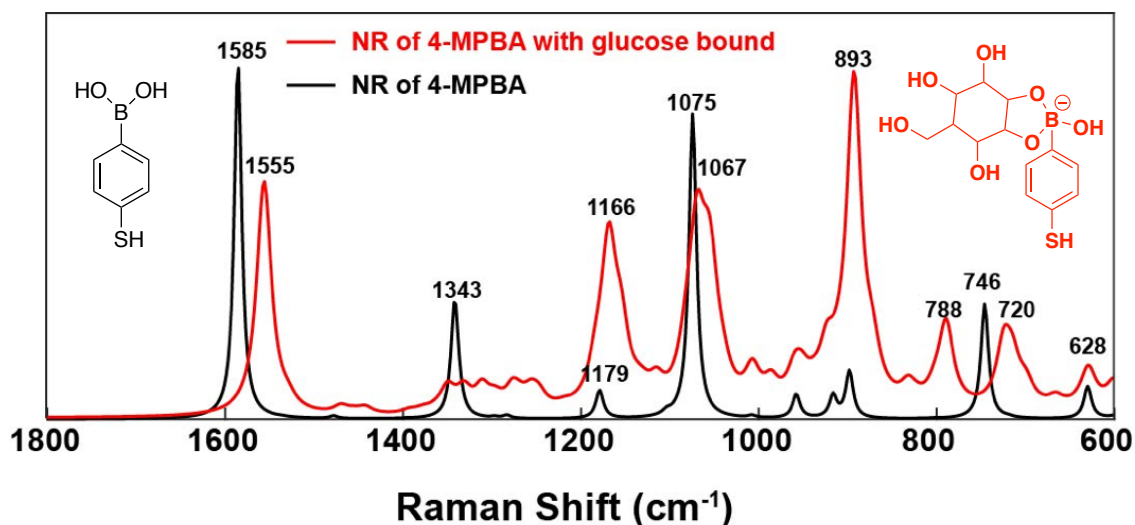
**Figure 11.** DFT calculations for normal Raman of 4-MPBA complexed with (red) and without (black) glucose.
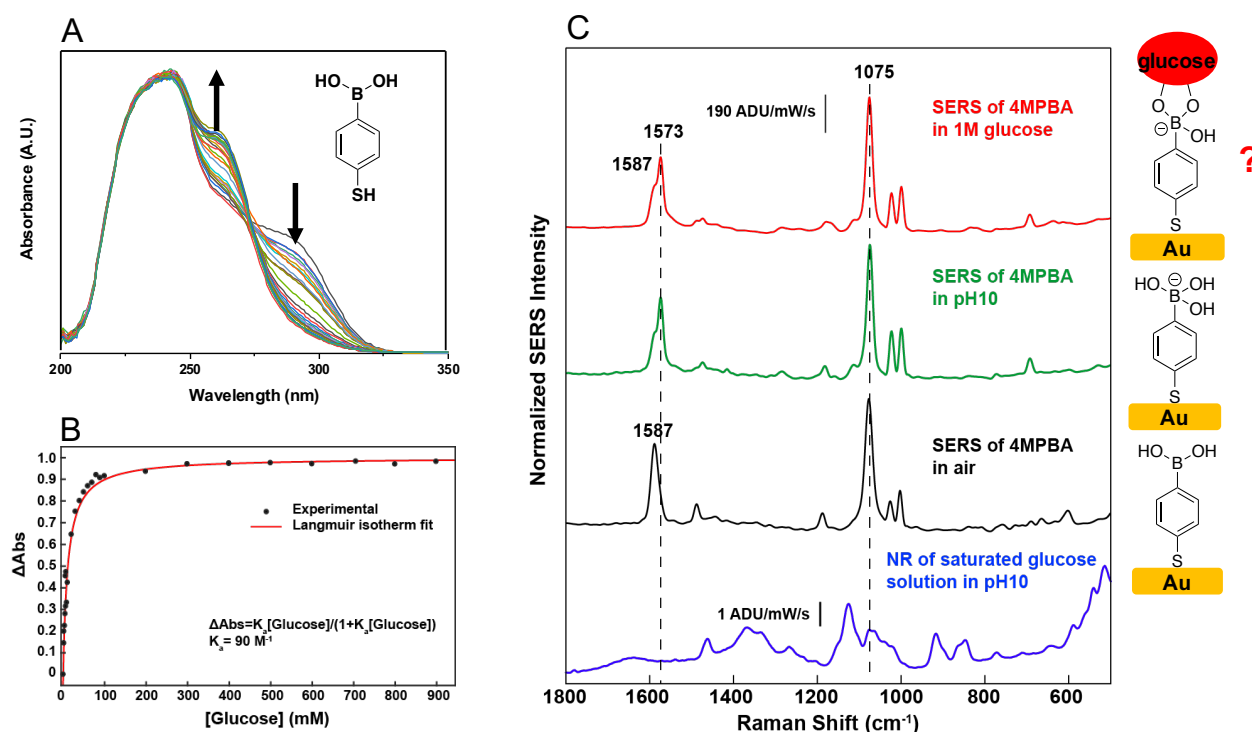
Figure 12. 4-MPBA binding interaction with glucose (A-B) in solution using UV-visible spectroscopy and (**C**) on a plasmonic substrate surface using SERS. (**A**) UV-vis spectra of 4-MPBA as change in glucose concentration 10% EtOH/pH 10 buffer, (**B**) Langmuir isotherm of 4-MPBA binding interaction with glucose, (**C**) SERS spectrum of 4-MPBA on a AuNR substrate before and after adding saturated glucose solution in pH 10 buffer. SERS spectra were normalized to the peak at 1075 cm^{-1} and are an average of seven spectra collected using a 20x ELWD objective, $P_{ex} = 400$ µW, $\lambda_{ex} = 785$ nm, Savitsky-Golay filtering and baseline correction).

16

Previous work has observed boronic acids cross-linking with other boronic acids thus preventing from glucose binding.[10,11] To address this possibility, protecting 4-MPBA with pinacol ester or adding spacer molecules was an alternative method for glucose detection.

3.1.3.2 Pinacol ester protected 4-MPBA

Pinacol ester protected 4-MPBA was synthesized in the Mrksich lab (**Figure 13A**). The normal Raman spectra of 4-MPBA with and without pinacol ester were taken for comparison and there were spectral differences in the lower and higher wavenumber ranges (**Figure 13A-B**). Most importantly, the normal Raman of pinacol ester protected 4-MPBA showed an aliphatic C-H stretch at 2979 cm^{-1}, which was evidence for pinacol ester. We then immobilized pinacol ester protected 4-MPBA on a SERS substrate, removed pinacol ester by hydrolysis, and introduced concentrated glucose solution. Similar to 4-MPBA a shoulder peak near 1576 cm^{-1} appeared after incubating the substrate in pH 10 buffer (**Figure 14**). However, there was no direct or indirect evidence of glucose binding when the saturated glucose solution was introduced.
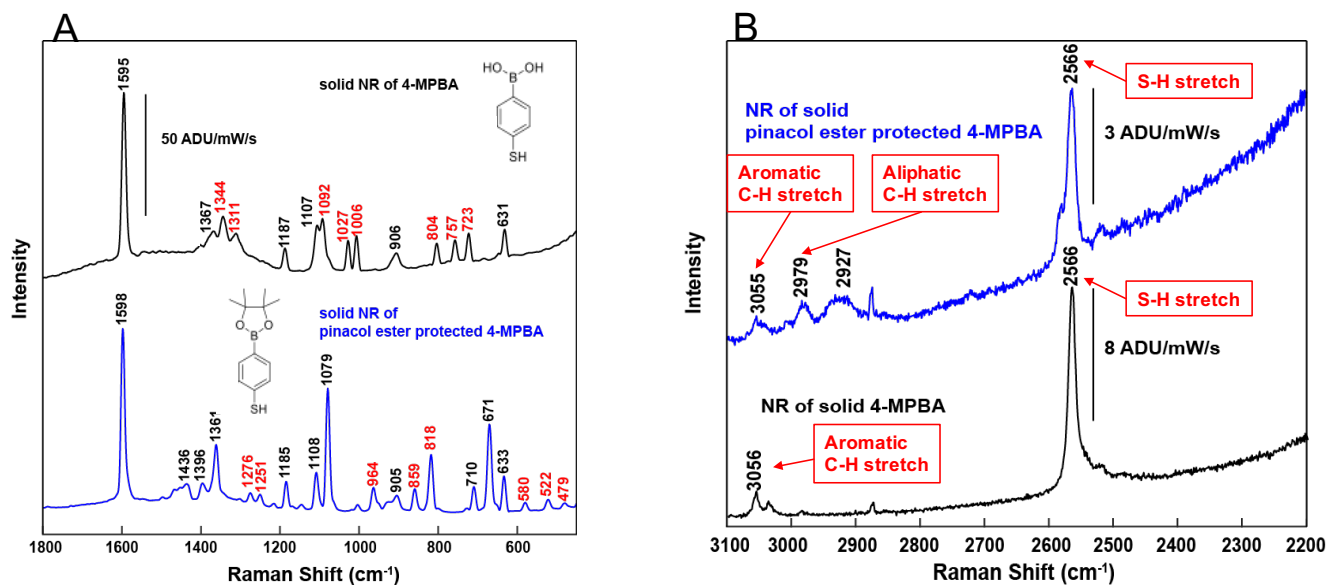
Figure 13. Normal Raman of solid 4-MPBA and pinacol ester protected 4-MPBA in the (A) lower and (B) high wavenumber range (λ_{ex} = 785 nm, 20x ELWD objective, P$_{ex}$ = 3 mW, t$_{aq}$ = 1 min).

17
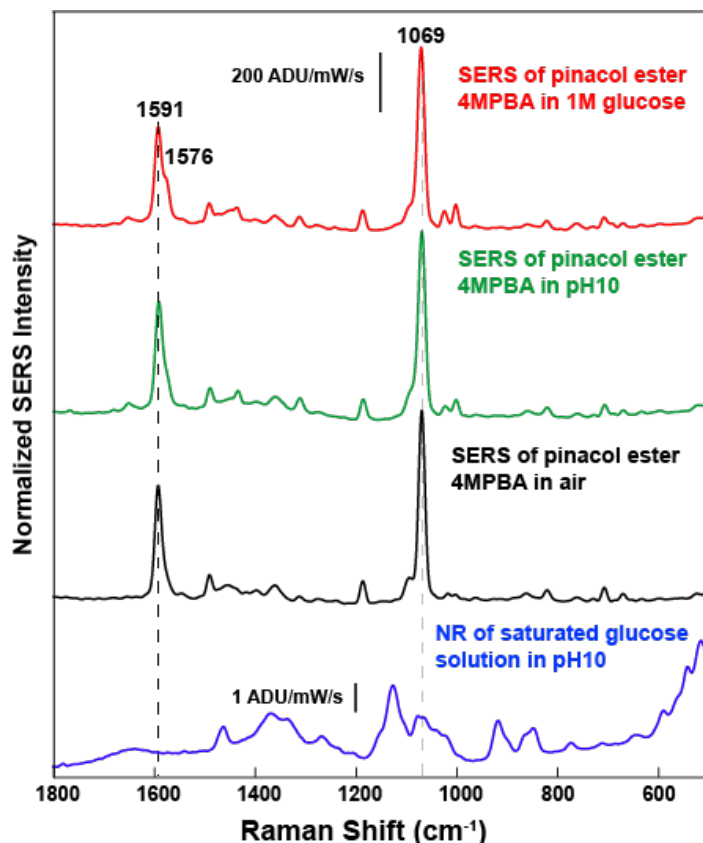
Figure 14. SERS spectra of pinacol ester protected 4-MPBA functionalized on SERS substrate for glucose sensing after removing piancol ester (from bottom to top: normal Raman of saturated glucose solution in pH 10, SERS of pinacol ester protected 4-MPBA in air, in pH 10, and in 1M glucose solution in pH 10, average of seven spectra collected using 20x ELWD objective, P_{ex} = 400 μW, t_{aq} = 1 min, λ_{ex} = 785 nm, Savitsky-Golay filtering and baseline correction).

3.1.3.3 Spacer molecules for preventing cross-linking between boronic acids

As an alternative method to solve the challenge of cross-linking between PBAs on the plasmonic nanomaterial surface, we tried a mixed self-assembled monolayer (SAM) consisting of various thiol molecules acting as a spacer molecule and 4-MPBA as the glucose capture ligand. We chose alkanethiols (octanethiol and decanethiol), adamantanethiol, benzenethiol (BZT), and mercaptobenzoic acid (4-MBA) as spacer molecules and varied the ratio between the spacer molecule and 4-MPBA on a SERS substrate. After functionalizing a mixed SAM (a spacer molecule and 4-MPBA) on a SERS substrate, Au film-over-nanospheres (AuFON), at various ratios, we incubated them in pH 10 buffer and then in a saturated glucose solution in a flow cell. The resulting SERS spectra showed no change in peak position or new peaks. Although we observed both the spacer molecule and 4-MPBA functionalized on AuFON with SERS, the spacer molecules were not optimal for promoting glucose binding. To eliminate the possibility of PBAs cross-linking and observe glucose fingerprint when bound to 4-MPBA as a reference, the Mrksich lab synthesized a complex where two 4-MPBA molecules bonded to one glucose molecule.

18

3.1.3.4 4-MPBA glucose complex

To fundamentally understand the binding interaction of 4-MPBA with glucose to try to answer the question of why we observe evidence that 4-MPBA binds glucose in solution via UV-vis spectrophotometry, but we cannot detect that binding via SERS, we investigated a complex where 4-MPBA was pre-bound to glucose (**Figure 15A**). The NMR of the complex showed the evidence of glucose directly bound to two 4-MPBA molecules. Additionally, there was a broad peak at 2926 cm^{-1} in the normal Raman spectrum of the solid, possibly representing glucose (**Figure 15B**).
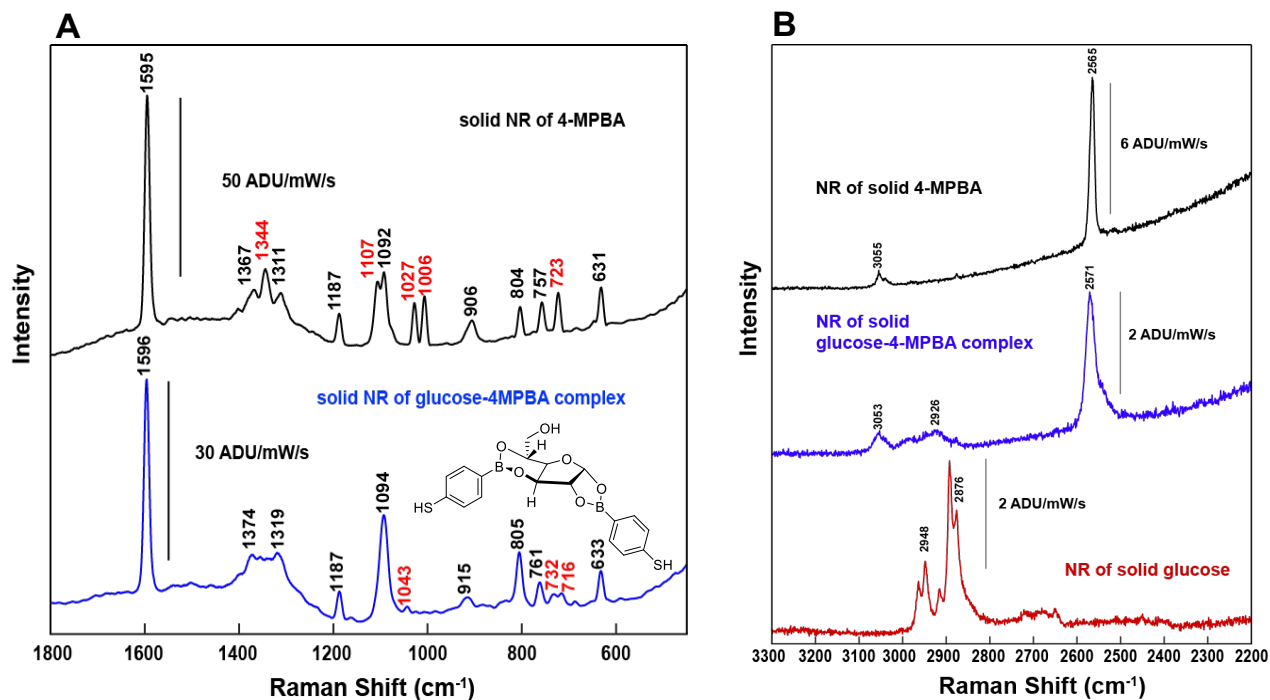
Figure 15. Normal Raman of solid 4-MPBA and glucose-4-MPBA complex in the (A) lower and (B) higher wavenumber range with solid glucose normal Raman (λ_{ex} = 785 nm, 20x ELWD objective, P_{ex} = 8 mW, t = 1 min).
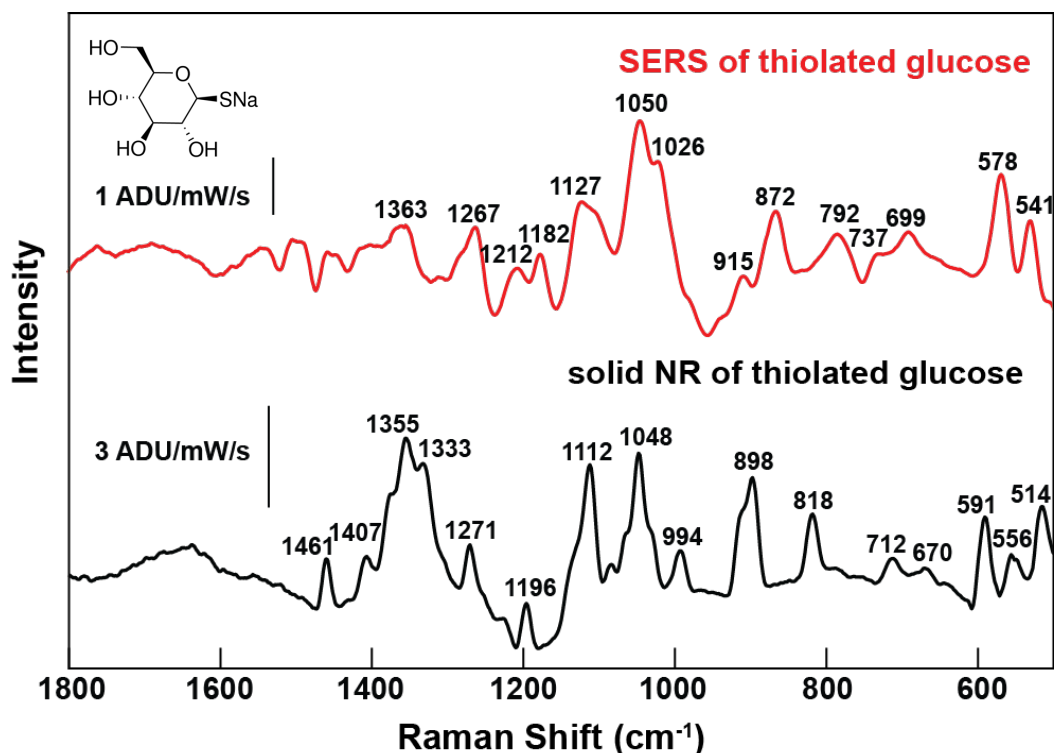
Then we functionalized a SERS substrate with the complex and SERS spectra were collected in air (**Figure 16**). We used anhydrous ethanol to dissolve the complex and incubate our SERS substrate to prevent glucose possibly detaching from 4-MPBA by hydrolysis of the boronate groups. The resulting SERS data did not show the dominant glucose peak expected around ~1126 cm^{-1} based on the normal Raman of glucose or any other direct evidence. The substrate was then rinsed with water to remove glucose in the complex by hydrolysis. Similar to 4-MPBA SERS data, a new peak at 1572 cm^{-1} appeared. This result only showed the evidence of the tetrahedral form of 4-MPBA, but not a direct or indirect evidence of glucose. We hypothesize that either glucose bound on the complex dissociated when the complex was functionalized on the surface or glucose molecule is a weak Raman scatterer that we cannot not observe with SERS.

19
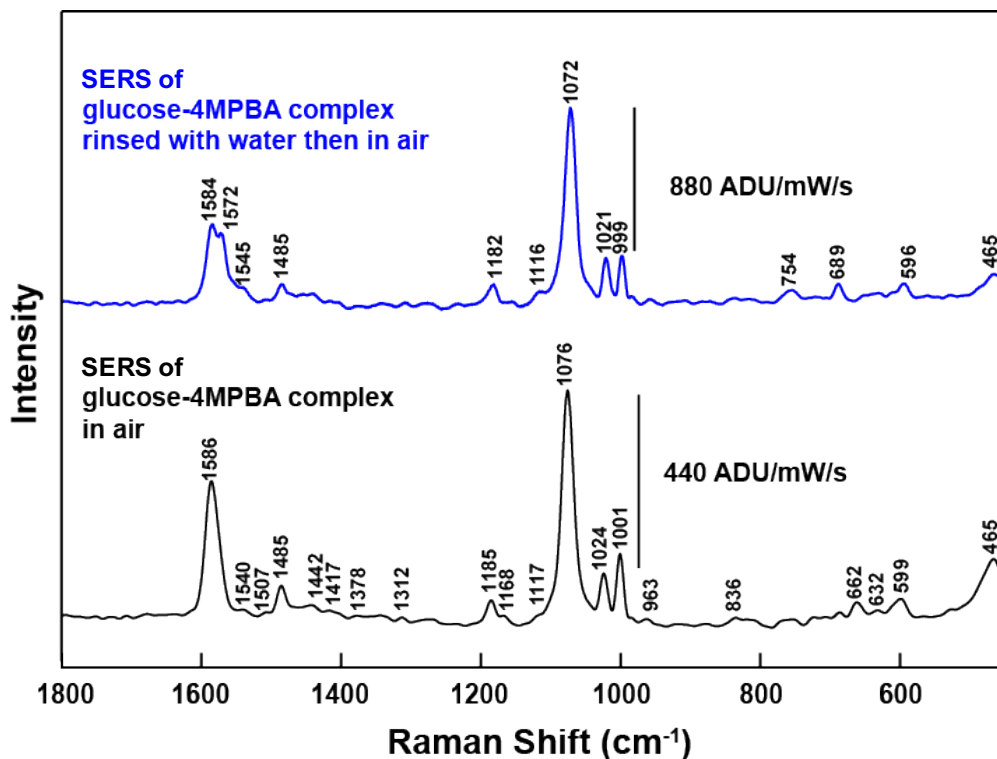
Figure 16. SERS glucose-4-MPBA complex functionalized on a SERS substrate measured in air (black) and after rinsing with water (blue) (Average of seven spectra using 20x ELWD objective, $P_{ex} = 400\ \mu W$, t = 1 min, $\lambda_{ex} = 785$ nm, with Savitsky-Golay filtering and baseline correction).

3.1.3.5 Direct glucose sensing with SERS using thiolated glucose (1-Thio-β-D-glucose sodium salt)

Because we did not observe any direct evidence of glucose, we postulated that it could be due to the relatively low Raman cross section of glucose, rather than a problem of the capture ligands not binding glucose. To investigate this possibility, we tried detecting 1-thio-β-D-glucose sodium salt (thiolated glucose) with SERS. Thiolated glucose will form a gold-thiolate bond, eliminating the distance dependence issue and the requirement for a capture ligand (as glucose itself does not adsorb to metal surfaces) Our hypothesis is that if we could directly detect glucose using SERS, the difficulty in glucose detection can be narrowed down to the glucose capture ligands. Thus, SERS spectrum was taken after functionalizing thiolated glucose onto a SERS substrate. We observed the SERS of thiolated glucose as shown in **Figure 17**. The SERS spectrum matched the normal Raman, the SERS data in the literature[12], and the DFT calculation of thiolated glucose. Therefore, it appears that the barrier to detecting glucose by SERS is most likely the efficacy of the capture agents to bind glucose when the capture agents are immobilized on a surface. To investigate the capture ligand for glucose binding on surface, we then tried a sandwich assay where we added another PBA that could bind to the other side of glucose with a distinct Raman fingerprint.

Figure 17. SERS of thiolated glucose functionalized on a SERS substrate and the normal Raman of thiolated glucose measured with a macro Raman set-up (λ_{ex} = 785 nm, P_{ex} = 3 mW for normal Raman and 30 mW for SERS, t_{aq} = 3 min, with Savitsky-Golay filtering and baseline correction).

3.1.3.6 Sandwiching glucose between two boronic acids

It is reported that PBAs reversibly bind with cis-1,2- or 1,3-diols.[9] Among various configurations of glucose at equilibrium, one glucose configuration has two syn-periplanar diols that could potentially bind with two PBAs (**Figure 18**).[9] With two pairs of syn-periplanar diols for glucose, Chen et al. detected glucose using a sandwich assay where 4-MPBA on the surface bond with one of glucose diols and 4-cyanophenylboronic acid (4-CPBA) bond with the diols on the other side.[13] Since the cyano group has a Raman peak at around 2200 cm^{-1}, they were able to observe the CN mode in the resulting SERS spectrum. Thus, we tried capturing glucose by sandwiching the molecule in between 4-MPBA functionalized on SERS substrate and 4-CPBA. However, there was no direct or indirect evidence of glucose or indication of CN mode in the resulting SERS spectrum. A possible reasoning for not observing the CN mode is that the glucose configuration consists of two syn-periplanar form is present at a small percentage (~0.14%) of the total configurations.

Figure 18. Glucose configurations in the dominant form (left) and the form with two syn-periplanar diols (right).[9]

We tested 4-MPBA binding interaction with molecules with diols, such as fructose. Surprisingly, the binding constant of 4-MPBA with glucose in solution was similar to that of fructose obtained by UV-visible titration study. According to the literature, the binding constant should be about 40 times higher for fructose than that of glucose.[9] Although we observed a binding trend of 4-MPBA for glucose, we could not observe a direct or indirect evidence of glucose detection. A report of a UV-vis titration study of porphyrin with glucose showed a binding trend similar to that of 4-MPBA with glucose, but they did not observe a direct evidence of glucose binding to the porphyrin.[14] They mentioned that the binding trend from the UV-vis titration study could be due to aggregation of the capture ligand, not from the binding.

3.2 Comparative evaluation of label-free optical plasmonic sensors

To further evaluate combinations of binding ligands and nanostructures, we aimed to compare surface plasmon behavior of various metallic nanostructures and furthermore to develop plasmonic based glucose sensors. We split this part of the study into parts; i) utilizing the local surface plasmons resonance (LSPR) behaviors of colloidal nanostructures to develop label-free colloidal plasmonic nano sensors, and ii) utilizing the surface enhanced Raman scattering to develop SERS based sensors. For this purpose, we synthesized two types of gold (Au) nanostructures; Au nanorods (Au NRs) and Au nanoflowers (Au NFs) and utilized them to develop the designated nano sensors. For the LSPR-based sensing work, we used ultraviolet-visible (UV-vis.) extinction spectroscopy using a commercial instrument (BECKMAN COULTER; DU 800). We used a commercial instrument (HORIBA LabRAM HR Evolution Confocal RAMAN) for SERS measurements. **Figure 19** depicts the fundamental behaviors of LSPR, and SERS-based mechanisms that can be integrated for sensing of various chemical and biological analytes.
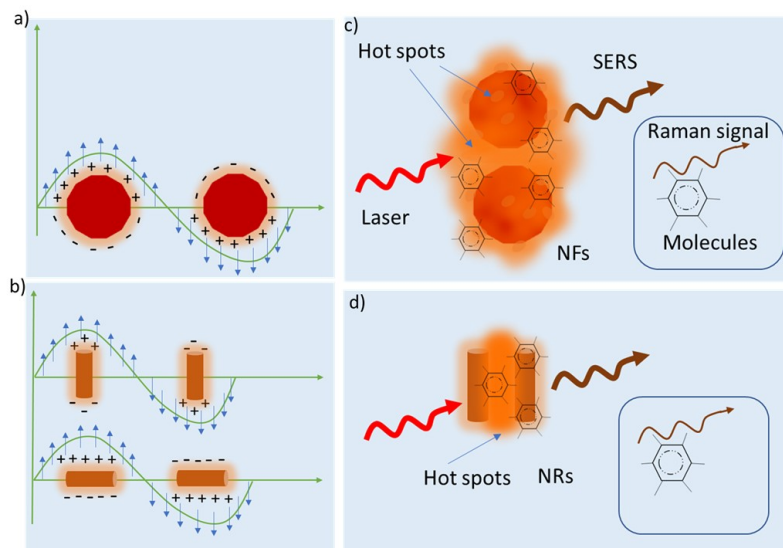
Figure 19. Conceptual depictions of LSPR and SERS phenomena. (a,b) Schematic representations of LSPR effects of Au NFs and Au NRs. Conductive electrons of NFs and NRs are excited into collective oscillation to generate highly localized electromagnetic fields in the metal-molecules dielectric interfaces with irradiation of light. NRs generate longitudinal (upper panel of b) and transverse (lower panel of b) oscillations. Such oscillation can be altered with changing the dielectric environment by analyte molecules. (c,d) Schematic diagram showing the SERS phenomenon; Au nanostructures-molecules interactions lead to the mutual excitation of Raman signal from molecules and generates enhanced Raman signals of analyte molecules.

3.2.1 LSPR based sensing techniques

The utilization of LSPR behavior of metallic nanostructures (NSs) can be a novel and effective approach in bio/chemical molecular sensing applications. The change in the local dielectric environment of nanostructures from the binding with bio/chemical analytes can cause the LSPR spectral shift. Systematic monitoring of such LSPR spectral shift as a function of the concentration of bio/chemical analytes can lead to the development of economical, easy, and effective bio/chemical sensing technology. In this work, we carried out a comparative study of the sensing potential of colloidal metallic NSs including Au NRs and Au NFs. For the development of glucose sensor, glucose molecules have poor affinity to bind to the metallic surface due to a lack of bonding. Hence, we chose various types of linker molecules previously used by our labs and others, such as 4-mecraptobenzoic acid (4-MBA), 4-mercaptophenylboronic acid (4-MPBA), 6-mercapto-1-hexanol (MH), 1-decanethiol (DT) and 4-mercaptophenol (4-MCP), to improve affinity of glucose molecules relative to unmodified metallic surfaces. These linker molecules can bind to the chosen metallic NSs via thiol-bonding and open an opportunity for hydrogen bonding to glucose. Indeed, these linker molecules initiate the manipulation of the local dielectric environment of suspended NSs, which can be further modified with added glucose concentrations, hence a colloidal glucose sensor can be derived. Our recent study presents a comparative monitoring of LSPR behaviors of 4-MBA, 4-MBPA, DT modified colloidal NRs, with varying the glucose concentration, measuring their extinction spectra based on UV-vis absorption.

3.2.1.1 LSPR-based sensor design/fabrication

We synthesized Au NRs and NFs using previously published chemical synthesis methods. We followed a similar process to a silver-assisted seed-mediated method to synthesize Au NRs.[10-13] Au seeds were prepared by mixing 0.25 mL of gold chloride trihydrate [HAuCl$_4$.3H$_2$O] (0.01M), 9.75 mL of cetyltrimethylammonium bromide (CTAB) solution (0.1 M), 600 uL of ice-cold sodium borohydride [NABH$_4$] (0.01 M) under vigorous stirring (1000 RPM) for 1 hr. We then added 24 uL of seeds after 2 hrs of seed aging to the Au NRs growth solution, and the solution was kept overnight for purification. The growth solution was prepared with mixing of 9.11 mL of CTAB solution (0.1 M), 130 uL of silver nitrate [AgNO$_3$] solution (0.01 M), 0.5 mL of HAuCl$_4$.3H$_2$O (0.01M), 190 uL of hydrogen chloride [HCl] (1 M), 80 uL of ascorbic acid (0.1 M) under gentle stirring (500 RPM). Au NRs solution was centrifuged twice at 10,000 rcf speed for 30 min of each, and supernatant was removed. Finally, obtained sediments were redispersed in the same volume of Milli-Q water.

We followed a one-step seedless chemical preparation method to synthesize Au NFs.[14] The Au NFs were prepared with mixing of 0.64 mL of Hydroxylamine hydrochloride [NH$_2$OH·HCl] (0.1 M), 1 mL of C$_6$H$_5$Na$_3$O$_7$.2H$_2$O [trisodium citrate dihydrate] (0.1 M), 0.8 mL of sodium hydroxide [NaOH] (0.1 M) and 1 mL of HAuCl$_4$.3H2O (0.01M) in 20 mL of Milli-Q water under vigorous stirring (~900 RPM) for 1 min. This growth mechanism corresponds to the instantaneous nucleation of seeds with anisotropic structures and the fast growth process supports the growing of flower-like structures with the formation of petals-like structures. The presence of citrate and chloride ions on the Au surface could be the reason for the anisotropic growing during the rapid growth process. To keep the synthesized NFs stable for many days, we further mixed 0.25 mL of polyvinylchloride (final concentration 13.5 uM) to the mixture under continuous stirring for 30 sec. Without further purification, Au NFs were used for sensing experiments described below.

Both Au NRs and NFs colloidal solutions were stored in closed tubes covered with aluminum foil to protect from light. We prepared the 1 mM solution of the various linker molecules as shown in **Figure 20**; and nanostructures are incubated in that solution for ~3 hours so that they can form thiol bonds at the Au surface and provide opportunity for binding with glucose.
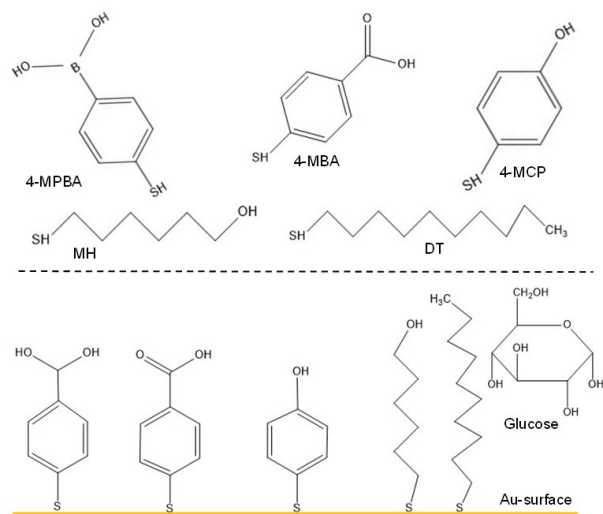
Figure 20. LSPR-based sensor design with the use of different linker molecules. The upper panel represents various linker molecules to be used to functionalize Au nanostructures, and the lower panel represents the thiol bonding of such molecules on the Au surfaces.

### 3.2.1.2 Characterization of the Au NRs and NFs

We characterized the synthesized nanostructures with light extinction spectra with a UV-vis spectrometer as shown in **Figure 21**. **Figure 21a** compiles the UV-vis absorption measurements of a few varieties of synthesized Au NRs. The clearly distinct two peaks in these spectra indicate the transverse and longitudinal plasmonic resonance peaks. The observation of these plasmonic peaks is also the indirect conformation of rod-like nanostructures as compared to the many reports.[10-13] The variation in the plasmonic peaks is mainly associated with the seeds' aging time. The stirring speed during the seed aging also alters the peaks. In contrast, broad absorption spectra shown in **Figure 21b** is associated with the plasmonic resonance of Au NFs.[14]
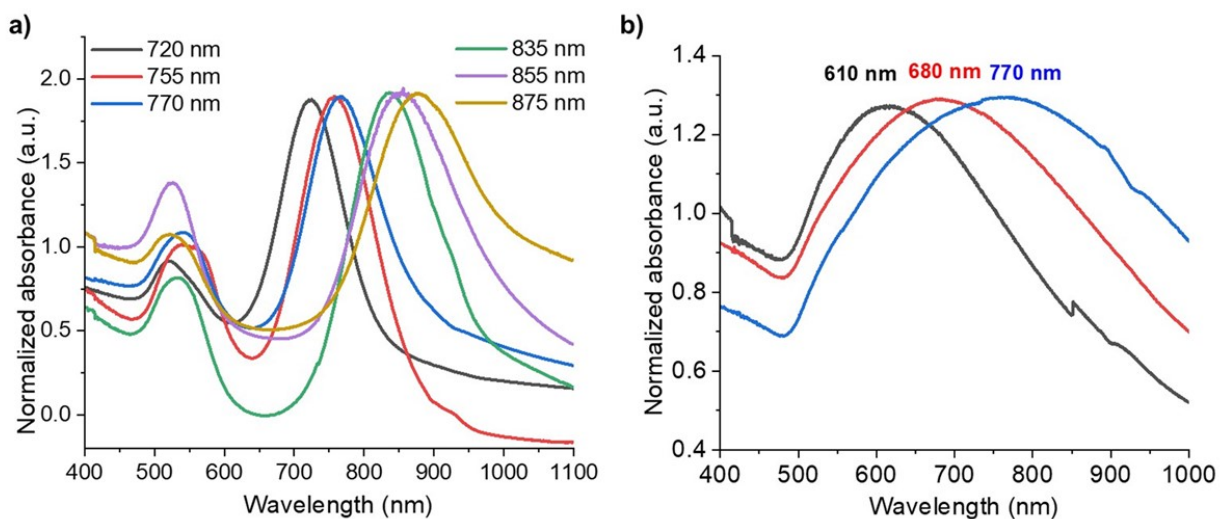
Figure 21. UV-vis absorption spectra of synthesized nanostructures. a) UV-Vis absorption measurements of Au NRs and b) Au NFs.

3.2.2 Towards LSPR-based sensing measurement

To demonstrate the LSPR-based glucose sensing behaviors of Au NRs and Au NFs, we first functionalized the Au nanostructures with suitable linker molecules including 4-MBA, 4- MBPA, DT, MH/DT, and 4-MCP. These molecules form thiol bonds with Au surface and enable hydrogen bonding (excluding DT) to the glucose molecules. We prepared 1 mM solutions of these functional molecules in 1:1 water:ethanol solvent. Then, we mixed an equal volume of Au nanostructure stock solution and functional molecules solution, (1 mL of each) and kept it overnight for the functionalization of Au nanostructures. The binding of these functional molecules altered the plasmonic resonance peaks of Au NRs and NFs due to the change in dielectric environment of NRs and NFs. We then mixed the glucose solution of various concentrations with the functionalized stock solution of Au NRs and NFs at equal volume (100 uL of each) and incubated for around 1 hr. In this report, we included the Au NRs-based glucose sensing with using the functional molecules 4-MBA, 4-MPBA and DT. **Figure 22** illustrates the UV-vis extinction spectra of Au NRs with varying functional molecule types and glucose concentration of 1 mM, 5 mM and 10 mM. The glucose sensing range of colloidal Au NRs in 1 mM to 10 mM indicates the potential of this technique for physiologically relevant glucose concentration measurement.
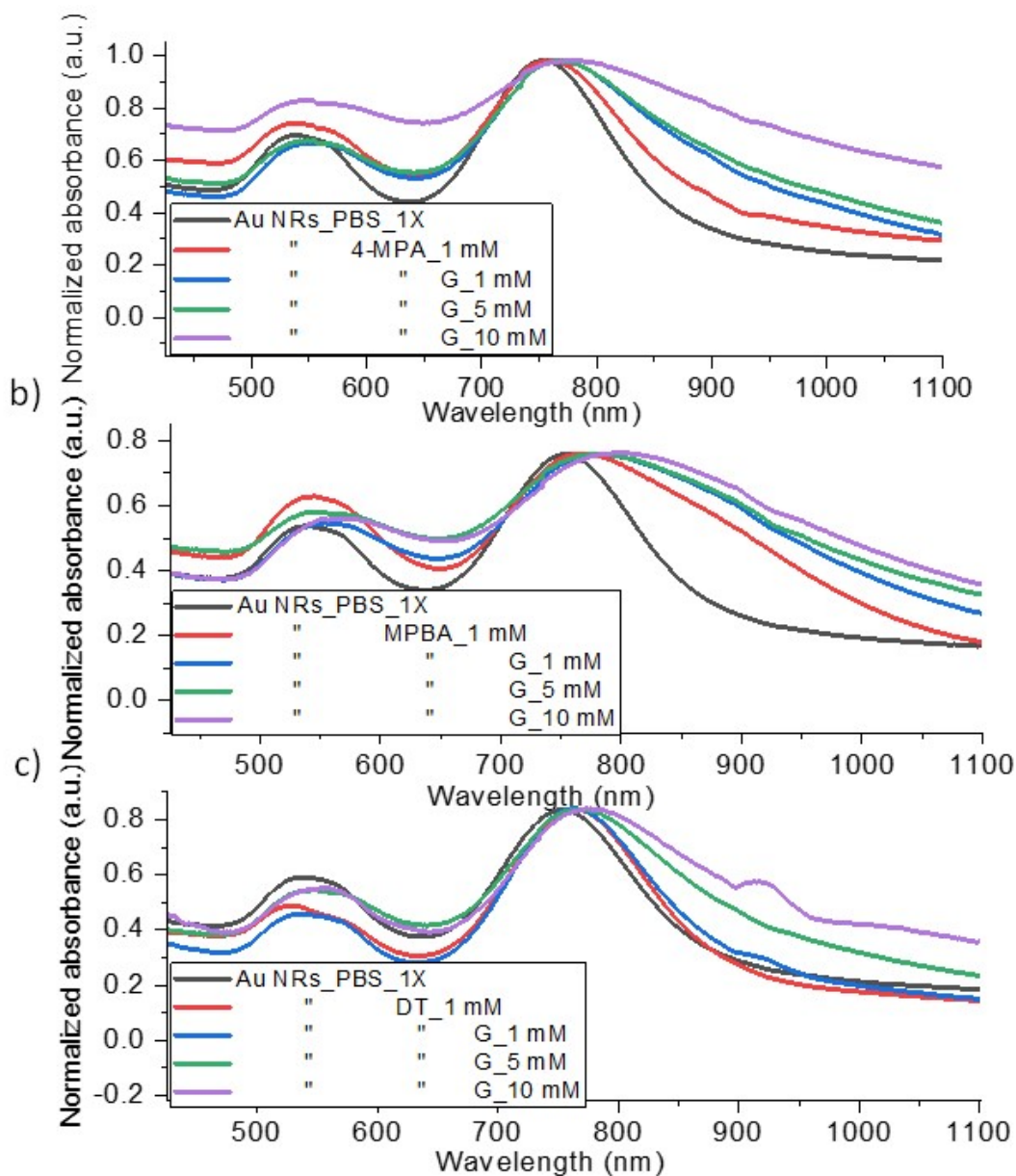
Figure 22. LSPR-based glucose sensing measurement. UV-vis absorption spectra of Au NRs functionalized with i) 4-MBA, ii) 4-MPBA and iii) DT; and glucose concentration is in the range of 1 mM, 5 mM and 10 mM.

3.2.3 Design and fabrication of the SERS sensors in the comparative study

To fabricate SERS based sensors, Si chips were chosen as a substrate. Those chips were first treated with oxygen plasma for 30 sec to make the surface hydrophilic, which makes the silicon surface much more suitable for the deposition of Au nanostructures. Afterwords, those treated chips were incubated in 1 mL solution of Au nanostructures stock (60 uL) and 10 mM linker molecules solution (940 uL)

in 1:1 water:ethanol co-solvent) for 24 hours in the dark environment.

After incubation, Si-chips were rinsed with ethanol and dried with nitrogen. We followed this method to prepare a few varieties of samples with varying nano structural types and linker molecules. This report presents the comparison of SERS signals 4-MBA, 4-MPBA, and 4-MCP on Au NRs and Au NFs (**Figure 23**). We observed some distinct Raman peaks of chosen molecules from flower like structure while comparing them to rod-like structures. The possibility of formation of numerous hot spots from petal-like portions of Au NFs could be the reason for the formation of new peaks. However, a detailed understanding of these phenomenon and testing of additional Raman-active linker molecules would be beneficial.
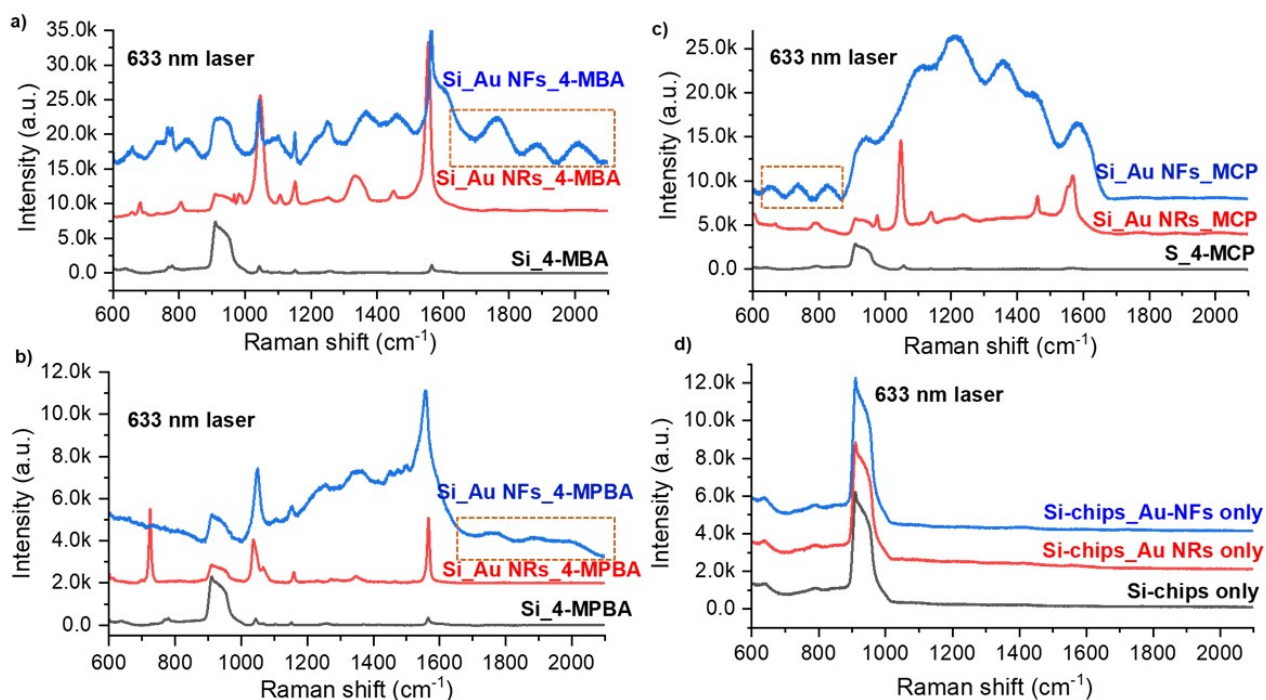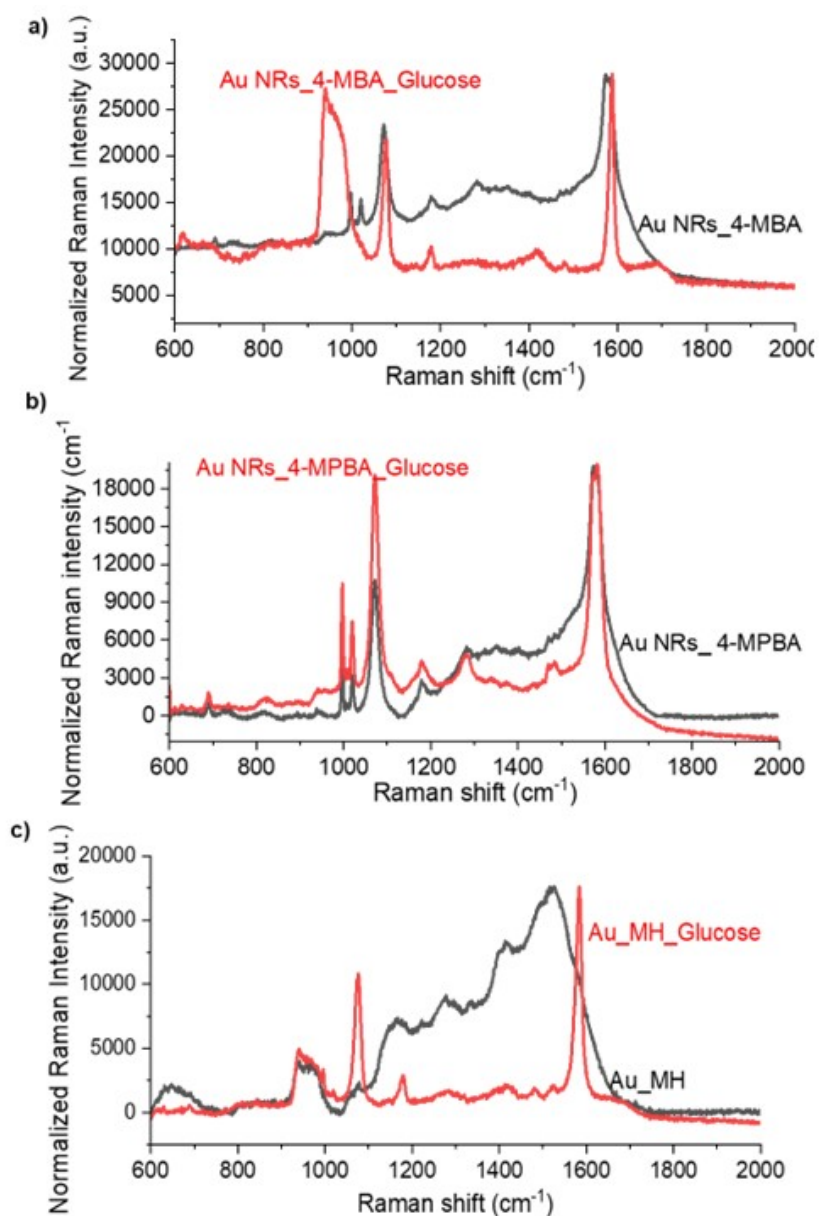

Figure. 23. Comparison of SERS spectra of various functional molecules generated with using Au NRs and Au NFs. SERS spectra with using Au NRs (red curve), Au NFs (blue curve) and without any nanostructures (black curve) generated from 10 mM of a) 4-MBA, b) 4-MPBA and c) 4-MCP. (d) Reference Raman spectra of Si chips (black curve), and Au NRs only (red curve) and Au NFs (blue curve) without functionalization with 4-MBA, 4-MPBA and 4-MCP. All these data were acquired using 633 nm laser excitation, and the same acquisition time.

3.2.4 Towards glucose sensing

To evaluate the performance of these nanostructures functionalized with various ligands, we incubated the nanostructures on Si-chips in glucose solution for 1 hr. Next, we rinsed the chips with ethanol and dried, and tested the glucose sensing capability of our synthesized nanostructures. At this stage, this report presents the SERS data originated from Au NRs functionalized with 10 mM 4-MBA, 4-MPBA and MH following by incubation in 1 mL of 10 mM glucose solution

prepared in 1X PBS as shown in **Figure 24**. To check the distinct SERS behavior of functionalized Au NRs after glucose binding, we normalized the intensity of Raman peak at around 1600 cm^{-1} position, then the data showed the significant increase of relative intensity of short wave numbered peaks after binding with 10 mM glucose concentration. This preliminary result suggests the potential utility of these nanostructures for sensing glucose. Comparing glucose concentration from 1 mM to 10 mM, in the range of diabetic diagnosis based on the SERS signals from Au NRs and Au NFs with using various functional molecules is under plan. Moreover, we need to optimize the sample incubation time for glucose too, and a theoretical simulated study would provide valuable additional insight.

Figure. 24 Comparison of SERS spectra of 10 mM glucose with using various functional

molecules functionalized Au NRs. a) SERS spectra from 4-MBA (black) and 4-MBA_glucose (red). b) SERS spectra from 4-MPBA (black) and 4-MPBA_glucose (red). c) SERS spectra from MH (black) and MH_glucose (red). Glucose incubation was carried out for 1 hr and measurement was proceeded on dried sample. Laser excitation 633 nm, and the same acquisition time.

3.3 SERS measurements from microneedle-based sensors

3.3.1 Soft hydrogel-based SERS biosensors

Prior to developing the microneedle arrays described above in Section 1.2, we tested hydrogel-based microneedles. Hydrogel-based microneedles have mostly been used as drug delivery devices due to their biodegradation and tendency to swell in water. Our motivation for using the hydrogels in microneedles form relies on their capacity to extract interstitial fluid by diffusion through pores, thusenabling in situ biosensing once the SERS active component is incorporated.

We first tested the feasibility of using polyacrylamide (PAM) as a scaffold for plasmonic patches. AuNRs were incorporated in PAM prior to polymerization. The successful embedding of AuNRs in PAM was qualitatively confirmed by dark-field scattering as shown on the image in **Figure 25A** wherethe metal nanoparticle aggregates appear white. Then, the SERS activity of AuNRs in the hydrogel was confirmed using a model water-soluble molecule, 4-mercaptobenzoic acid (4-MBA). As shown in **Figure 25B**, SERS of 4-MBA is only observed when AuNRs are incorporated into the hydrogel. This result confirmed that 4-MBA diffuses through the hydrogel pores and adsorbs to AuNRs embedded in the hydrogel, which is already formed before exposure to 4-MBA.
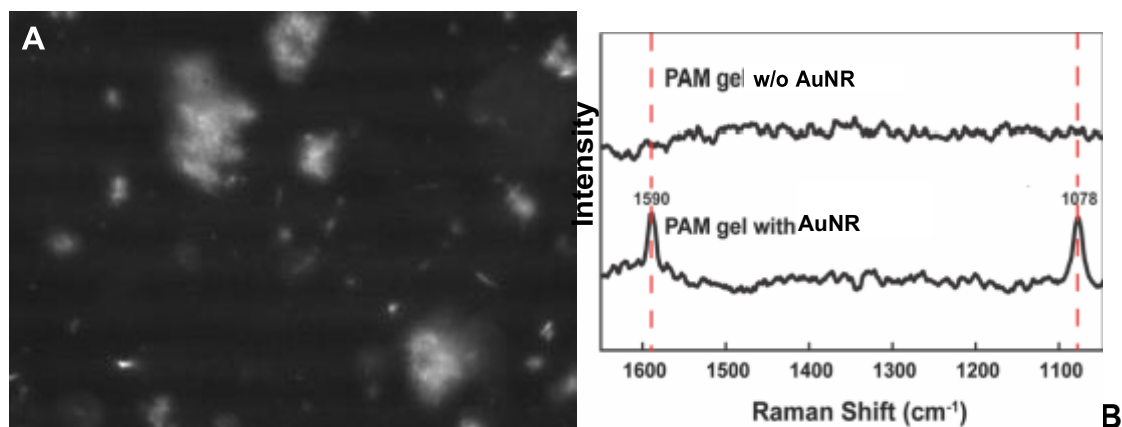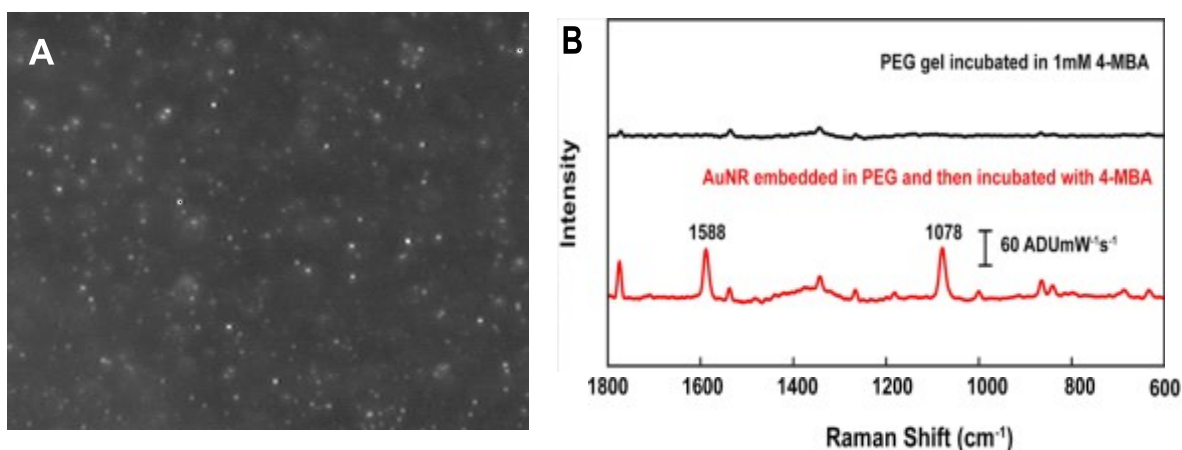

Figure 25. SERS-active hydrogel made with PAM. A) Dark-field scattering image of PEG hydrogel with AuNRs B) SERS spectra of PEG hydrogel with and without AuNRs with 4-MBA (Average of seven spectra using 20x ELWD objective, P_{ex} = 500 µW, λ_{ex} = 785 nm, Savitsky-Golay filtering and baseline correction).

PAM was a useful polymer for us to start with to confirm analyte detection with the AuNRs embedded within the hydrogel. However, the limited stiffness (maximum 1 MPa)[15] of PAM makes

it unsuitablefor the fabrication of microneedles capable of piercing human skin. For an actual sensor, the microneedle design must use a hydrogel with high (~ GPa range) stiffness.

Based on literature results showing that microneedles made with poly(ethylene glycol) (PEG) effectively pierced mouse skin ex vivo,[16] we next selected PEG as our polymer of choice for stiff, transparent, and biocompatible microneedle transdermal patches. Similar to the PAM hydrogel preparation, AuNRs were added to the polymer precursors and then photopolymerized to produce PEG hydrogels loaded with AuNRs. Again, AuNRs were successfully embedded in PEG hydrogels as seen by dark-field scattering (**Figure 26A**). SERS activity of the plasmonic PEG hydrogels was confirmed after incubation in 1 mM 4-MBA and compared against a control sample (PEG hydrogel only, without AuNRs, and incubated in 4-MBA) (**Figure 26B**, black spectrum). Only the hydrogel with AuNRs (**Figure 26B**, red spectrum) showed the two dominant vibrational modes of 4-MBA. Thisresult shows that 4-MBA can diffuse through the PEG hydrogel and adsorb onto AuNRs. This early work showed that AuNRs were successfully integrated into a SERS-active PEG hydrogel.

Figure 26. SERS-active hydrogel made with PEG. A) Dark-field scattering image of a PEG hydrogel with AuNRs B) SERS spectrum PEG hydrogel: black) without AuNRs incubated in 1 mM 4-MBA, red) with AuNRs embedded in hydrogel initially and incubated in 1mM 4-MBA (Average of seven spectra using a 20x ELWD objective, $P_{ex} = 620$ µW, $\lambda_{ex} = 785$ nm, Savitsky-Golay filtering and baseline correction).

3.3.2 Plasmonic NOA microneedle arrays

Plasmonic polymers consisting of AuNRs in NOA microneedles or flat films were incubated in a concentrated solution capture ligand. The CTAB bilayer on the nanorods was replaced with the capture ligand and immobilization through S-Au binding. NOA samples are then immersed in a buffer solution to saturate the surface with the working buffer condition. Varied concentrations of glucose were used to study the glucose sensing capability of the capture ligand. After incubating the microneedle samples in the glucose solution, SERS spectra were collected.

NOA microneedles metallized with Au films were incubated in a concentrated solution of glucose capture ligand 4-MPBA so that the SERS substrate surface was decorated with 4-MPBA. 4-MPBA was used to detect glucose since it is the simplest phenylboronic glucose capture ligand that is

known to bind glucose. With a thiol group present in the molecule, 4-MPBA readily forms self-assembled monolayers on the SERS-active metal surface.

As shown in **Figure 27**, SERS spectra were obtained from NOA microneedles with three different thicknesses of Au (40, 70, and 100 nm). SERS spectrum of bare NOA microneedles (no Au film) was taken to evaluate potential background signals of NOA that may overlap with the SERS signals from 4-MPBA. No NOA SERS signals were found to potentially interfere with SERS signals of 4-MPBA. With the highest SERS intensity of 4-MPBA and highest degree of optical transparency, NOA microneedles with a 40 nm-thick Au film were found to be best among the three thicknesses for detecting glucose.
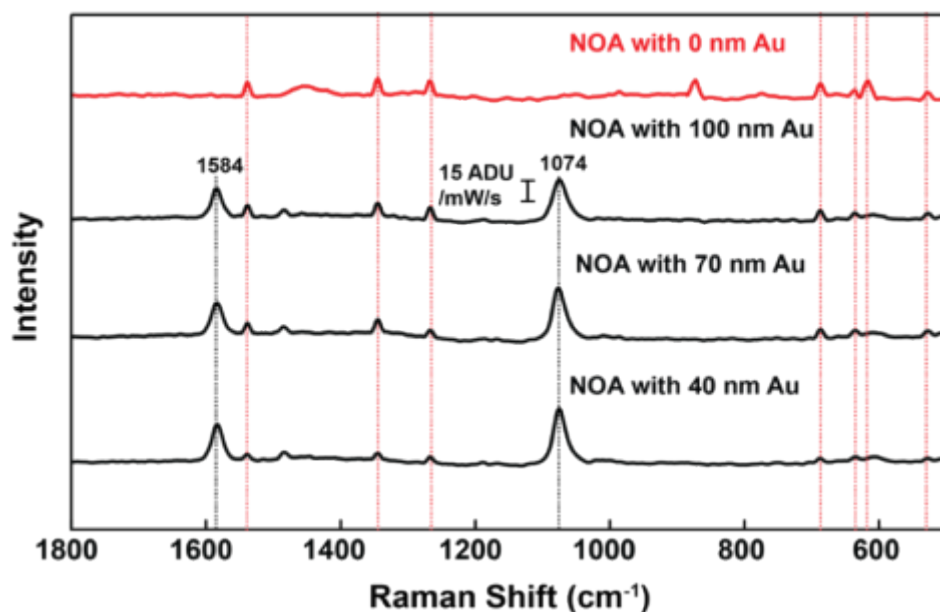

Figure 27. SERS activity of metallized microneedles array. SERS spectra of NOA microneedles with different thicknesses of Au (0, 40, 70, 100 nm) (20x ELWD objective, λ_{ex}= 785 nm, P_{ex}= 278 μW, Savitsky-Golay filtering and baseline correction).

The pKa value of 4-MPBA is around 9 and the ideal pH to detect glucose should be basic condition (pH 9 or higher). SERS spectra were taken with the microneedles incubated in pH 10 buffer and then in 10 mM glucose solution (pH 10). The resulting SERS spectra (**Figure 28**) shows that the dominant peaks of 4-MPBA at 1074 and 1584 cm^{-1} did not shift upon glucose addition, but the peak intensities of both peaks increased when glucose was added. This is consistent with literature results in which only the SERS signal intensities changed upon glucose binding to 4-MPBA.[17,18]

this was a promising result in that these SERS-active NOA microneedles show potential as transdermal glucose nanosensors.
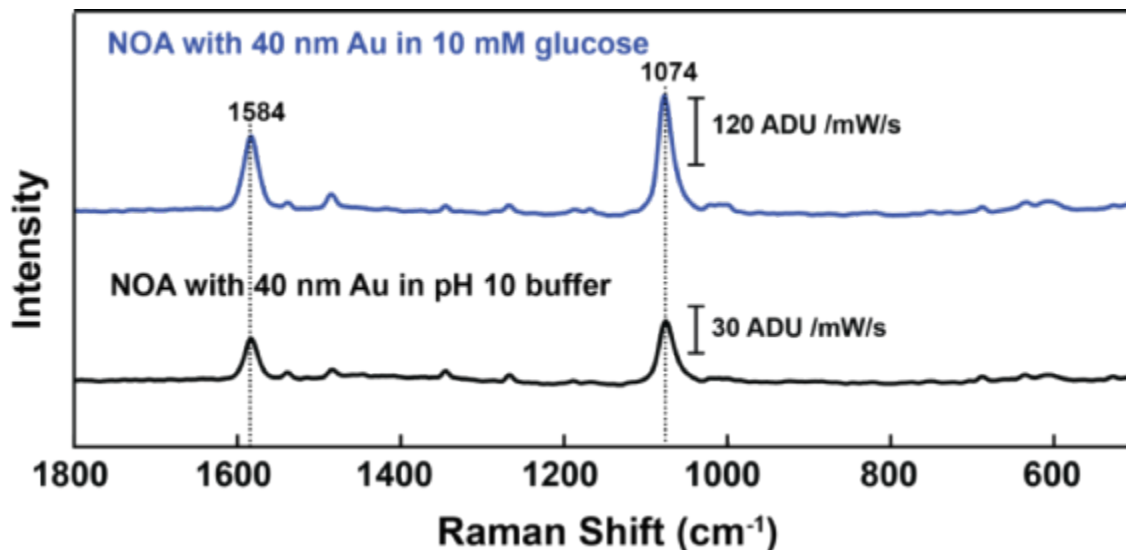
Figure 28. SERS activity of plasmonic microneedles array. SERS spectra of NOA microneedles with and without 10 mM glucose in pH 10 buffer (20x ELWD objective, λ_{ex} =785 nm, P_{ex}= 278 µW, Savitsky-Golay filtering and baseline correction).
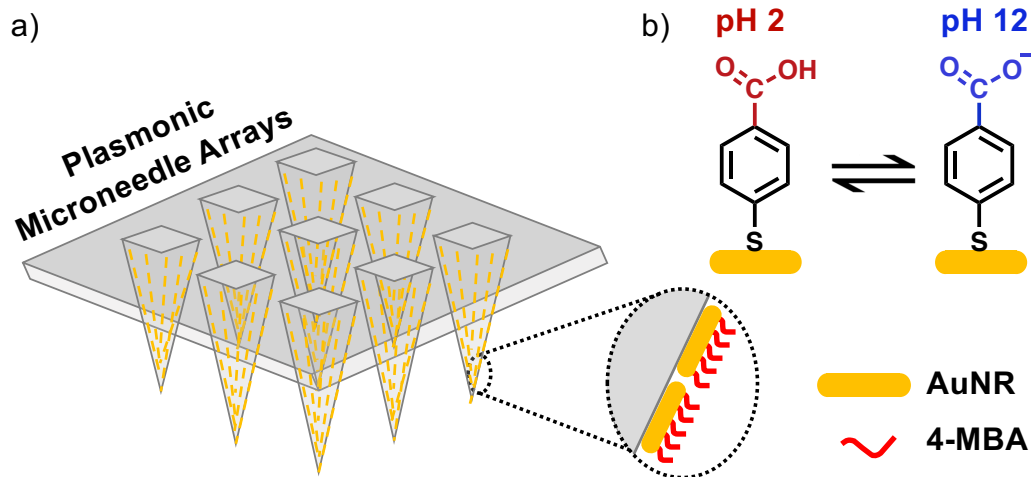
3.3.2.1 Plasmonic microneedle arrays for transdermal SERS sensor platform

Combining the sensing capability of SERS with microneedle arrays creates an opportunity to detect biomolecules *in situ* through tissue or skin that are otherwise difficult to detect in a relatively non-invasive fashion. Microneedle arrays have received attention as a painless and minimally-invasive sensor platform for monitoring analytes in biofluids, especially in the interstitial fluid (ISF). Here, we integrated SERS with polymeric microneedle arrays as a minimally invasive, innovative platform for biomolecule sensing, with particular vision towards detecting glucose in the ISF.

For the polymer, we chose commercially available Norland Optical Adhesive (NOA) 65 that is known to be optically transparent at 785 nm, which is critical since it allows Raman scattered light to be detected through the microneedle arrays and thus enables *in situ* sensing. Although the exact composition of NOA 65 is protected by a commercial patent, the polymer consists of mercaptoester functional groups. We hypothesized that the functional group would allow us to functionalize SERS-active nanoparticles such as AuNRs onto the polymer surface. Lastly, the biocompatibility of various NOAs have been demonstrated in literature by using NOA as a cell culture scaffold for endothelial cells, fibroblasts, HeLa cells and neurons, and human embryonic stem cells. With NOA 65 prepolymer solution, we fabricated microneedles using a replica molding technique where the polymer was photocured (365 nm) inside a PDMS mold. The microneedle arrays have pyramidal features measuring 300 µm x 200 µm (height x width) with a tip-to-tip spacing of 500 µm .

For plasmonic nanomaterial, gold nanorods (AuNRs) were synthesized in aqueous solution using the silver-assisted seed-mediated growth synthesis method with cetyltrimethylammonium bromide stabilizing surfactant. The localized surface plasmon resonance (LSPR) of AuNRs were optimized for excitation at 785 nm in aqueous media. AuNRs were characterized by UV-visible spectroscopy, transmission electron microscopy (TEM) and scanning electron microscopy (SEM), and inductively coupled plasma optical emission spectrometry (ICP-OES). The AuNR concentation was calculated using the concentration of Au determined from ICP-OES, the dimension of AuNRs determined from TEM, and the density of Au.

Next, to fabricate plasmonic microneedle arrays, the NOA microneedle arrays were plasma treated and incubated in 1 mL solution of AuNRs (40 uL of AuNRs and 10 mM 4-MBA in 1:1 water:ethanol co-solvent) for 24 hours. After incubation, the microneedle arrays surface was rinsed with ethanol and dried with nitrogen. The schematic representation of the plasmonic microneedle arrays is shown in **Figure 29**.

Figure 29. Plasmonic microneedle arrays sensor design. a) Gold nanorods (AuNRs) functionalized with a pH-sensitive molecule 4-mercaptobenzoic acid (4-MBA) are decorated on the surface of NOA microneedle arrays. b) pH-sensitive 4-MBA can be protonated at pH 2 and deprotonated at pH 12.

3.3.2.2 Optical characterization

We characterized the plasmonic microneedle arrays by taking optical and SEM images, and light extinction spectra of the sensor. **Figure 30a and 30b** show the dimension of the pyramidal arrays and **Figure 30c and 30d** show the evidence of AuNRs on the sensor surface. This work, along with research presented in sections below, was published in Nano Letters.[19]
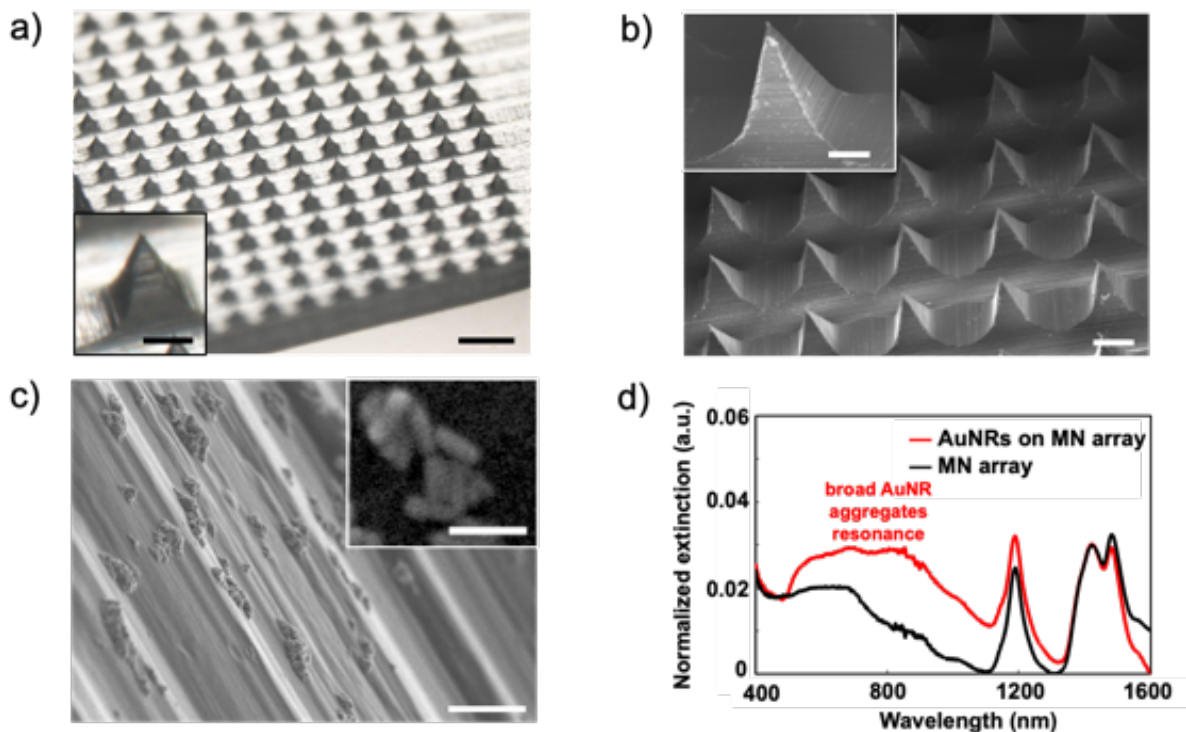
Figure 30. Optical characterization of plasmonic microneedle arrays. a) optical image of the microneedle arrays (scale bars: 500 μm and 100 μm (inset)), b) SEM image of the microneedle arrays (scale bars: 200 μm and 100 μm (inset)), c) SEM image of AuNRs on a microneedle tip (scale bars: 1 μm and 100 nm (inset)), and d) light extinction spectra of microneedle arrays with (red) and without (black) AuNRs.

3.4 Electrochemical (EC)-SERS nanosensors

We investigated alternatives to deal with glucose binding affinity for the sensor. Due to the difficulties of developing a purely chemical capture agent, we started exploring the possibility of using physical strategies as a parallel route to achieve analyte reversible binding onto the SERS hotspots. Encouraged by numerous reports of microneedle-based electrochemical sensors, we decided to include a coated layer of gold onto the MN sensor, consisting of a thin Au layer. This layer is expected to allow application of potential to the surface, permitting modulation of the chemical properties of the sensor. Besides circumventing many of the challenges involved in the incorporation of chemical ligands into the sensor, the set of tools provided by Electrochemistry allows exploration of a new degree of freedom in controlling the sensor response. Indeed, results from our groups indicate the feasibility of using potential to modulate surface chemistry and therefore adsorption.

3.4.1 Microneedles-based EC-SERS sensor

We developed a microneedles-based EC-SERS sensor, recently published in 2022 in Scientific Reports.[20] The sensors were fabricated by placing Norland Optical Adhesive (NOA) prepolymer solution in a PDMS microneedle mold and curing it using UV light as we described previously. We then coated the surface with a 5 nm adhesion layer of titanium using electron beam deposition

followed by a 40 nm layer of gold using thermal deposition. The resulting plasmonic microneedles (Au MNs) are shown in **Figure 31**, which also shows characterization of their Raman enhancement performances. The molding and Au evaporation processes create an intrinsic hierarchical structure with a fine rugosity consisting of ~50 nm characteristic length (**Figures 31D**), which is likely to be responsible for the SERS activity.
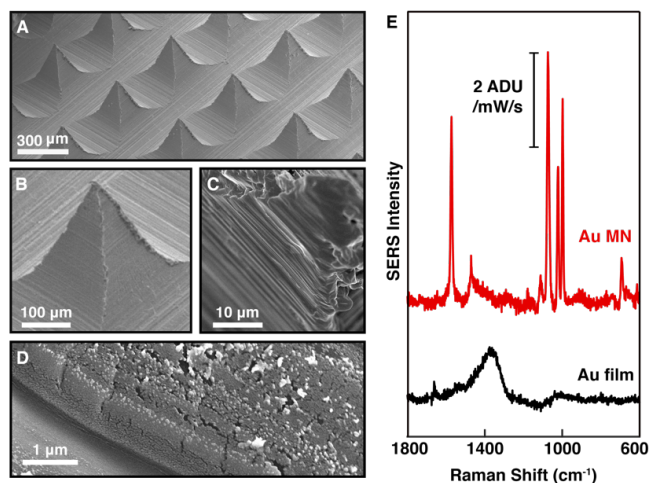
Figure 31. Characterization of Au-coated polymeric microneedles (Au MN). (A-D) Characterization of the surface by scanning electron microscopy, revealing the hierarchical structure which results from the molding and gold evaporation processes. (E) SER spectrum of the Au MN functionalized with benzenethiol, compared to an Au film on a flat NOA. The parameters for the SERS data acquisitions were λ_{ex} = 785 nm, 20x extra-long working distance (ELWD) objective, t_{acq} = 1 min, P_{ex} = 1 mW.

Figure 32 shows a direct comparison between FONs and Au coated microneedles, using benzenethiol (BZT) as a Raman reporter.
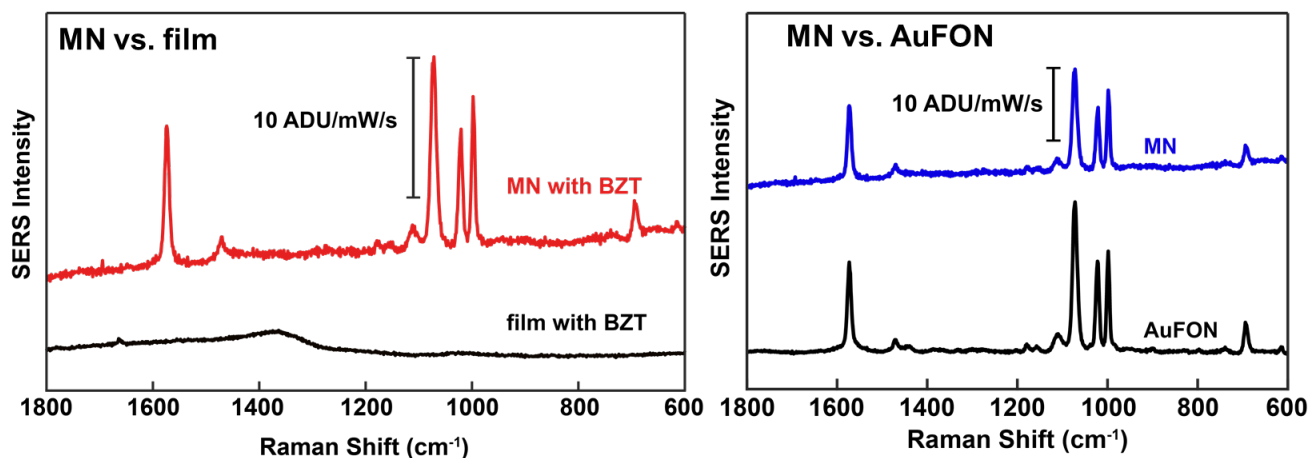

Figure 32. Evaluation of the SERS performance of the EC-SERS-MN (a) the SERS enhancement of Au-MN is compared with a flat film over NOA, using benzenethiol as a Raman reporter (b)

36

Comparison of Au-MN SERS enhancement with a well stablished SERS-substrate (Au-FON), showing comparable performances. For all spectra λ_{ex} = 785 nm, 20x ELWD objective, t_{acq} = 1 min, P_{ex} = 1 mW.

Preliminary tests in ex vivo human skin samples were also conducted and indicate the possibility of applying potential with the sensor in skin. Over the course of these initial tests, we also realized the need to apply a thin adhesion layer (5 nm) of Ti in order to avoid delamination of the gold coating. After we started using a Ti adhesion layer, no evident delamination of the sensor was observed.

Next, we proceeded to analyze the effect of electrochemical potential on the SERS response, using the setup indicated in **Figure 33**. Owing to glucose's low Raman scattering cross-section, we conducted our initial tests in the presence of 1 mM caffeine, a model molecule relevant to biosensing, in the presence of 100 mM phosphate buffer (pH 7.4).
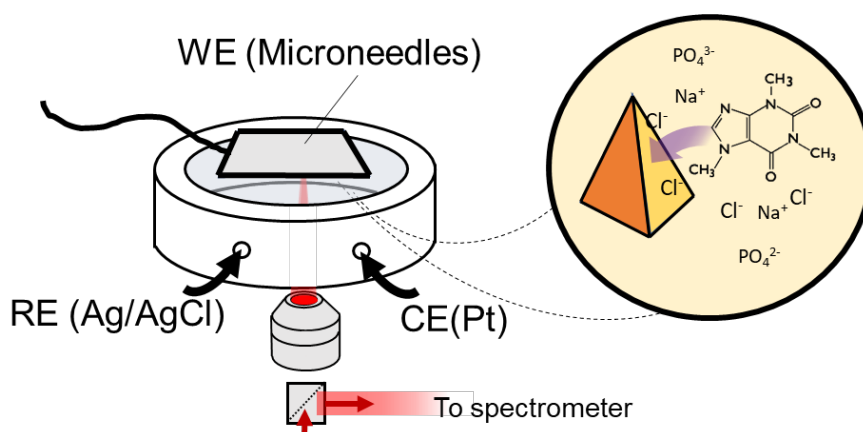
Figure 33. Schematics of the electrochemical SERS setup and experiment concept.

The results, shown in **Figure 34**, indeed indicate that cycling the potential (E) between -0.8 and 1 V (vs Ag/AgCl) generates drastic spectral changes, corresponding to different adsorption and redox events. Initially, at E close to open circuit potential (OCP), only a faint band can be observed, near $250 cm^{-1}$, (black trace in **Figure 34**) which corresponds to electrolyte adsorption on Au surface (Au-Cl) [12]. As the potential is raised, the intensity of this band increases, until E~0.7V where Au oxide forms, which can be observed through the appearance of a broad band at ~550 cm^{-1}, which attenuates all other Raman bands. When the potential is brought to lower potentials, however, caffeine characteristic bands clearly appear, such as the 555 cm^{-1} peak, associated to a perturbated pyrimidine ring breathing mode, and 1325 cm^{-1}, related to imidazole trigonal ring stretching, among others. At more cathodic potentials, these peaks disappear again, only to reappear during the following cycle. A representative cycle is shown in detail on **Figure 34**. This experiment demonstrates the potential of electrochemistry to reversibly modulate surface chemistry, and therefore SERS response of the biosensor.
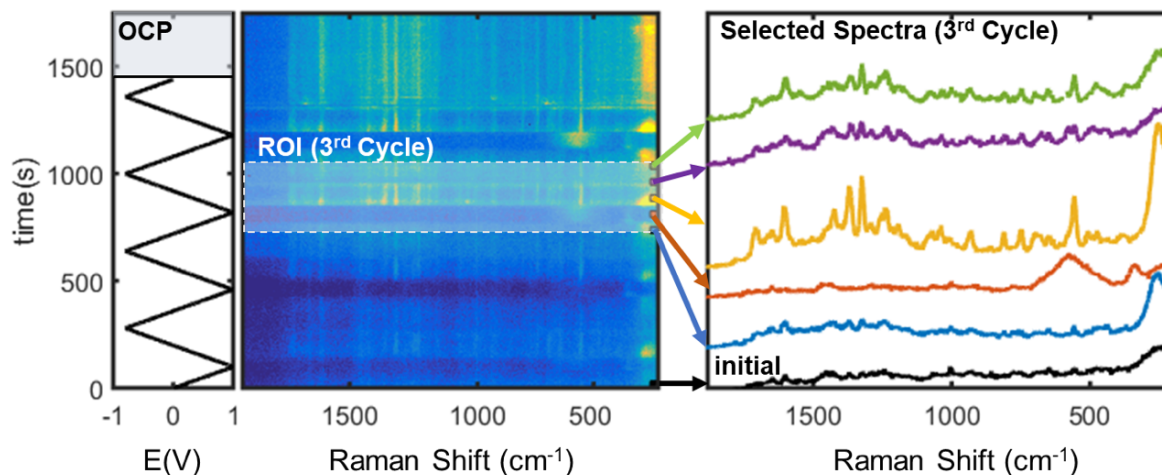
Figure 34. Evaluation of the SERS performance of the EC-SERS-MN. Temporal evolution of the SERS response as a function of potential. Selected spectra are shown (right), corresponding to a representative cycle.

3.4.1.1 Incorporating principal component analysis (PCA)

The ability to modulate adsorption also allowed the application of multivariate methods which are sensitive to the signal variance, such as Principal Component Analysis (PCA). PCA is a popular dimensionality reduction technique which decomposes a set of correlated variables into a lower-dimensional linear representation, preserving the dataset most dominant dynamics. In short, the data is described in terms of the eigenvectors of the dataset correlation matrix. In other words, it discovers new representations of the data by considering a linear combination of variables which maximize the independence of each component (i.e. minimize the redundancy). In the general case the different variables can be very different, making their combination essentially uninterpretable (i.e. comparing apples and oranges). For a spectrum, an ensemble of N different single wavenumber measurements (one for every pixel of the detector), the variables are all comparable, which allows the eigenvectors to be seen as spectra on their own and therefore reasonably interpreted.

These methods traditionally are quite sensitive to sample-to-sample variations, requiring extensive preprocessing of the data in order to extract interpretable physical-chemical information. In our case, however, the data matrix used to extract the spectra representations, is evaluated locally (e.g. at a given spot and sample), which minimizes background influence and other parasitic phenomena. Indeed, the PCA algorithm is applied to data with minimal amounts of preprocessing (only cosmic rays are removed), which makes the methodology more appealing to practical applications and less prone to artifacts due to biased preprocessing.

Next, to demonstrate the ability to detect analytes with EC-SERS microneedles, we tested the devices with caffeine (1 mM), and focused the laser excitation beam (785 nm) on the sample surface. We chose to do initial development with caffeine, rather than glucose, due to glucose's relatively low Raman signal, compared to caffeine. Application of cycles of positive and negative potential resulted

in a repeated signature in the SER spectra with characteristic bands. In order to avoid side reactions and to ensure that only SERS signal was collected, the laser power was limited to 1 mW. Results showed a common pattern through a cycle. Once the potential was lowered to E<0.7 V, the 260 cm-1 band became progressively more visible, in addition to many caffeine characteristic vibration bands, including the 555 cm-1 peak and 1325 cm-1, associated with a perturbated pyrimidine ring breathing mode and imidazole trigonal ring stretching, respectively. At very cathodic potentials (E<-0.4 V), most bands disappeared, and only the background was detected, presumably due to caffeine desorption and formation of a double layer dominated by cations (Na+ and K+), whose adsorption on bare Au show no strong Raman signal. Interestingly, caffeine seems to appear more strongly in the return trace, which might suggest increased affinity for residual oxide that favors adsorption.

Variation of the molecular affinity with surface potential leads to modulation of analyte-dependent peaks through the cycle, which suggests that this dependence could be used to discriminate amongst analytes. This can be done through application of multivariate methods, which are known to efficiently deconvolute the contribution of different analytes in complex samples, such as biological media and mixtures. Among such methods, PCA exploits the correlation between variables to extract lower dimensional representations of the dataset, called the loadings or the eigenvectors. In the case of a spectrum, which can be seen as an ensemble of N single wavenumber measurements, this technique is especially appealing, as the extracted eigenvectors can be plotted against the wavenumber and regarded as spectra on their own, allowing direct interpretation of the results without having to rely on clustering techniques.

Moreover, multivariate methods are often prone to sample-to-sample variations, requiring extensive preprocessing of the data in order to extract useful physical-chemical information. In our experiment, however, the data matrix used to extract the spectra representations is evaluated locally (*e.g.,* at a given spot and sample), which minimizes the influence of background and other confounding factors. Indeed, we successfully applied the PCA algorithm to minimally processed data (only cosmic rays were removed), as shown in **Figure 35**, where the main PCs are portraited (**Figure 35A**) next to the evolution of their time traces (**Figure 35B**). The 4th PC (**Figure 35A**, purple trace) contains caffeine characteristic vibration bands, and its time trace also reproduces our previous observations for caffeine adsorption behavior, being dominant over the other PCs in the return trace of the voltammogram after formation of AuO_x until more cathodic potentials (E<-0.4 V).
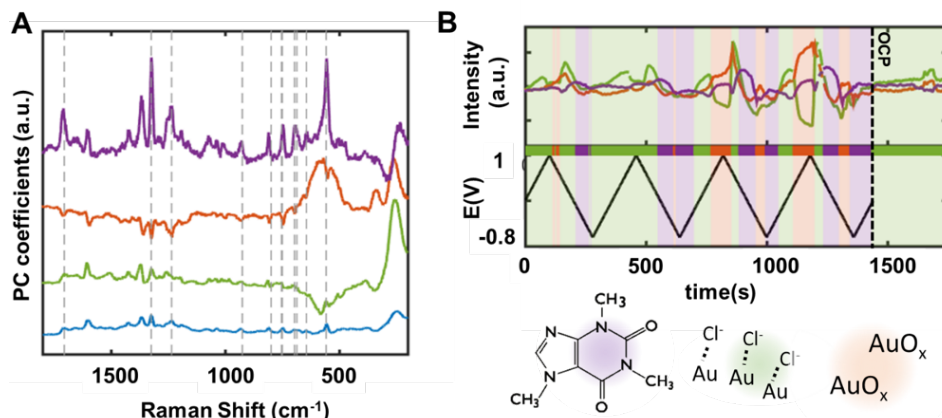
Figure 35. PCA on SERS spectra from caffeine solution. (A) The dominant PCs of the data, which account together for >95% of the dataset dynamics. (B) Dynamics of the 2-4th PCs intensity compared to the potential over time. The shading zones indicate the dominant PC and the dashed lines show known caffeine vibrations33. After the end of the experiment (t ∼1450 s), the system is left at open circuit potential (OCP) for ∼ 150 s.

3.4.1.2 Separating Mixtures using EC-SERS PCA

We also demonstrated that the same strategy can also be used to separate molecules with similar chemical structure (similar to that described in the previous annual report). In order to test that idea, we introduced 1 mM of theobromine in addition to the 1mM caffeine and 100 mM phosphate buffer solution. Theobromine and caffeine have similar chemical structure, only differing by a methyl group, which might suggest similar adsorption behavior. The peaks associated with theobromine and caffeine were isolated into different PCs, demonstrating that even closely related structures can be separated through potential modulation and multivariate analysis (**Figure 36**). These results demonstrate that even molecules with similar chemical structures can display differences in their adsorption potential profiles that are sufficient to enable discrimination between their spectral contribution. This is more directly shown in **Figure 37A**, which shows the evolution of the coefficients of the main PCs with the potential over three potential cycles. Since the first two PCs account for the presence of AuOx, we have cluster them together by summing their scores. The average spectrum of all frames in which this PC becomes dominant is shown in **Figure 37B**, and clearly portrays the characteristic broad band of AuOx. Similarly, averaging the SER spectra on which the 3rd and 4th PCs are dominant reveals the spectra shown in **Figures 37C and 37D**, where the characteristic vibrations from theobromine and caffeine can be respectively identified. Interestingly, we once again observe that caffeine and theobromine characteristic bands only show up on the return trace of the voltammogram, after AuOx is formed and reduced, which suggests the role of trace amounts of oxide in the adsorption of both theobromine and caffeine. This behavior is consistent with our previous experiments.
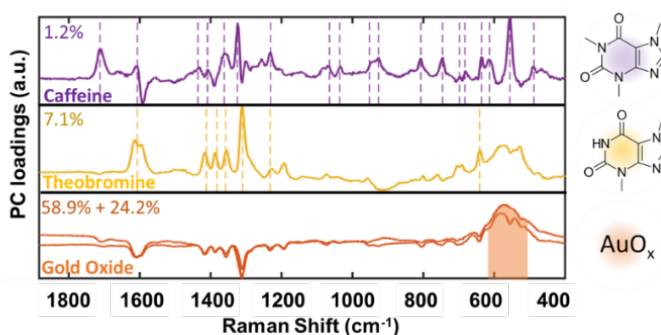
Figure 36. Eigenvectors extracted from a total of 700 spectra (t_{total} = 3500 s) accounting for 91.4% of the dataset dynamics. The presence of caffeine peaks (purple dashed lines) on the 4th PC (purple) can be clearly observed, while the 3rd PC shows theobromine vibration bands (yellow dashed lines), and the 1st /2nd PC (orange) primarily shows AuO$_x$ vibration.
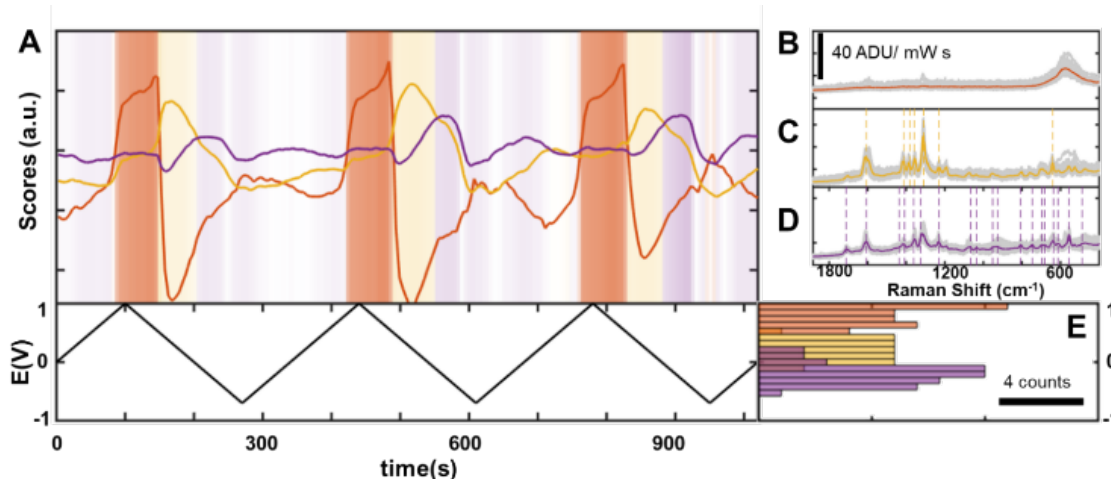
Figure 37. (A) Evolution of the potential and PC scores with time over three potential cycles between -0.8 and 1 V. The intensity of the background colors is proportional to the ratio between the maximal PC intensity (orange for AuOx, yellow for theobromine, and purple for caffeine) and the sum of the other PCs. (B) Spectra in which the AuOx related PCs are dominant (gray) and their average spectrum (orange). (C) Spectra in which the theobromine related PCs are dominant (gray) and their average spectrum (yellow). (D) Spectra in which the caffeine related PCs are dominant (gray) and their average spectrum (purple). (E) Histogram summarizing the potential at which each PC becomes dominant (beyond a 0.1 threshold), clearly showing the dependency of the adsorption probability with the surface potential, and suggesting criteria for selecting one analyte over the others.

Surface potential criteria for selectively localizing each species in the SERS hotspots can be derived by considering the potential at which each PC becomes dominant over the others, as shown in the histograms of **Figure 37E**. One can clearly identify the anodic region where the AuOx (first two PCs) dominates the SERS response, and then the spectral regions where caffeine is more likely to adsorb with respect to theobromine (between 0 and -0.3 V), as summarized in the histogram of **Figure 37E**. This allows potential modulation strategies to be regarded as a pseudo-separative methods, enabling the analysis of complex media in an automated and straight-forward manner. In the context of in vivo biosensors design, our technique can be applied to various conductive plasmonic sensor platforms to enable highly sensitive and selective analysis of chemically complex media, such as biofluids. Thus, we have developed a strategy to directly and continuously detect analytes in a complex mixture using a novel Au MN sensor platform.

### 3.4.2 Fabrication of SERS-active substrates with electrodeposition

Using SERS for glucose detection is challenging due to its low Raman scattering cross-section. In an article published in 2021 in the Journal of Raman Spectroscopy[21], we describe a method for fabricating localized EC-SERS probes on substrate tips using electrodeposition. This method deposits gold with fractal geometries that can be optimized, allowing for enhanced Raman signal quality.

We started by preparing nanoelectrodes based on substrates of 20 nm apex diameter. The pyrolysis of butane generates a thick layer of pyrolytic amorphous carbon on the inner walls of the nanopipette. At ∼200 nm from the apex, the carbon layer completely fills the electrode aperture, forming

nanoelectrodes which are recessed. This electrode geometry is ideal for growing metallic nanostructures by electrodeposition, as the recessed cavity is quickly filled with electrodeposited metal, maximizing the interface between carbon and the electrodeposited material, and therefore the mechanical stability and electronic continuity of the electrodeposited structure.

In order to obtain good surface enhancing properties, some principles regarding the relationship between structure and SERS performance must be considered. In first approximation, the global SERS performance of a plasmonic substrate depends on two main factors: (i) its intrinsic SERS performance, regulated by the plasmonic properties of the material and by the geometry of its hotspots, and (ii) on the density of hotspots. Fast electrodeposition at high overpotentials is expected to generate structures which fulfill these requirements, as it favors nucleation over growth, leading to a corrugated surface with sharp features, nanoscale gaps, and defects, with potential to act as plasmonic hotspots. The inherently self-similar resulting morphology ensures a high density of such hotspots, improving SERS performance.

An example is shown in **Figure 38b**, obtained after cycling a nanoelectrode two times between 0 and −0.9 V at 20 mV/s in a 0.2 mM HAuCl4 and 50 mM KCl solution. Dark-field (DF) spectral characterization of independently grown nanostructures indeed reveals a broad peak extending from 700 nm into the NIR region. This is expected, as the electrodeposited structures are analogous to aggregated particles, for which the plasmon mode is broad and redshifted with respect to the LSPR of well dispersed individual nanoparticles. Based on these measurements, we selected 785 nm as the laser excitation wavelength for SERS experiments. Repetition of the electrodeposition program for a large number (N = 95) of independent nanoelectrodes yields the normalized 2D current-applied potential histogram shown in **Figure 38c**.
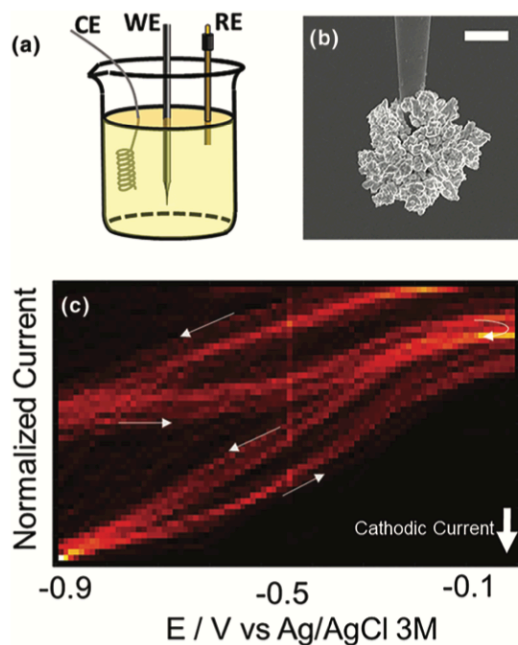

Figure 38. Au SERS substrate electrodeposition. (a) Sketch of the electrodeposition procedure, using Pt wire as the counter electrode and an Ag/AgCl 3 M KCl reference, and (b) characterization by

electronic microscopy of a typical particle resulting from cycling the electrode between 0 and −0.9 V at 20 mV/s over two cycles in 0.2 mM HAuCl4 in 50 mM KCl. The image displays a fractal-like geometry, characteristic of electrodeposition at out-of-equilibrium conditions. The scale bar corresponds to 1 μm. (c) A 2D histogram of the normalized voltammograms obtained by cycling the nanoelectrode two times between 0 and −0.9 V at 20 mV/s. The histogram gathers the data of N = 95 independent electrodepositions and showing the reproducibility of the procedure.

The resulting fractal geometry resulting from the strongly out of equilibrium electrodeposition leads to the appearance of crevices and valleys of different lengths, and consequently of SERS hotspots. The electrodeposition conditions are expected to greatly influence both the density and the intrinsic properties of the hotspots. In this section, we analyze the influence of the scan rate on the SERS performance of nanostructures.

We tested a set of 42 electrodes, divided in two groups: gold was electrodeposited with a scan rate of 20 mV/s or 40 mV/s. As expected, the 40 mV/s group particles spent less time at high overpotential and are consequently smaller than the 20 mV/s group. The size distribution is estimated as d = 2.2 ± 0.3 μm by DF microscopy (N = 15). As both size diameters are larger than the laser spot size (FWHM = 1.4 ± 0.1 μm), it is fair to directly compare the intensity of Raman signal in each particle as a proxy for SERS performance. Benzenethiol was used as the Raman reporter, owing to its large Raman cross-section and its ability to form a self-assembled monolayer on the surface of gold. A 100 mM solution of benzenethiol in ethanol was prepared, and the electrodes were immersed for 1 min, allowing the self-assembled monolayer to form at the gold surface. After functionalization, the electrodes were rinsed with ethanol and SER spectra were collected. An example spectrum is shown in **Figure 39a**.
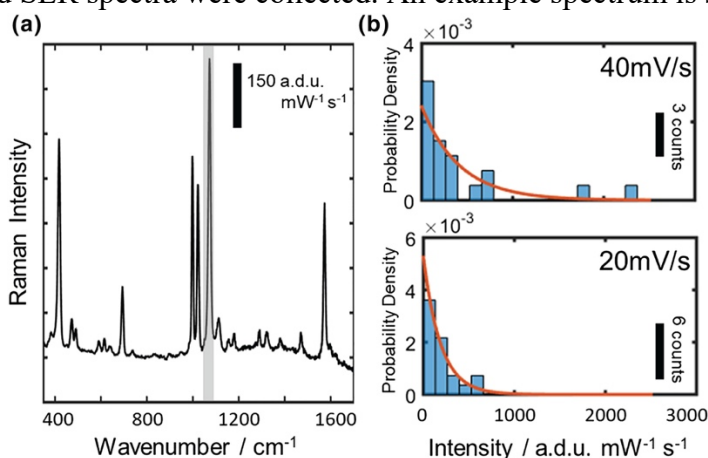

Figure 39. Evaluation of SERS performance of the electro-deposited particles. (a) SER spectra of benzenethiol (BZT), used as a Raman reporter. (b) Histogram of the intensity of the 1,072 cm^{-1} vibration band, used as a proxy for the SERS performance, for particles deposited at 20 mV/s (lower inset, $N = 21$) and 40 mV/s (upper inset, $N = 21$) and their fits by exponential functions (red line).

A value of $\mu20 = 190$ mW s/a.d.u and $\mu40 = 420$ mW s/a.d.u were respectively obtained from the 20 and 40 mV/s datasets. The ratio of the parameters (~ 2.2) reveals that the 40 mV/s electrodeposition procedure consistently produces nanostructures that are more enhancing than those prepared at 20 mV/s. The results suggest that higher scan rates favor SERS performance. We rationalize these

observations on the basis of the fact that although nucleation is relatively an instantaneous process, growth takes time. Slower scan rates therefore allow the freshly nucleated seed to grow more, leading to less sharp surface features and therefore to a poorer SERS performance. Moreover, growth also leads to a lower feature density, therefore creating less numerous hot spots. Higher scan rates are expected to lead to enhanced SERS performance; however, other practical issues start to appear as the particles become progressively smaller than the laser spot size. The measurements are much more prone to sample drift with respect to the laser spot, therefore making a fair comparison more delicate. Similarly, the size can be controlled using different precursor concentrations, which compares particles electrodeposited under the same conditions except the concentration of the gold salt precursor.

Our results show that by controlling the electrodeposition conditions, such as the number of cycles, precursor concentration, and scan rate, it is possible to modulate the particle size and geometry. The conditions can therefore be tuned to a given experimental condition, such as laser spot size, allowing maximization of the SERS signal. Moreover, the SERS performance of electrochemically grown structures is comparable (and can be superior) to more standard SERS platforms such as Au Film over nanosphere (AuFON).

We performed preliminary experiments evaluating the ability to measure glucose with EC-SERS. In these experiments, we detected 1 mM glucose using EC-SERS and Au FONs, as shown in **Figure 40**. The next steps will be to design, build and test the performance of microneedle arrays for detection of glucose with EC-SERS.
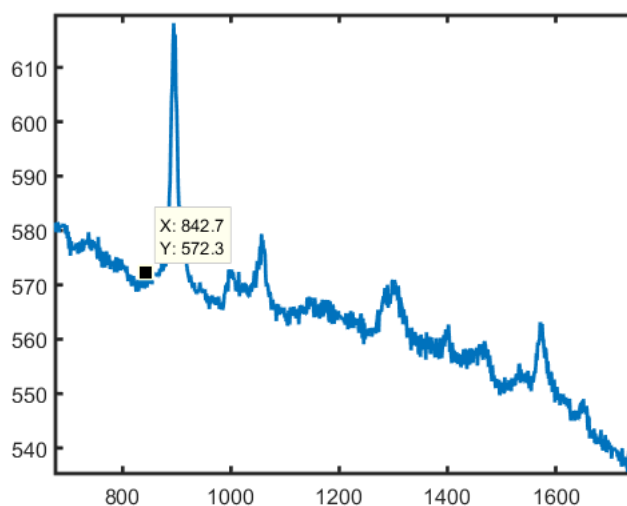

Figure 40. EC-SER spectrum of 1 mM glucose solution.

3.5 Peptide aptamers for binding biomolecules to monolayers on gold

We explored another option for binding biomolecules on gold substrates, as a strategy that could be used in place of the original small molecule ligand approach. In this approach, we immobilized peptide aptamers for the model biomolecule Neuropeptide Y onto alkane-thiolate monolayers on gold surfaces. Three peptide aptamer sequences were evaluated: 1) **"N3"**, a 12-mer peptide that binds NPY

with a Kd of 0.59 μM; 2) "N16", a 12-mer peptide that binds NPY with a Kd of 0.64 μM; and 3) "N21", a 12-mer peptide that does not bind NPY. The sequence GGGC was added to the peptides, where the GGG provided a short spacer and the C provided a sidechain thiol to enable covalent attachment of the peptide aptamer to the monolayer presenting maleimide groups.

To evaluate the ability of the immobilized aptamers to bind and capture NPY, solutions of NPY were applied to the gold substrates presenting the peptide aptamers on monolayers. After a period for binding, the surface was rinsed with water and ethanol, then dried. We used SAMDI-mass spectrometry, a method developed in our group, to analyze whether NPY had bound to the aptamer-presenting surfaces. We observed an equivalent amount of NPY in spectra collected from spots presenting either binding or non-binding peptide when NPY was present at concentrations of 50-100 μM. We did not observe peaks corresponding to NPY at concentrations of 6.25- 25 μM. We tested two additional controls: 1) a random, non-binding peptide sequence, and 2) a surface treated with β-mercaptoethanol (βME). These additional controls represent surfaces that should not specifically bind NPY. This experiment showed equivalent detection of NPY in spectra collected from spots presenting either binding, non-binding or random peptide when NPY was present at concentrations of 50-100 μM (**Figure 41**), but no detection of NPY at concentrations of 6.25-25 μM. The spots in which maleimide sites were blocked by βME, however, gave no detection of NPY at any concentration (**Figure 41**). This result suggests that detection of NPY resulted from a low-affinity, nonspecific interaction with all of the peptides, and that the SAMDI-MS assay did not show any specific, high-affinity binding interactions between NPY and N3 or N16. These results suggest that the use of aptamers immobilized on gold particles will likely be a significant challenge to apply as a method to sense glucose and was not pursued further by our lab.
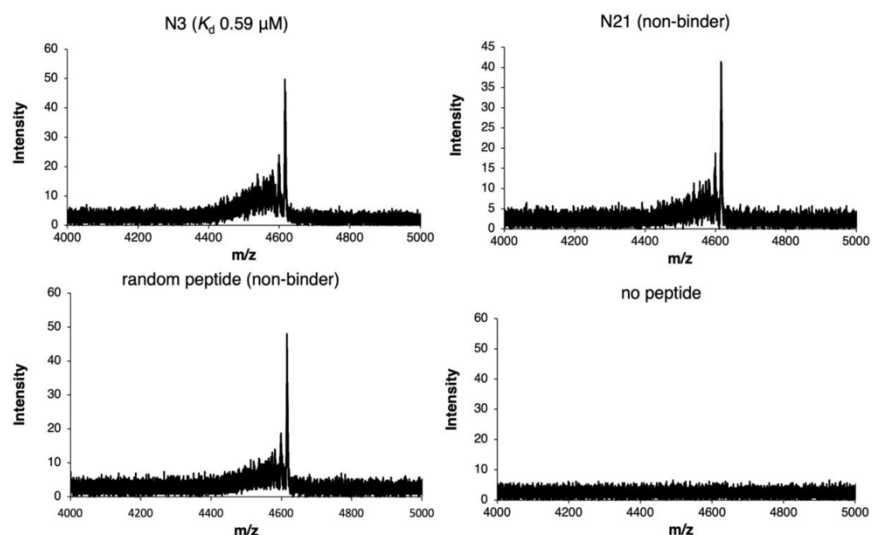
Figure 41. Detection of Neuropeptide Y using peptide aptamers immobilized on monolayers on gold substrates. Representative mass spectra of 100 μM NPY applied to a monolayer saturated with the N3 peptide, the N21 peptide, a random peptide sequence or βME. The peak corresponding to NPY is shown at m/z= 4617.

Major Task 2: Biocompatability of functional nanosensors

4. SYNTHESIS OF ANTI-BIOFOULING LAYERS

We worked extensively on developing SERS-active microneedle arrays for a transdermal sensor for continuous glucose monitoring (CGM). The basic structural parameters that dictate the effectiveness of such a sensor are optical transparency at the wavelength of the SERS excitation in the 700-800 nm region, robust design to effectively penetrate through skin retaining the structural integrity and functionality, both chemically and mechanically stable throughout the sensing time period, and depth of the microneedles in direct contact with the interstitial fluid which will minimize the contamination and biofouling risks of the microneedles from blood-borne proteins. As mentioned above, we chose two different polymeric materials for fabricating microneedles, which are Gantrez-poly(ethylene glycol) (Gantrez-PEG) hydrogels and Norland Optical Adhesive (NOA). Gantrez is a non-toxic material that exhibits antimicrobial properties when mixed with PEG.[3] Donnelly et al. demonstrated the capability of Gantrez-PEG based microneedles for drug delivery and biosensing applications *in vivo*.[5] The selection of this hydrogel material relies on the mechanical robustness to penetrate skin, porosity for diffusion, biocompatibility, and optical characteristics of the solidified hydrogel. In addition to Gantrez-PEG hydrogels, NOA materials are optically transparent which makes them a good candidate for transdermal biosensors. Once photocured, they form mechanically robust structures with high stiffness (~ GPa range).

4.1 Summary of solid microneedles arrays

Solid microneedles arrays were fabricated via a replica molding method using two different classes of polymeric materials: (i) Gantrez-PEG hydrogels and (ii) NOA-based rigid polymers. A plasmonic component (Au nanorods, or AuNRs) was incorporated to make the microneedles SERS active by either embedding the AuNRs in the solid microneedles or through physisorption on the surface of the microneedles, depending on the microneedle material type as well as the fabrication method. For example, AuNRs can only be incorporated into the hydrogel matrix by pre-mixing the AuNRs with the pre-polymer mixture prior to crosslinking. Although the hydrogel swells in water, the mesh size is not large enough and diffusion of the AuNRs into the matrix is severely limited. AuNRs also do not readily localize to the tips of the microneedles where plasmonic enhancing is most relevant. Additionally, NOA pre-polymer mixtures are very viscous liquids that prevent incorporation of AuNRs with a homogeneous dispersion. Therefore, plasmonic particles can only be localized on the NOA surface following the microneedle fabrication. Finally, Raman reporter molecules (glucose capture ligands) are assembled in the self-assembled monolayer (SAM) form on the surface of AuNRs via ligand exchange with the particle stabilizing ligand, cetyltrimethylammonium bromide (CTAB). In the following subsections, we describe the details of how Raman reporter molecules were assembled with the hydrogel and NOA-based solid microneedles, the current challenges for fabrication methods, resulting SERS activities and our proposed solutions to address some of the issues that we encountered.

4.2 Background of Gantrez-PEG hydrogel (anti-biofouling property)

Gantrez is a synthetic, alternating copolymer of maleic anhydride and methyl vinyl ether. Gantrez

and its acidic form have been used in various biomedical applications such as thickening agents in ointments, denture adhesives and drug carriers for oral drug delivery systems.[22,23] Although there is limited information in the literature about extensively studied biocompatibility, there are some research work demonstrating no adverse effects of Gantrez hydrogels using in vitro and in vivo biocompatibility tests.[24,25]

4.3 SERS active solid hydrogel-based microneedles

Solid hydrogel-based microneedles were prepared by casting the aqueous mixture of Gantrez, PEG and AuNRs on a PDMS mold and polymerizing at high temperature (80°C) via esterification of carboxyl and hydroxyl groups in Gantrez and PEG, respectively. Then, the resulting microneedle patch is submerged in a glucose-capture ligand solution to induce the ligand exchange with CTAB and to generate SAMs of Raman reporter molecules on the AuNR surfaces. **Figure 42** demonstrates the SERS activity of plasmonic hydrogel microneedles through detecting Raman fingerprints of commercially available boronic acid-based glucose capture ligand (4-mercaptophenyl boronic acid, 4-MPBA) at 1074 and 1588 cm^{-1} in a pH 10 buffer. The control sample that was swollen in the working buffer condition (pH 10) in the absence of 4-MPBA does not show any Raman fingerprints overlapping with the Raman spectrum of reporter molecule. After glucose was incorporated into the swelling buffer, even at very high concentration (1 M), we could still measure the SERS signals of the reporter molecule, indicating that the reporter molecule is robust enough for this experiment. The purpose of the glucose-capturing Raman reporter is to either bring glucose close enough to the surface of the Raman signal enhancing AuNRs that it can be directly detected (i.e., Raman peaks of glucose would appear), or to indirectly report the presence of glucose through spectral changes (e.g., peak position shifting). Of the two, the former is more difficult to achieve owing to the sharp distance dependence of SERS. However, we see no direct evidence of glucose after 4-MPBA incubation in 1 M glucose, and the characteristic peaks at 1074 and 1588 cm^{-1} maintain their positions upon glucose addition.
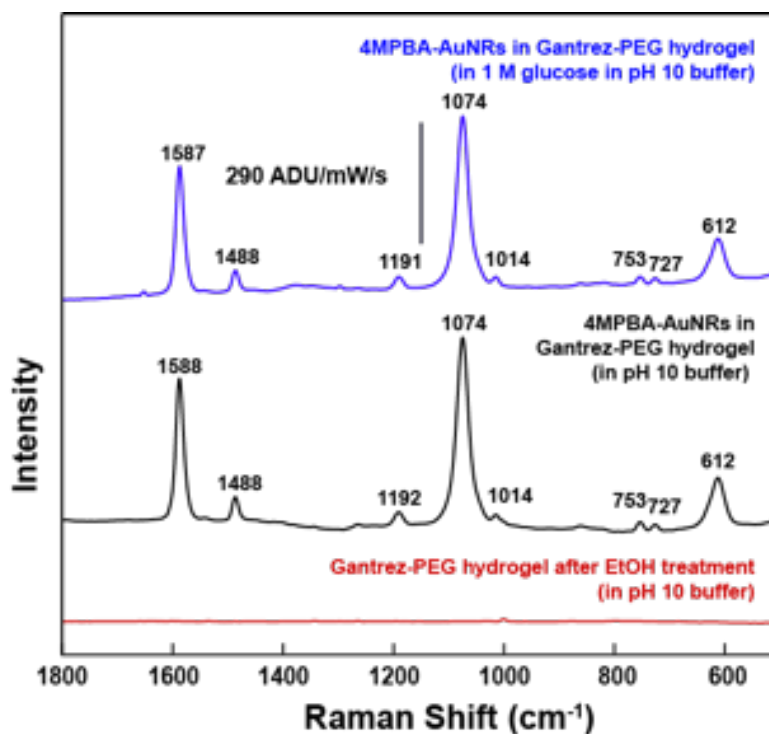
Figure 42. SERS activity of plasmonic-PEG hydrogel. SERS spectra 4-MPBA localized in the flat plasmonic Gantrez-PEG hydrogel before (black) and after (blue) glucose introduction. Control sample does not include AuNRs within the hydrogel matrix (red) (λ_{ex} = 785 nm, 20x ELWD objective, P_{ex} = 278 μW, Savitsky-Golay filtering and baseline correction).

The greatest challenge in preparing plasmonic hydrogel-based microneedles is the capture ligand implementation step where dried hydrogel patch, into which AuNRs are already incorporated, is exposed to capture ligands in organic solvent. Some glucose capture ligands, which show greater promise for glucose detection than 4-MPBA, are only sufficiently soluble for functionalization in organic solvents. In addition to solvent exposure during capture ligand immobilization, plasmonic hydrogel microneedles will be interacting with interstitial fluid upon piercing in skin which is estimated to be a prolonged time period for biosensing and gives enough time to get fully swollen. These two factors – multiple swelling steps with different solvents, and long term swelling in interstitial fluid - brought into question whether the AuNRs will remain intact within the hydrogel matrix. Therefore, it was important to investigate the entrapped AuNR stability within the Gantrez-PEG hydrogel patch under organic and aqueous solvent conditions.

We used the UV-Vis extinction of AuNRs to evaluate the presence of entrapped particles in the hydrogel patch. To test the particles stability, a slab of flat plasmonic hydrogel was incubated in ethanol for 1 hour and then dried. UV-Vis spectra of the dry hydrogel before and after ethanol treatment shows no change in the extinction peaks at 500-600 nm and 800 nm regions (**Figure 43**-blue and orange spectra) that are characteristic longitudinal and transverse surface plasmon extinction peaks for the 50 nm long and 20 nm wide AuNRs that we use. This represents that AuNRs are still in the hydrogel matrix with minimum particle loss via diffusion which is below the optical detection limits. Then, the sample was soaked in DI water for 1 h. This time, the wet

sample's UV-Vis extinction was measured because the longterm goal is to take biosensing measurements through the swollen plasmonic hydrogel microneedles which have pierced skin. We observed a significant decrease in the peak intensities in the UV-Vis spectrum. This may mean either (i) particles already leached out of the hydrogel matrix as the hydrogel swelled or (ii) the density of particles was diminished in a given volume with the geometrical expansion effect of swelling. Once the sample was dried, the extinction peaks were recovered. We have seen a very similar trend in the extinction spectrum upon swelling in a basic buffer condition (pH 10) which is the working buffer condition for glucose capturing with 4-MPBA. Thus, we concluded that AuNRs are physically locked within the Gantrez-PEG hydrogel and remain in the matrix as the hydrogel swells with organic and aqueous solvents.
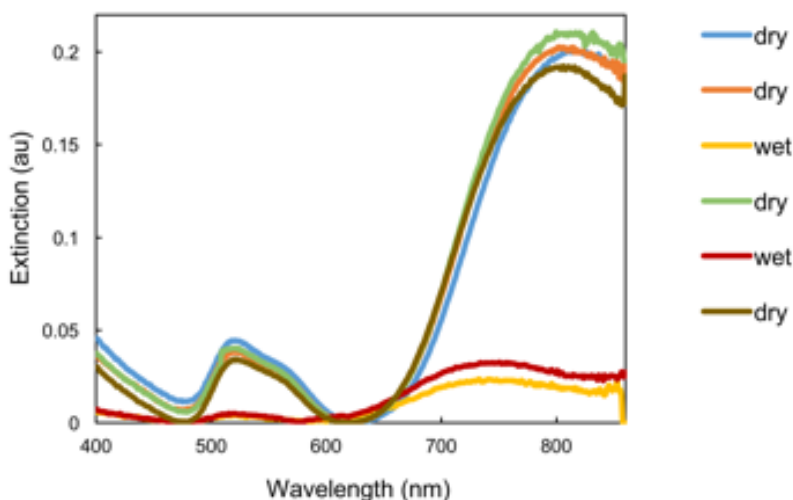

Figure 43. Au NRs stability within plasmonic hydrogel upon solvent (ethanol, DI water, and pH 10 buffer) exposure. UV-Vis spectra of flat plasmonic Gantrez-PEG hydrogel in (dry-blue) dried form right after preparation, (dry-orange) dried form after swelling in ethanol, (wet-yellow) swollen with DI water, (dry-green) dried form after DI exposure, (wet-red) swollen in pH 10 buffer, (dry-brown) and dried after buffer exposure.

Although we observed with UV-Vis measurements that AuNRs are stable in the hydrogel matrix during solvent treatment in a fully soaked condition, we also observed that the patch does not go back to its original flat 3D geometry due to non-uniform shrinkage of two surfaces. We didn't see any change in mechanical robustness for the samples that went through swell-dry cycle as evidenced by initial punching tests using skin mimicking agarose gel phantom. However, hydrogel microneedles with wrinkles may prevent maximum engagement with the skin and this may lead partial penetration of the microneedles that will negatively impact the sensing measurements. One way of resolving this issue would be to functionalize AuNRs with SAMs of Raman reporter molecules prior to particles incorporation into the Gantrez-PEG hydrogel. Thus, the patch will not go through a post-processing with solvent and the structural integrity would be maintained.

5. DEMONSTRATION OF STABILITY OF BIOCOMPATIBLE, ANTI-BIOFOULING COATINGS IN COMPLEX BIOFLUID

5.1 Monitoring stability and SERS activity of plasmonic NOA microneedles in an interstitial fluid-mimicking condition

Similar to evaluating AuNRs stability within plasmonic Gantrez-PEG patch under organic and aqueous solvent conditions, it is crucial to define the particles stability of plasmonic NOA microneedles and corresponding SERS activity in a biofluidic mimic considering the skin pierced patch. The exact composition of interstitial fluid is still a subject of study, but its known components include small and large molecules such as metabolites (glucose, lactate, glutamate), ions (Na^+ and K^+), cytokines, and proteins. Therefore, we used PBS buffer solution as the interstitial fluid mimicking condition to determine the particles stability. The plasmonic NOA patch was incubated in the PBS buffer for an extended time period (one month) and their optical extinctions were used to evaluate the presence of AuNRs assembly on the patch surface (**Figure 44**). The results are promising – we demonstrated particle stability and SERS activity under one month in PBS buffer.
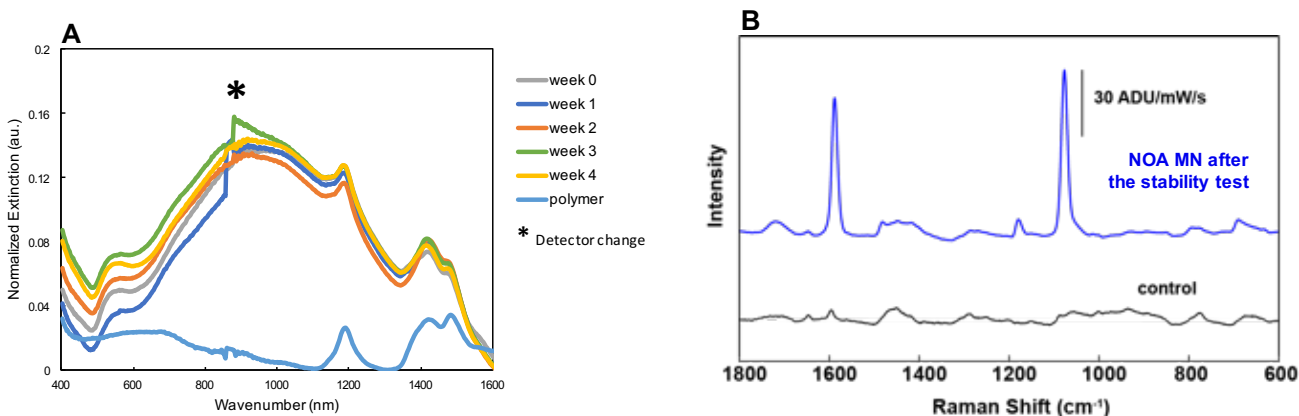
Figure 44. Monitoring Au NRs stability and SERS activity of plasmonic NOA microneedles in interstitial fluidic mimicking condition. (A) UV-Vis spectra of AuNRs and (B) SERS spectra of a Raman reporter (4-mercaptobenzoic acid, 4-MBA) on the plasmonic NOA microneedles surface before and after incubating in PBS buffer for a one month period. Control sample does not include the reporter molecules on the AuNRs surfaces.

5.2 Optimization of NOA microneedles for SERS biosensing and developing a method to localize AuNRs at microneedles tips

AuFONs prepared by the Van Duyne group are very important initial standards for plasmonic (hydrogel or NOA) microneedles to identify the maximum Raman signal intensity of the reporter molecules. Thus, we can adjust the plasmonic microneedles patch formulation in a way that the SERS signal can be maximized for biosensing applications. Previously shown SERS spectra of the reporter molecule demonstrated the dominant Raman fingerprints. However, the Raman signal intensities were not as high as the AuFONs samples. In order to improve the SERS activity of plasmonic NOA microneedles, we prepared the plasmonic patches with different capture ligand density on the particles surface. This could be done by simply working with varied capture ligand concentration ranging from 10 to 100 mM and their extended incubation time (24 h) compared to earlier samples (45 min). We observed enhanced SERS signals for the samples that hold higher ligand density (**Figure 45**).
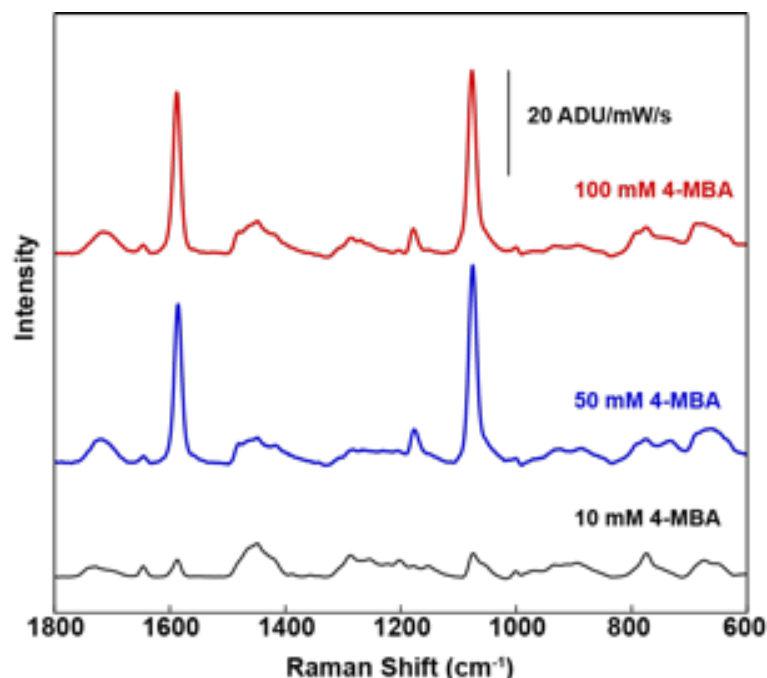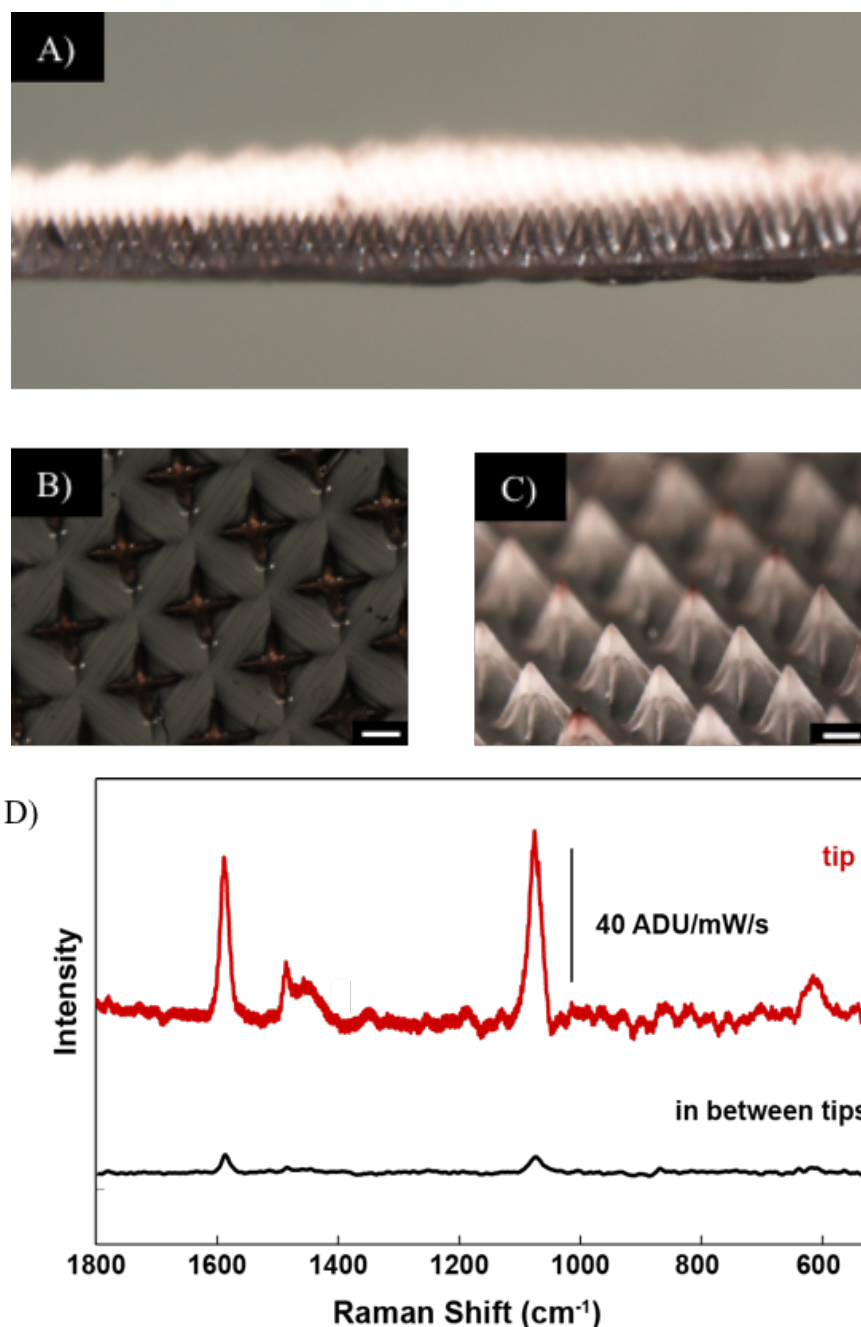
Figure 45. Enhanced SERS activity of plasmonic NOA microneedles by tuning Raman reporter molecule (4-mercaptobenzoic acid) density on AuNRs surface. (20x ELWD objective, λ_{ex} = 785 nm, P_{ex} =1 mW, Savitsky-Golay filtering and baseline correction).

Tip sections of the transdermal plasmonic patches will be interacting with interstitial fluid upon piercing into skin. Once the light source is focused on the plasmonic device, Raman fingerprints of glucose-captured ligands will be collected from a large area across the surface that is limited by the laser spot size. Alternatively, the laser can be scanned across the device surface and the Raman signals of the reporter molecule can be averaged for a given area. In this scenario, capture ligand Raman signals originated from the flat regions between microneedles tips would give background signals of un-bound ligands given the fact that flat regions are not in direct contact with epidermis and interstitial fluid. The best way to differentiate bound *vs* unbound capture ligand signals is to localize plasmonic component selectively at the tips surface and to minimize the particles density on the flat regions. This will allow us to maximize the sensing performance of the plasmonic microneedles. In order to prepare selective particle entrapment only within the hydrogel tip or deposition on the NOA tip surface, we have tried a few different approaches:

### 5.2.1 Au NRs localization at the Gantrez-PEG microneedles tips.

Pre-polymer solution of Gantrez and PEG was mixed with AuNRs following its deposition on the PDMS mold. The excess solution was carefully removed from the mold surface by wiping with a glass slide. The mixture was allowed to dry for a few hours at ambient conditions. Then, the mold was filled with the same hydrogel mixture composition but without AuNRs and polymerized at high temperature. In **Figure 46**, optical images of the resulting sample demonstrate AuNRs that are localized at the microneedles tips. Following the capture ligand immobilization on particles surface, SERS activity was measured as maximized at the hydrogel microneedles tip only (**Figure 46D**).

51

Figure 46. Localized AuNRs at plasmonic-PEG microneedles tips and corresponding SERS activity. Optical images of an array of plasmonic Gantrez-PEG hydrogel microneedles with AuNRs selectively localized at the tips: (A) in large field of view, (B) from top view, and (C) from tilted sample. Scale bars are 200 mm. (D) SERS spectra of 4-MPBA at the plasmonic Gantrez-PEG hydrogel tip (red) and flat regions in between the microneedles (black) (20x ELWD objective, λ_{ex} = 785 nm, P_{ex} = 0.55 μW, Savitsky-Golay filtering and baseline correction).

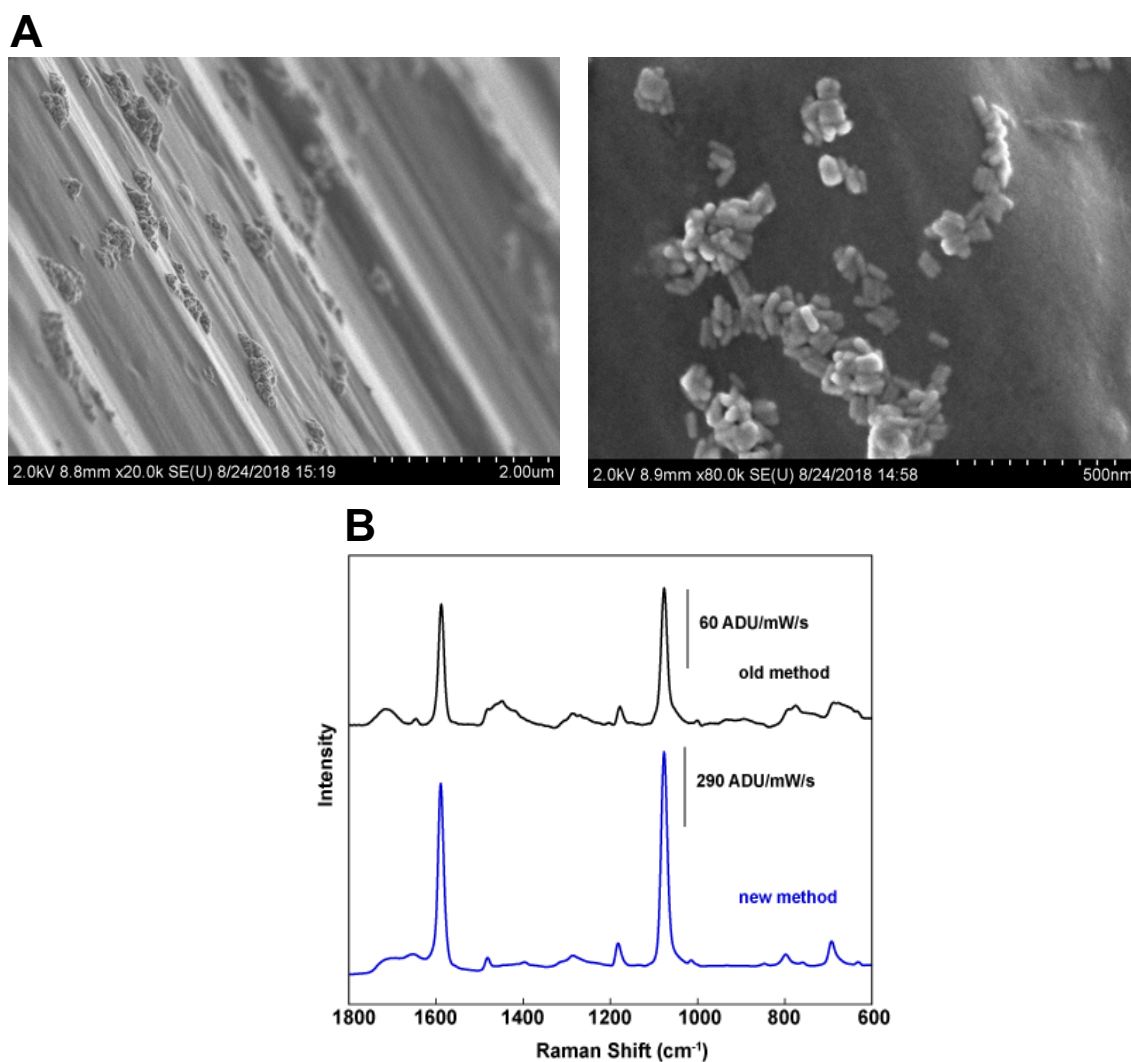## 5.2.2 Au NRs localization at the NOA microneedles tips

A drop of AuNRs solution was deposited on a flat PDMS surface and let dry. Then, particles were transfer printed on the NOA microneedles tip by bringing the PDMS in contact with the microneedles. AuNRs were transferred from the PDMS surface onto the tips (**Figure 47A-B**). Once the patch was incubated in the reporter molecule solution, particles remained intact giving strong SERS signals (**Figure 47C**).
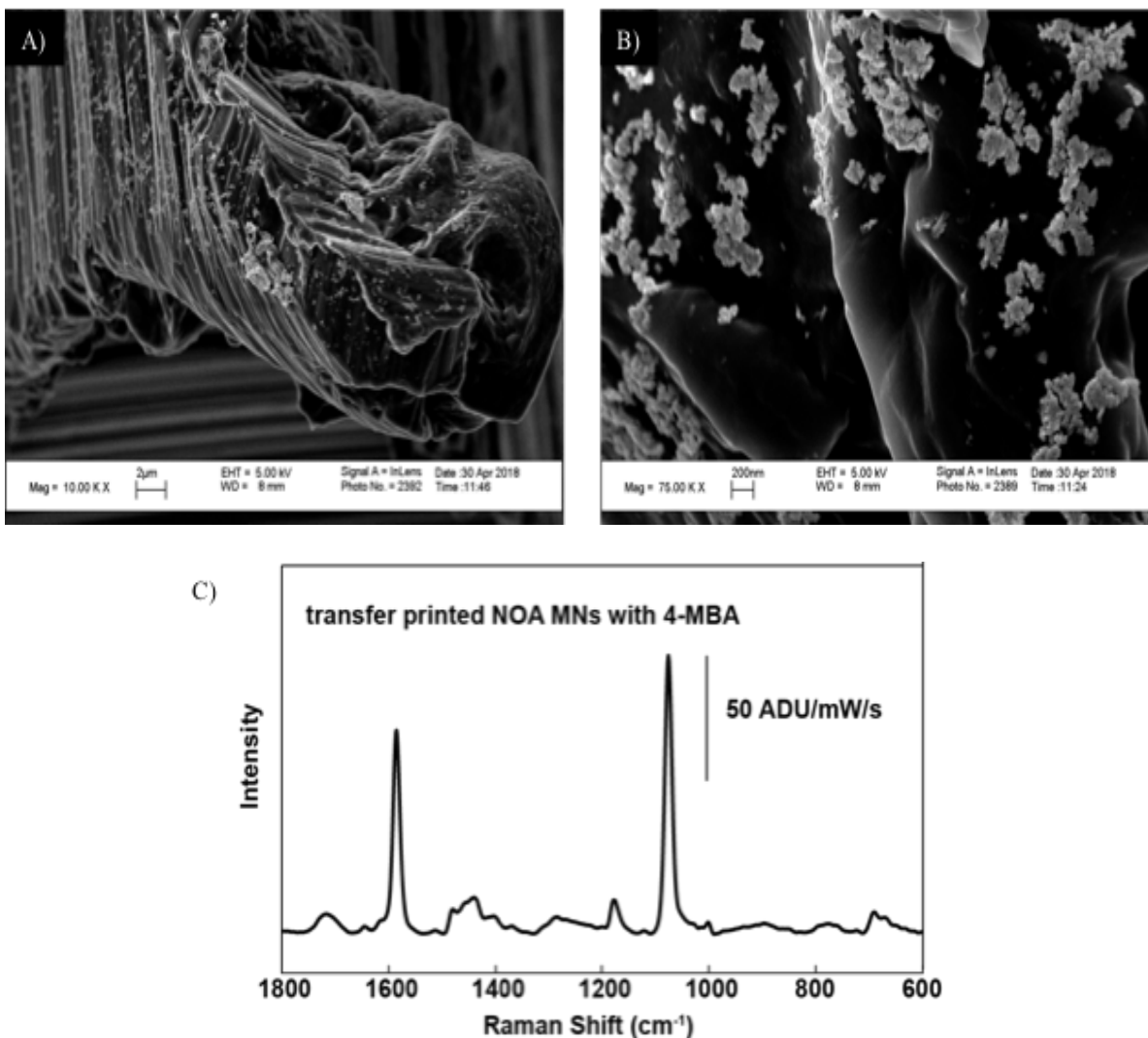
Figure 47. Localized SERS activity on plasmonic NOA microneedles tips. (A, B) SEM micrograph of transfer printed Au NRs assembly localized at NOA microneedles tip. (C) SERS activity of transfer printed samples demonstrating localized SERS signals at the microneedles tips (20x ELWD objective, λ_{ex} = 785 nm, P_{ex} =1 mW, Savitsky-Golay filtering and baseline correction).

We were concerned with the possibility of partial ligand exchange during the ligand immobilization step where AuNRs were already aggregated on the NOA surface and capture ligand molecules may not diffuse in depth of the randomly arranged particles aggregates due to tight particle-particle

contacts. This will strongly reduce the number of SERS active hot spots for the signal enhancement and will lead to reduced signal-to-noise ratio. We came up with an alternative approach to maximize SERS signals. In this approach, AuNRs assembly on the NOA microneedles as well as their functionalization with capture ligand were performed in situ while NOA patch was incubated in the mixture of particles and capture ligand solution (**Figure 48**). Since this is another solution based particle immobilization method, it does not provide selective particle deposition at the microneedles tip.

Figure 48. In Situ AuNRs assembly and their functionalization as localized on the NOA microneedles. (A) SEM micrographs of Au NRs that are functionalized with capture ligand as localized on NOA microneedles surface. (B) SERS spectrum of NOA MN functionalized with 4-MBA using two different methods (old vs. new).

5.3 Demonstration of NOA microneedle stability and functionality

We started with validating the plasmonic NOA microneedles for SERS biosensing. Then, we tested

54

the mechanical and chemical stability by puncturing the microneedles in a skin phantom.

5.3.1 Validating the plasmonic NOA microneedle platform for SERS biosensing

After successfully fabricating NOA microneedles with AuNRs, we functionalized the surface with a pH sensitive molecule, 4-MBA, to validate the NOA microneedle platform for SERS biosensing. After confirming the SERS activity of the platform, we measured SERS of NOA microneedle tips by focusing a laser directly onto the tip (not through the polymer) and then focusing through the polymer in order to check whether the laser interferes with NOA polymer. The resulting SERS spectra in **Figure 49** showed the signal-to-noise ratio of the SERS signals before and after focusing through the polymer were the same, confirming the optical transparency of the polymer and appropriateness of the material for SERS sensing.
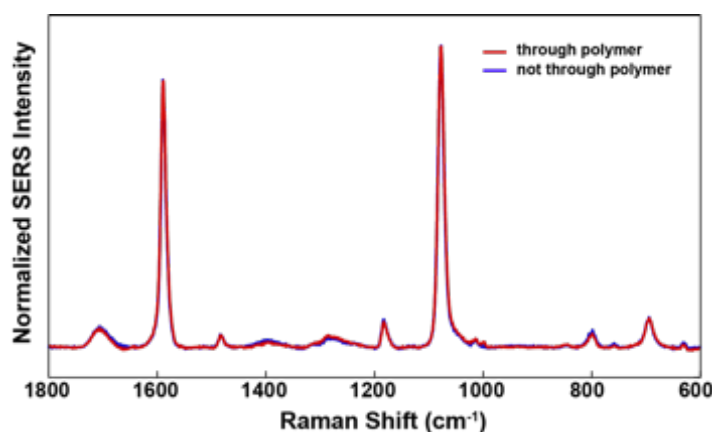

Figure 49. SERS spectra of 4-MBA functionalized on AuNRs of NOA microneedles focused on the tip directly (blue) and through the NOA polymer (red) (Average of seven spectra using 20x ELWD objective, $P_{ex} = 1$ mW, $\lambda_{ex} = 785$ nm, with baseline correction, and normalized to the SERS peak intensity at 1076cm^{-1}).

Mechanical robustness of the sensor was demonstrated by penetrating through an agarose skin phantom and detecting the pH of the gel, and puncturing through the gel multiple time (10 times). First, NOA microneedles was punctured through an agar gel and SERS was measured while the microneedles of the sensor was in the gel. As shown in **Figure 50**, a peak at around 1400 cm^{-1} increased upon inserting the microneedles into the agar gel. Based on the peak intensity at 1400 cm^{-1}, the pH of the agar gel was around 8. Then, the sensor was taken out from the gel and SERS was measured again after rinsing with water. The resulting SERS spectrum before and after penetrating agar gel were the same, showing the reversibility of the sensor. Lastly, SERS of the microneedle sensor was measured before and after puncturing through an agar gel 10 times (**Figure 51B**). The SERS signal intensity did not change upon penetrating the agar gel, demonstrating the mechanical stability of the sensor.
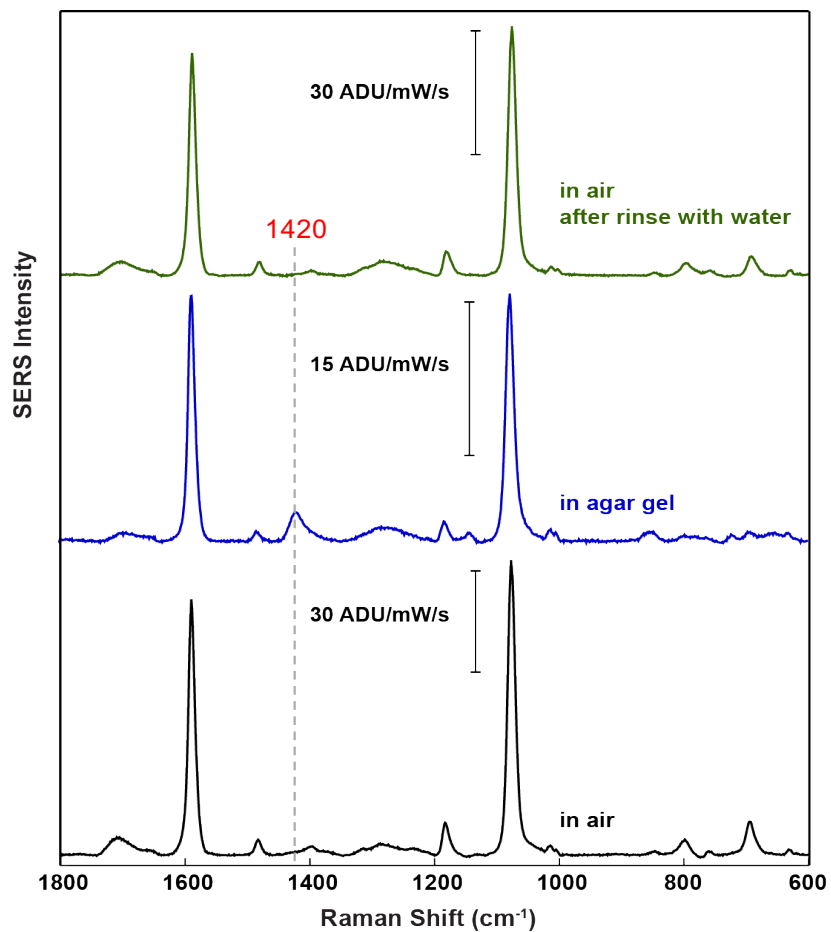
Figure 50. SERS spectra of NOA microneedles functionalized with 4-MBA taken in air (black), agar gel (blue), air after rinsing it with water (green) (Average of seven spectra using 20x ELWD objective, $P_{ex} = 1$ mW, $\lambda_{ex} = 785$ nm, with baseline correction, and normalized to the SERS peak intensity at 1076 cm^{-1}).
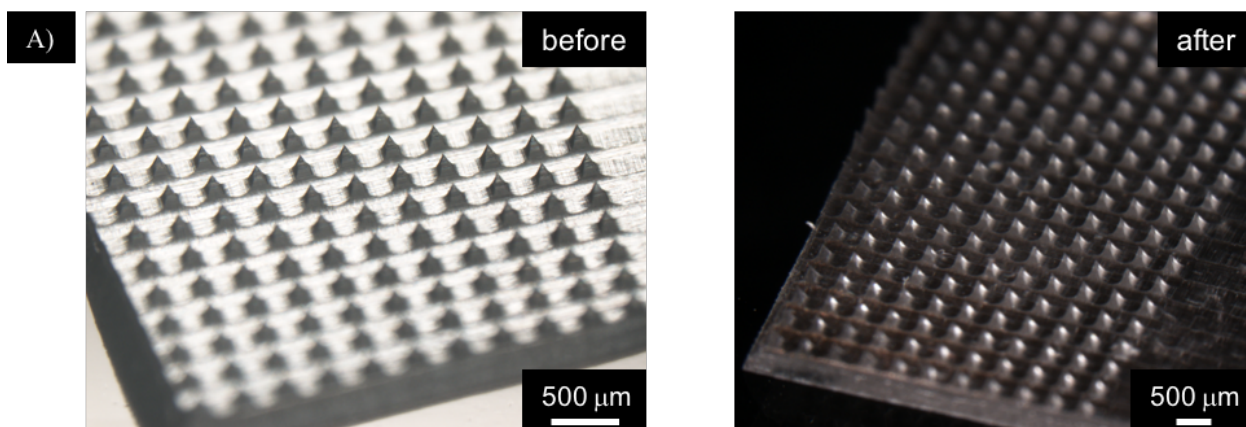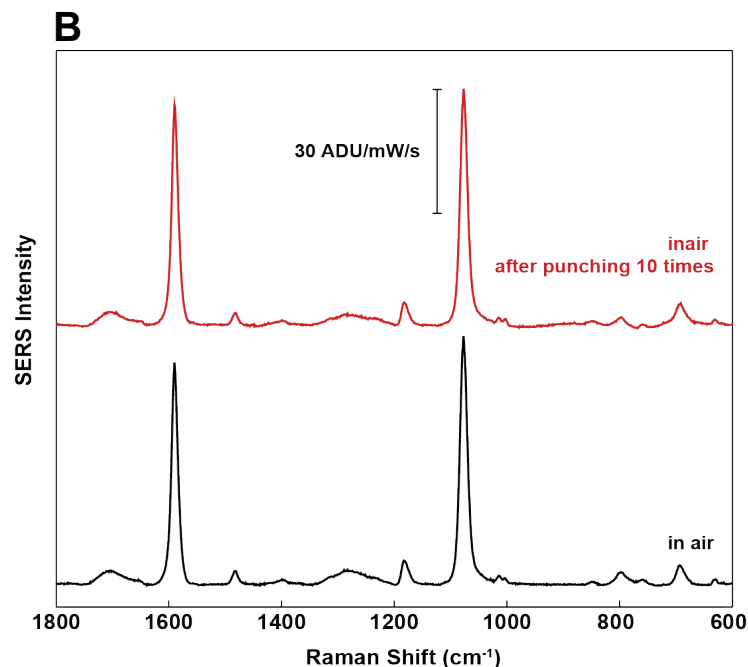
Figure 51. Mechanical stability of plasmonic NOA microneedles upon skin insertion mimicking punching test. (A) Optical images before and after puncture and (B) SERS activity spectra of plasmonic NOA microneedles before and after punching test (Average of seven spectra using 20x ELWD objective, P_{ex} = 1 mW, λ_{ex} = 785 nm, with baseline correction, and normalized to the SERS peak intensity at 1076cm^{-1}).

5.3.2.1 pH calibration curve

To demonstrate *in situ* pH sensing ability of the plasmonic microneedle arrays functionalized with 4-MBA, we took SERS spectra of the sensor in Britton-Robinson buffer with pH ranging from 2 to 12 with 1 pH increments. As shown in **Figure 52a and b**, the pH-responsive peak at around 1421 cm^{-1} (carboxylate vibrational mode) shifts to 1400 cm^{-1} as the pH decreases. When calibrated, the integrated intensity of that mode is known to provide a measure for the pH of the sensor environment. We first calibrated the sensor by taking the ratio between the integrated peak intensity of the carboxylate peak (A_{cbx}) to a mode at 1076 cm^{-1} (A_{1076}), which is insensitive to pH variations. The precision was evaluated by collecting and averaging SER spectra of three replicate sensors, measuring 7 different microneedle tips for each sensor. The normalized ratio was then plotted against pH, leading to a well-known S-shaped sigmoidal curve. For comparison, we repeated the same procedure using a well-known SERS substrate, Au film-over-nanospheres (AuFON). As shown in **Figure 53c**, a small variation in the pK$_a$ value of functionalized 4-MBA functionalized can be observed between the two substrates (7.13 for AuFON and 7.38 for the plasmonic microneedle arrays), which is due to the difference in the surface density of 4-MBA on the two substrates. The pK$_a$ value for 4-MBA on AuFON was slightly lower that on the plasmonic microneedle arrays, which indicates that the density of 4-MBA is slightly higher on AuFON than on the plasmonic microneedle arrays. However, the two calibration curves in **Figure 52c** suggest that the two substrates are comparable.

57

In addition, the S-shaped calibration curves allows determination of the working pH region as the range between 5 to 9 (**Figure 52c**). The sensor resolution was evaluated by measuring a refined calibration curve (0.2 pH increments), which led to a nominal value of 0.23 pH units (twice the standard deviation at pH 7). Lastly, the pH reversibility of the sensor was demonstrated by cycling the pH between 2 to 12 (total of 6 cycles) shown in **Figure 52e**.
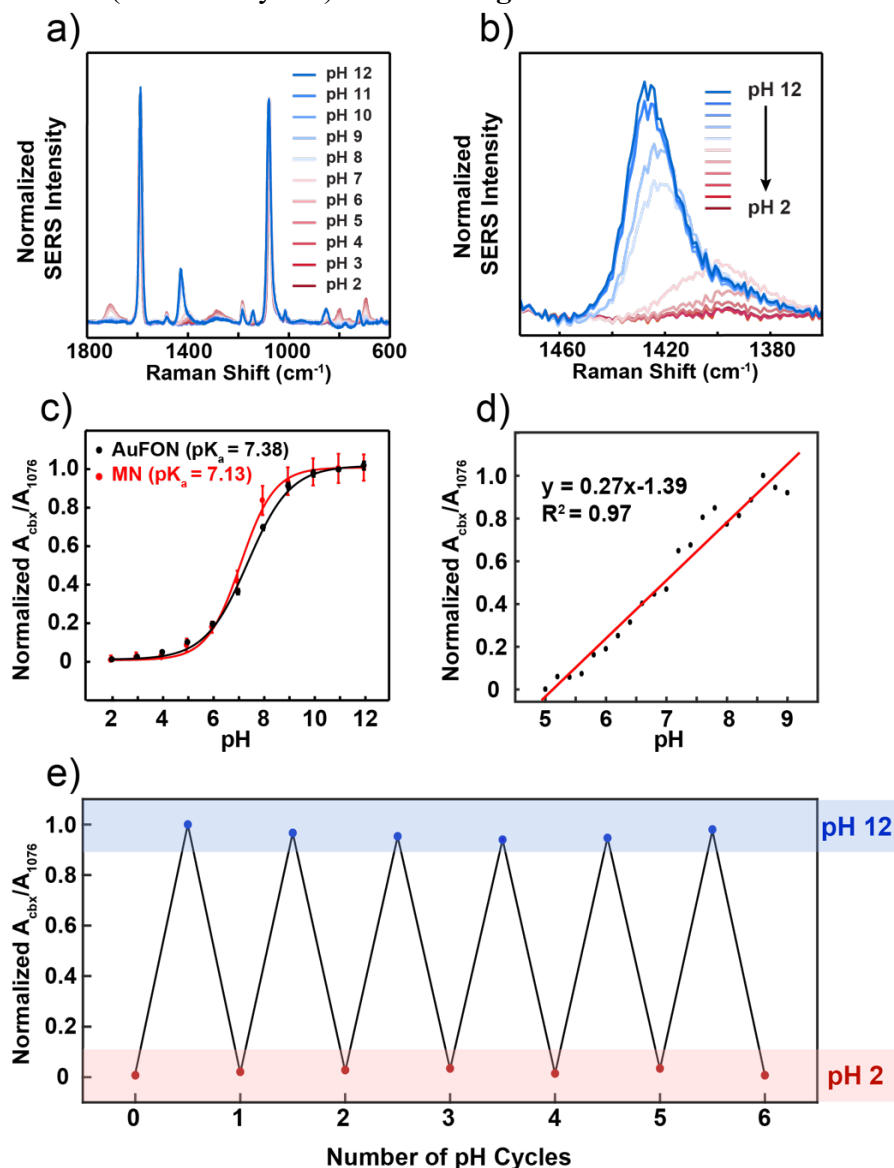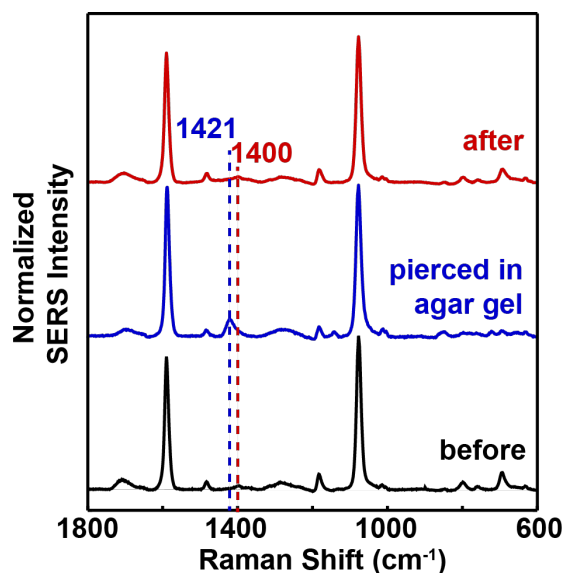

Figure 52. pH sensing with the plasmonic microneedle arrays in Britton-Robinson buffer solution. a) SERS spectra of the plasmonic microneedle arrays functionalized with 4-MBA in Britton-Robinson buffer ranging from pH 2 to 12 with pH 1 increments, and b) magnified spectra to show the pH-sensitive peak at around 1400 cm^{-1}. Each pH level is an average of 7 different microneedle tips. c) S-shaped calibration curves for the plasmonic microneedle arrays (MN) in red and a standard SERS substrate (AuFON) in black in the pH 2-12 range with 1 pH increments (MNs: 7 different tips were collected and was averaged from 3 different samples, AuFON: 5 different spots were collected from one sample and averaged). d) A linear calibration curve for the plasmonic

58

microneedle arrays range in the pH 5-9 range with 0.2 pH increments. e) A reversibility plot for the plasmonic microneedle arrays (cycling the pH of the buffer solution between 2 to 12). The parameters for the SERS data acquisitions were λ_{ex} = 785 nm, 20x ELWD objective, t_{acq} = 1 min. The excitation power for MNs and AuFON were 1 mW and P_{ex} = 270 µW, respectively. As a note, the NOA 65 background was subtracted from all the SERS data.

5.3.2 In situ sensing in agar gel skin phantom

As an initial demonstration of *in situ* sensing, we measured the pH inside a skin phantom agar gel. First, a SER spectrum of the plasmonic microneedle arrays was acquired in air as a baseline (**Figure 53a, black**). Then the sensor was punctured into an agar gel skin phantom, and SER spectra were collected through the microneedle arrays while the sensor was inserted in the skin phantom (**Figure 53a, blue**). The carboxylate peak at around 1400 cm^{-1} shifted to 1420 cm^{-1} and the peak intensity increased when the sensor was in the skin phantom. After removing the sensor and rinsing with water, the SERS was measured again in air to check the reversibility. As shown in **Figure 53a** red trace, the peak at around 1420 cm^{-1} shifted back to 1400 cm^{-1}, similar to SERS spectrum taken in air before puncturing the skin phantom (**Figure 53a, black**). This result also demonstrates the reversibility of the sensor.


Figure 53. *In situ* sensing with plasmonic microneedle arrays in an agar gel skin phantom. SERS spectra taken in air before puncturing an agar gel (black), while pierced in agar gel (blue), and in air after puncturing an agar gel (red). Each spectrum is an average of 7 different microneedle tips. The parameters for the SERS data acquisitions were: λ_{ex} = 785 nm, 20x ELWD objective, t_{acq} = 1 min, P_{ex} = 1 mW.

5.3.3 Mechanical and thermal stability

Next, we tested the mechanical stability of the plasmonic microneedle arrays by comparing the SERS spectra of the sensor before and after puncturing in an agar gel skin phantom. As shown in **Figure 54**, no loss of 4-MBA signal was observed. To test the thermal stability of the sensor, we

incubated the sensor in 1x phosphate buffered saline (PBS) solution for one month. The SER spectra before and after a month-long incubation in the buffer showed no loss of 4-MBA signal (**Figure 55a**). In addition, light extinction spectra of the sensor were taken over four weeks and compared to the control (MNs without AuNRs). As shown in **Figure 55b**, the extinction spectra show that AuNRs are present even after incubating in a buffer solution.
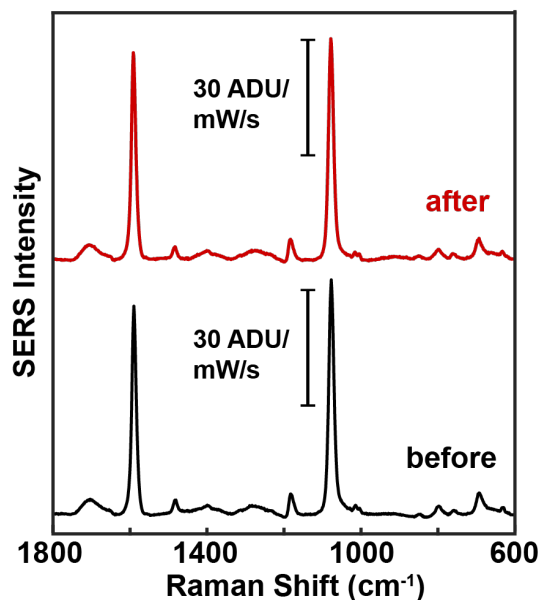
Figure 54. Mechanical stability of the plasmonic microneedle arrays. SER spectra of the sensor before and after puncturing agar gel skin phantom 10 times. Each spectrum is an average of 7 different microneedle tips. The parameters for the SERS data acquisitions were: $\lambda_{ex} = 785$ nm, 20x ELWD objective, $t_{acq} = 1$ min, $P_{ex} = 1$ mW.
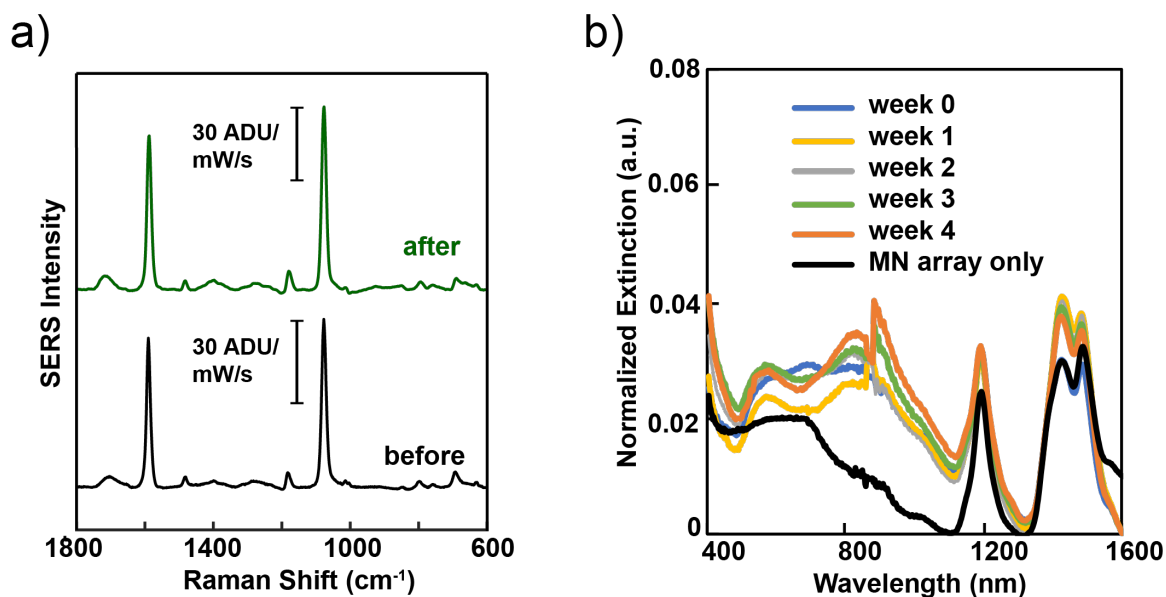
Figure 55. Thermal stability of the plasmonic microneedle arrays. SER spectra of the sensor a) before and after incubation in 1x PBS buffer for one month and b) normalized light extinction spectra of the plasmonic microneedle arrays incubated in 1 x PBS buffer over four weeks compared with a control (MN array only). Each SER spectrum is an average of 7 different microneedle tips. The parameters for the SERS data acquisitions were: λ_{ex} = 785 nm, 20x ELWD objective, t_{acq} = 1 min, P_{ex} = 1 mW.

## Major Task 3. In vivo glucose SERS sensing

6. EX VIVO SERS SENSING

6.1 Implantation of nanosensors with SERS/SESORS detection and demonstration of stability and functionality of the sensor.

We successfully fabricated a plasmonic microneedle arrays sensor and evaluated the sensor platform functionality by detecting a biologically important metric, pH. The results of this work were published in Nano Letters.[19] The sensor described in this publication was the first to combine SERS-active nanoparticles with polymeric microneedle arrays and demonstrated both *in situ* and *ex vivo* sensing, thereby achieving some of the main goals of this project.

In this article, we described the mechanical stability of microneedle arrays implanted in agar gel skin phantoms and human skin (**Figures 53, 54, 55, and 56**), and the resulting maintenance of SERS signal quality. First, we showed that the SERS signal before implantation into an agar gel was similar to the signal obtained during implantation and after implantation (**Figure 53** in section 5.3.2). Next, we showed that after 10 insertions into an agar gel, the SERS signal produced by the microneedle array was preserved (**Figure 54** in section 5.3.3), demonstrating the reusable nature of the sensor patches. To address the long-term potential use of these patches, we incubated the arrays in PBS for one month and showed that the SERS signal quality was maintained and stable over that duration (**Figure 55** in section 5.3.3).

6.2 Application of nanosensors on ex vivo skin samples with SERS/SESORS detection.

To translate this approach to *ex vivo* sensing, we applied the plasmonic microneedle array sensor to human skin. We determined the penetration depth of the microneedle array in skin using optical coherence tomography (OCT) and the sensor's ability to measure pH *in situ* by SERS. Compared with the flat region of the array as a control, the region with microneedles shows that microneedles can be placed in skin (**Figure 56**).
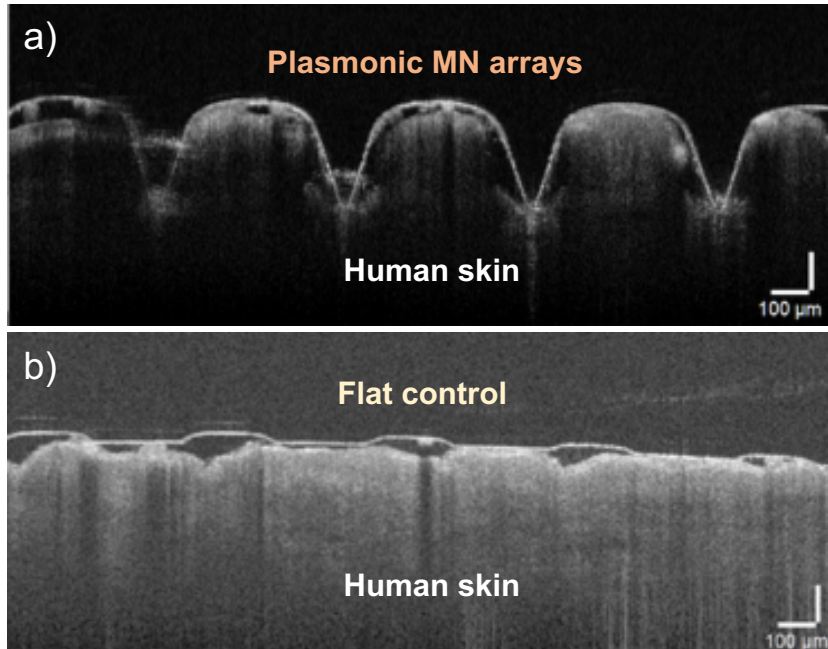
Figure 56. Optical coherence tomography (OCT) images. a) Plasmonic microneedle (MN) arrays and b) flat control (without MN) inserted onto human skin.

Next, to change and measure the skin pH in the range between pH 6.6 and 7.6 (ISF pH), we incubated human skin in Dulbecco's phosphate buffered saline (DPBS) with pH 6.6, 7.1, and 7.6 for 12 hours while replacing the buffer solution every 2 hours. As shown in **Figure 57**, the incubation was performed in a Petri dish while the tissue floated on a metal mesh boat so that the dermal side is in contact with the buffer solution and the top part (the stratum corneum) remains dry.
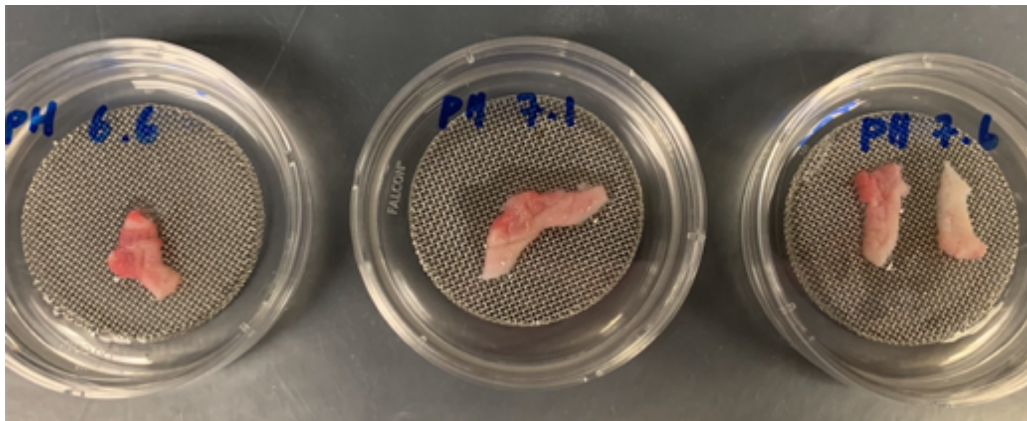
Figure 57. Image of human skin tissues on mesh boat in Petri dish filled with DPBS with three different pHs (pH 6.6, 7.1, and 7.6).

After incubation, we dried the bottom of the skin with clean lab tissue paper and inserted a microneedle array in the skin. We then acquired SERS while the laser was focused through the polymer and onto the tips, as with the agar gel skin phantom. As controls, SER spectra of a microneedle array sensor was taken in the DPBS buffer solution in which the human skin was incubated. As shown in **Figure 58**, compared to the controls, the A_{cbx}/A_{1076} corresponds well with the measurement from the skin.
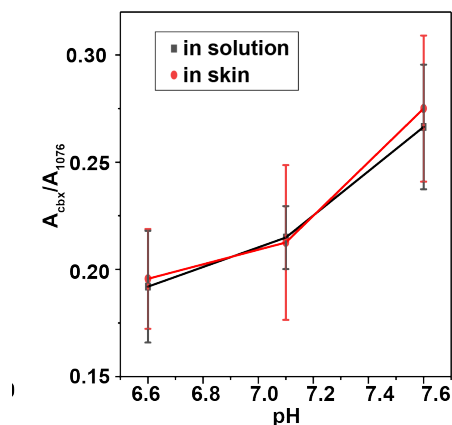
Figure 58. Comparison plot of A_{cbx}/A_{1076} of MN array with AuNRs functionalized with 4-MBA inserted in human skin versus in DPBS solutions with pH 6.6, 7.1, and 7.6. Each point is an average of 7 different microneedle tips, the error bars are the standard deviation at each pH, and the measurements were done by focusing the laser through the polymer and on the tips. The parameters for the SERS data acquisitions were: $\lambda_{ex} = 785$ nm, 20x ELWD objective, $t_{acq} = 1$ min, $P_{ex} = 1$ mW.

We then characterized the microneedle array sensor after puncturing human skin using UV-vis, SERS, and SEM. The SERS signal (**Figure 59a**) was stable and light extinction spectra (**Figure 59b**) showed AuNR aggregates present after puncturing human skin (with pH 6.6, 7.1, and 7.6).
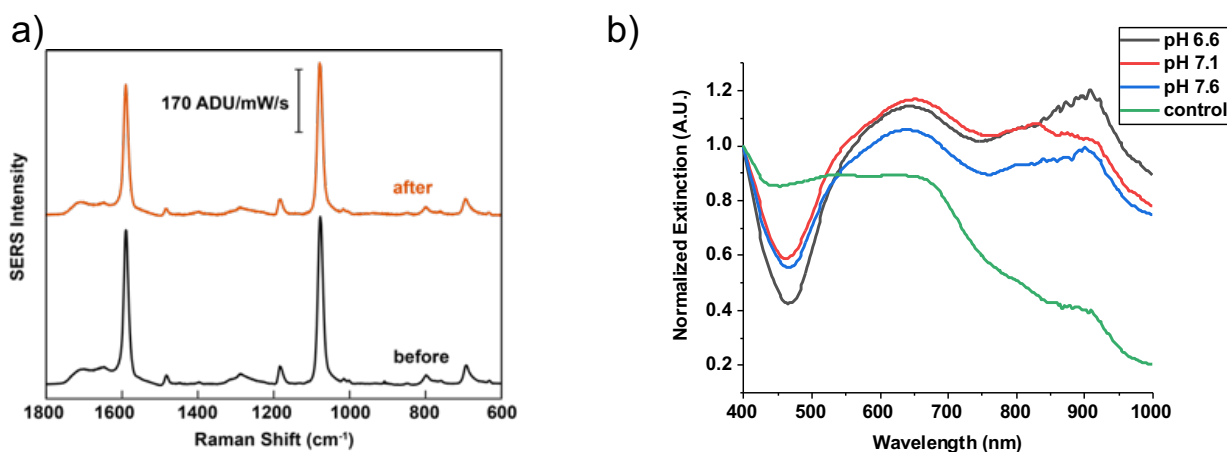
Figure 59. Optical characteristics of plasmonic MN array following *ex vivo* punching test using human skin. (a) SER spectra of plasmonic MN array before (black) and after (orange) one time insertion in human skin (taken in air). Each spectrum is an average of 7 different microneedle tips.

The measurement was done by focusing the laser through polymer and on the tips. The parameters for the SERS data acquisitions were: λ_{ex} = 785 nm, 20x ELWD objective, t_{acq} = 1 min, P_{ex} = 1 mW. (b) Normalized extinction spectra of plasmonic MN array functionalized with AuNRs after insertion into human skin tissues with pH 6.6 (black), pH 7.1 (red), pH 7.6 (blue), and MN array control without AuNRs (green).

SEM images of microneedle arrays after insertion in human skin showed that the microneedles were still intact with AuNR aggregates present on the surface (**Figure 60**). Lastly, to test the mechanical stability of the sensor, the microneedle sensor was applied to human skin tissue repeatedly (10 punches). The SER spectra before and after 10 punches showed no loss of 4-MBA signal (**Figure 61**).
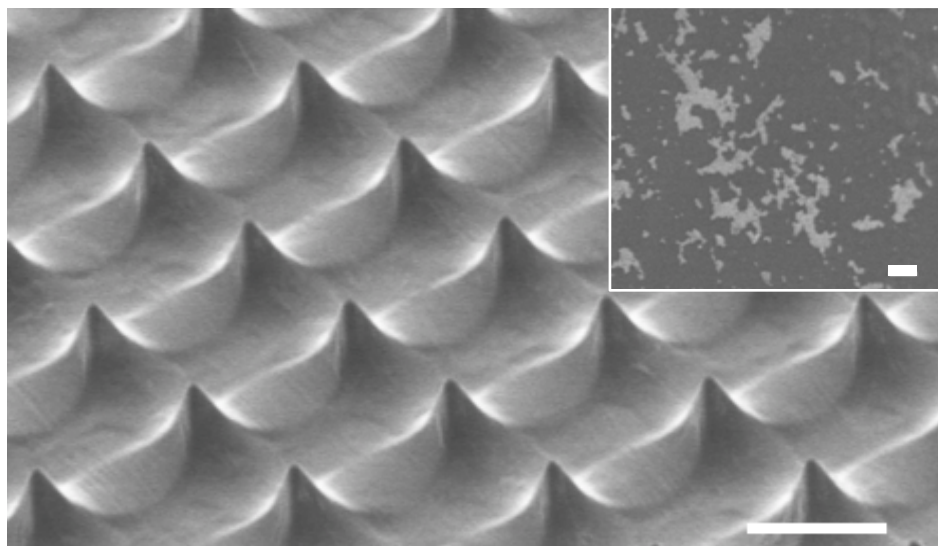
Figure 60. SEM image of MN array with AuNRs functionalized with 4-MBA after puncturing human skin (scale bars are 200 μm and 2 μm (inset)).
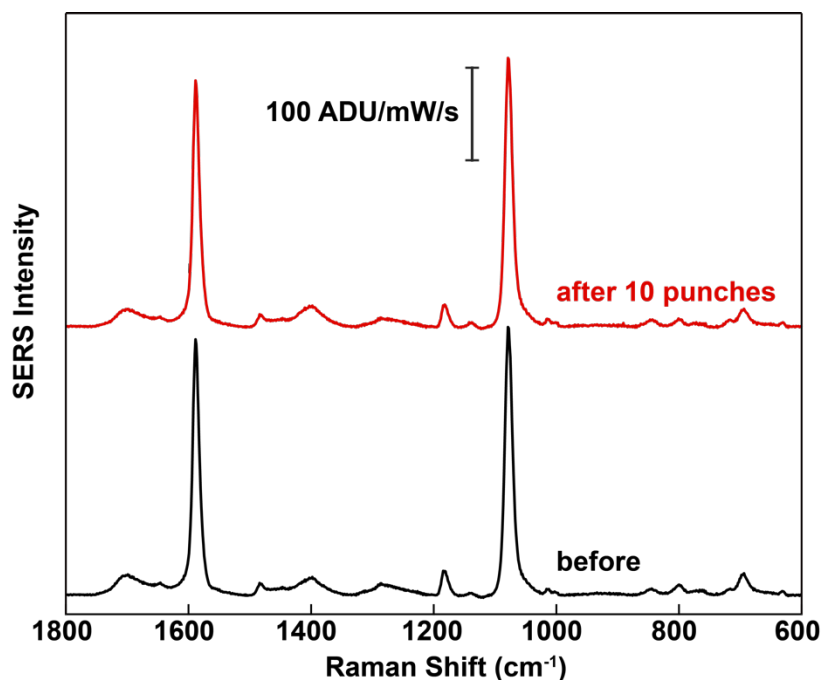
Figure 61. SER spectra before (black) and after (red) 10 punches in human skin. Each spectrum is an average of 7 different microneedle tips. The measurement was done by focusing the laser through polymer and taken in pH 6.6 DPBS solution (filled in a quartz cuvette). The parameters for the SERS data acquisitions were: λ_{ex} = 785 nm, 20x ELWD objective, t_{acq} = 1 min, P_{ex} = 1 mW.

From the *ex vivo* study, we demonstrated the sensing ability and the mechanical robustness of the plasmonic microneedle arrays after inserting in skin. The next step is to investigate the toxicity and the lifetime of the sensor after a long period in skin. In order to do so, *in vivo* studies should be performed. Our studies have not characterized the long-term stability and performance of the sensor arrays in animal models, and we are not able to comment on the stability of the sensor to biofouling and any toxicity.

In conclusion, we report the design and fabrication of a plasmonic microneedle array SERS sensor and demonstrate its SERS activity to measure different pH levels in solutions, in an agar gel skin phantom, and in human skin. Measurement of pH with this sensor was both reversible and reproducible. The use of surface chemistries that provide reports of other molecular analytes, together with the mechanical and optical properties of the microneedle array offer a strategy for sensing a variety of relevant analytes in interstitial fluids.

References:

1   Kurouski, D. *et al.* Unraveling the Near- and Far-Field Relationship of 2D Surface Enhanced Raman Spectroscopy Substrates Using Wavelength-Scan Surface-Enhanced Raman Excitation Spectroscopy. *Journal of Physical Chemistry C* **121**, 14737-14744 (2017).

2   Irache, J. M. *et al.* Bioadhesive properties of Gantrez nanoparticles. *Molecules* **10**, 126-145 (2005).

3   Donnelly, R. F. *et al.* Hydrogel-forming microneedle arrays exhibit antimicrobial properties: Potential for enhanced patient safety. *International Journal of Pharmaceutics* **451**, 76-91 (2013).

4   Donnelly, R. F. *et al.* Hydrogel-Forming and Dissolving Microneedles for Enhanced Delivery of Photosensitizers and Precursors. *Photochemistry and Photobiology* **90**, 641-647 (2014).

5   Donnelly, R. F. *et al.* Hydrogel-Forming Microneedles Prepared from "Super Swelling" Polymers Combined with Lyophilised Wafers for Transdermal Drug Delivery. *PLoS One* **9** (2014).

6   Hamilton, G. R. C., Fullerton, L., McCaughan, B., Donnelly, R. F. & Callan, J. F. A ratiometric fluorescent hydrogel sensor for zinc(II) based on a two fluorophore approach. *New Journal of Chemistry* **38**, 2823-2830 (2014).

7   Sharma, B. *et al.* Bisboronic Acids for Selective, Physiologically Relevant Direct Glucose Sensing with Surface-Enhanced Raman Spectroscopy. *J. Am. Chem. Soc.* (2016).

8   McAnally, M. O. *et al.* Quantitative Determination of the Differential Raman Scattering Cross Sections of Glucose by Femtosecond Stimulated Raman Scattering. *Anal Chem* **89**, 6931-6935 (2017).

9   Wu, X. *et al.* Selective sensing of saccharides using simple boronic acids and their aggregates. *Chem Soc Rev* **42**, 8032-8048 (2013).

10   Ribet, F., Stemme, G. & Roxhed, N. Real-time intradermal continuous glucose monitoring using a minimally invasive microneedle-based system. *Biomed. Microdevices* **20** (2018).

11   Miller, P. R. *et al.* Multiplexed microneedle-based biosensor array for characterization of metabolic acidosis. *Talanta* **88**, 739-742 (2012).

12   Bollella, P., Sharma, S., Cass, A. E. G. & Antiochia, R. Microneedle-based biosensor for minimally-invasive lactate detection. *Biosens. Bioelectron.* **123**, 152-159 (2019).

13   Windmiller, J. R. *et al.* Bicomponent Microneedle Array Biosensor for Minimally-Invasive Glutamate Monitoring. *Electroanalysis* **23**, 2302-2309 (2011).

14   Mishra, R. K., Mohan, A. M. V., Soto, F., Chrostowski, R. & Wang, J. A microneedle biosensor for minimally-invasive transdermal detection of nerve agents. *Analyst* **142**, 918-924 (2017).

15   Tsung, C. K. *et al.* Selective shortening of single-crystalline gold nanorods by mild oxidation. *J. Am. Chem. Soc.* **128**, 5352-5353 (2006).

16   Dasog, M. & Scott, R. W. J. Understanding the oxidative stability of gold monolayer-protected clusters in the presence of halide ions under ambient conditions. *Langmuir* **23**, 3381-3387 (2007).

17   Kyu, T. & Nwabunma, D. Simulations of microlens arrays formed by pattern-photopolymerization-induced phase separation of liquid crystal/monomer mixtures. *Macromolecules* **34**, 9168-9172 (2001).

18   Ferhan, A. R., Guo, L. H. & Kim, D. H. Influence of Ionic Strength and Surfactant Concentration on Electrostatic Surfacial Assembly of Cetyltrimethylammonium Bromide-Capped Gold Nanorods on Fully Immersed Glass. *Langmuir* **26**, 12433-12442 (2010).

19   Park, J. E. *et al.* Plasmonic Microneedle Arrays for in Situ Sensing with Surface-Enhanced Raman Spectroscopy (SERS). *Nano Lett.* **19**, 6862-6868 (2019).

20   Brasiliense, V., Park, J. E., Berns, E. J., Van Duyne, R. P. & Mrksich, M. Surface potential modulation as a tool for mitigating challenges in SERS-based microneedle sensors. *Sci Rep* **12**, 15929 (2022).

21   Brasiliense, V., Park, J. E., Chen, Z., Van Duyne, R. P. & Schatz, G. C. Nanopipette-based electrochemical SERS platforms: Using electrodeposition to produce versatile and adaptable plasmonic substrates. *J. Raman Spectrosc.* **52**, 339-347 (2021).

22   Arbos, P., Wirth, M., Arangoa, M. A., Gabor, F. & Irache, J. M. Gantrez (R) AN as a new polymer for the preparation of ligand-nanoparticle conjugates. *Journal of Controlled Release* **83**, 321-330 (2002).

23   Ojer, P., de Cerain, A. L., Areses, P., Penuelas, I. & Irache, J. M. Toxicity Studies of Poly(Anhydride) Nanoparticles as Carriers for Oral Drug Delivery. *Pharmaceutical Research* **29**, 2615-2627 (2012).

24   Luzardo-Alvarez, A. B.-M., J.; Varela-Patino, P., Biedma, B. Amoxicillin-Loaded Sponges Made of Collagen and Poly [(Methyl Vinyl Ether) -Co- (Maleic Anhydride)] for Root Canal Treatment : Preparation , Characterization and In Vitro Cell Compatibility. *J. Biomater. Sci. Polym. Ed.* **22**, 329-342 (2011).

25   Moreno, E. *et al.* Thermosensitive hydrogels of poly(methyl vinyl ether-co-maleic anhydride) - Pluronic (R) F127 copolymers for controlled protein release. *International Journal of Pharmaceutics* **459**, 1-9 (2014).

Opportunities for training and professional development provided by the project

Ji Eun Park joined the Van Duyne group in September 2016 as a second-year graduate student. She was trained in AuFONs fabrication, LSPR and SERS characterization, including EF measurement. She has graduated and works for a company in Dallas, TX.

Dr. Anne-Isabelle Henry was selected for an oral presentation at the National Spring 2017 meeting of the American Chemical Society (April 2-6, 2017) in San Francisco, CA. Her talk, entitled 'Towards SERS-enabled diagnostics: quantitative detection of glucose and other biomarkers', presented the results from the 1,1BBA-AuFON sensor published in September 2016 in the Journal of the Americal Chemical Society (Sharma et al. J. Am. Chem. Soc. 138, 13952-13959) by herself, Pradeep Bugga, Milan Mrksich, and Richard Van Duyne.

Dr. Vitor Brasiliense joined the project in July 2018 and worked together with Ji Eun Park to develop EC-SERS microneedle platform. Dr. Ju-Young Kim joined the group in June of 2019 and was fully trained on a laser table and instruments from core facilities (SEM and AFM).

Dissemination of results to communities of interest

Ji Eun Park and Vitor Brasiliense took part in the 'All Scout Nanoday' outreach event organized by the International Institute for Nanotechnology and hosted in part by the Van Duyne lab. They engaged with a young audience (~10-14 year old girl and boy scouts from the Chicago area) to communicate about nanotechnology research and careers in science.

Plan for the next reporting period

Nothing to report.

4. IMPACT

Impact on the development of the principal discipline(s) of the project
The development of plasmonically active polymer platforms is new when applied to combining microneedles and SERS. As such, this an exciting new avenue demonstrated by this project. Both groups closely and actively pursued the development of these new functional platforms. We published six articles as a result of this grant, each advancing the field.

We have developed a plasmonic microneedle arrays sensor and successfully applied the sensor in skin tissues (e.g., human, rat, pig). To evaluate the platform capability, we have demonstrated its use for pH sensing. This work has been accepted for publication in a high impact journal (Nano Letters). While investigating alternatives to chemical capture ligands, we have identified a general strategy to reversibly bind analytes to our sensor surface using potential. This is a general concept which is likely to be applied to a wide range of biosensors. In the context of spectro-electrochemical biosensors, we have identified and demonstrated a strategy that allows interpretable multivariate analysis to be deployed. We expect these results to be of interest to the general biosensing community as it introduces a flexible tool that can be applied in various different contexts/sensors. We published two articles related to the electrochemical approach.

Impact on other disciplines

Nothing to report.

Impact on technology transfer

Nothing to report.

Impact on society beyond science and technology

Nothing to report.

5. CHANGES/PROBLEMS

Changes in approach and reasons for change

Nothing to report.

Actual or anticipated problems or delays and actions or plans to resolve them
Difficulties in reproducing previous data with 1,1-BBA was a challenge toward the beginning of this project. This was addressed by testing several alternative ligands and approaches for detecting glucose. Second, the death of one of the original PIs, Dr. Van Duyne, impacted the ability to carry out SERS measurements outside of an NU core facility.

Changes that had a significant impact on expenditures

Nothing to report.

Significant changes in use or care of human subjects, vertebrate animals, biohazards, and/or select agents

Nothing to report.

6. PRODUCTS

Publications, conference papers, and presentations

Journal publications
1. A.-I. Henry, T. W. Ueltschi, M. O. McAnally, and R. P. Van Duyne. Surface-enhanced Raman spectroscopy: from single particle/molecule to angstrom-scale spatial resolution and femtosecond time resolution. *Faraday Discuss,* **2017**, *205*, 9-30.

2. D. Kurouski, N. Large, N. Chiang, A.-I. Henry, T. Seideman, G. C. Schatz, and R. P. Van Duyne. Unraveling the near- and far-field relationship of 2D surface-enhanced Raman spectroscopy substrates using wavelength-scan surface-enhanced Raman excitation spectroscopy. *J. Phys. Chem. C*, **2017**, *121*, 14737-14744.

3. M. O. McAnally, B. T. Phelan, R. M. Young, M. R. Wasielewski, G. C. Schatz, and R. P. Van Duyne. Quantitative determination of the differential Raman scattering cross-sections of glucose by femtosecond stimulated Raman scattering. *Anal. Chem.*, **2017**, *89*, 6931-6935.

4. J. Park, N. Yonet-Tanyeri, E. Vander Ende, A. I. Henry, B. E. Perez White, M. Mrksich, R. P. Van Duyne. Plasmonic Microneedle Arrays for in Situ Sensing with Surface-Enhanced Raman Spectroscopy (SERS). *Nano Letters,* **2019***, 19,* 6862-6868.

5. V. Brasiliense, J. E. Park, Z. Chen, R. P. Van Duyne, G. P. Schatz. Nanopipette-based electrochemical SERS platforms: Using electrodeposition to produce versatile and adaptable plasmonic substrates *Journal of Raman Spectroscopy*, **2020**, *52*, 339-347.

6. V. Brasiliense, J. E. Park, E. J. Berns, R. P. Van Duyne, M. Mrksich, Surface potential modulation as a tool for mitigating challenges in SERS-based microneedle sensors. *Scientific Reports*, **2022**, *12*, 15929.

Books or other non-periodical, one-time publications

Nothing to report.

Other publications, conference papers, and presentations

- Dr. Nihan Yonet-Tanyeri presented her work with a poster presentation on the Society for Biomaterials (SFB) Biomaterials Day at the University of Michigan-Ann Arbor, MA in October 2017 entitled "SERS Based Transdermal Patches for Nanosensing."

- Dr. Nihan Yonet-Tanyeri was also invited to give an oral presentation at the Annual Meeting of American Institute of Chemical Engineers (AIChE, October 28 - November 2, 2018) that will be held in Pittsburgh, PA. Her talk is entitled "Non-invasive Plasmonic Biosensors for In Situ Glucose Monitoring."

- Ji Eun Park presented her work with a poster presentation at American Chemistry Society National Meeting and Expo at Orlando, Florida in April 2019 entitled "Plasmonic Microneedles for Continuous pH Monitoring Using Surface-Enhanced Raman Spectroscopy."

Website(s) or other Internet site(s)

Nothing to report.

Technologies or techniques

Plasmonic microneedles described in Accomplishments are technologies directly resulting from this program.

Inventions, patent applications, and/or licenses

Nothing to report.

Other Products

Nothing to report.

7. PARTICIPANTS AND OTHER COLLABORATING ORGANIZATIONS

Individuals who participated on the project

PIs
Richard Van Duyne
Milan Mrksich

Research Professors
Anne-Isabelle Henry
Eric J. Berns

Post-doctoral Researchers

Nihan Yonet-Tanyeri
Vitor Braisiliense
Ju-Young Kim
Guru Neupane

Graduate Students
Ji Eun Park
Emma Vander Ende
Michael O. McAnally
Pradeep Bugga
Daniel Sykora
Che-Fan Huang
Adam Pluchinsky
Sarah Anderson

Research Technologists
Allen Yang
Tsatsral Iderzorig

Other organizations involved as partners

Organization Name: NU*ANCE*, Northwestern University
Location of Organization: Evanston, IL
Partner's contribution to the project: Facilities; project staff from the Van Duyne lab and Mrksich lab used Northwestern's electron microscopy facility to characterize the morphology of the microneedle platforms by scanning electron microscopy.

Organization Name: Skin Tissue Engineering Core, Northwestern University
Location of Organization: Chicago, IL
Partner's contribution to the project: project staff from the Van Duyne lab and Mrksich lab collaborated with the core staff for skin experiments.

8. SPECIAL REPORTING REQUIREMENTS

Since this is a collaborative award and the PI (Richard Van Duyne) deceased, the Partnering PI (Milan Mrksich) will submit one report.

9. APPENDICES

None.